Three-Dimensional Analysis of Impact Processes on Planets

Thesis by

Toshiko Takata

In Partial Fulfillment of the Requirements
for the Degree of
Doctor of Philosophy

California Institute of Technology
Pasadena, California

1995

(Defended October 19, 1994)

Acknowledgments

First, I would like to thank all of the resident faculty, students, secretaries, and technical staff in the South Mudd building. I may not be able to address each of you personally, but thanks for your support during my wonderful stay at Caltech.

I would like to acknowledge five years of academic and personal support from my thesis adviser, Tom Ahrens. Even though my English writing and speech are not understandable, you have been so patient that you corrected my writings an infinite number of times without any complaint! Moreover, you have been so understanding my difficult situation of being separated from my husband, and have never complained of my long vacations with him. Thank you.

Thanks to my parents, who understood my career goal and have sent me to the U.S. with encouragement.

Looking back to the beginning of my career in planetary science, I thank Hitoshi Mizutani, who was my undergraduate thesis advisor, and who helped me in going back to graduate school after several years-absence from school. Without my work with you for my bachelor's thesis, I could not have accomplished the work on Comet Shoemaker-Levy 9 in such a short time. Thanks.

The scientific environment at Caltech is terrific. Thanks to all the faculty in Planetary Science and the Seismo Lab. Dugan O'Keefe always supported me with intellectual comments and guided me through the field of impact cratering. Andy Ingersoll, your brilliant scientific and daddy-type instructive talents are a goal I hope to achieve. My TA experience with your classes is one of the best treasures obtained at Caltech. Bruce Murray, who was once my neighbor, helped me to get rid of my old customs. Dave Stevenson, with whom I worked on one of my propositions always has the answers. Thank you, all of you.

Thanks to all the people in the shock wave lab. Sue, you sometimes play the role of my elder-sister and sometimes of my Mom in my Caltech life. Without you, I would not have been able to have done this. Bill Anderson, thank you for your advice and comments, and for your help on manuscripts every time. Margaret, thank you for your support. Tom Duffy, Noreen Evans, and Linda Rowan, thank all of you. Several people had contributed to develop the SPH code used in my thesis, before I started this work. Cathy Smither was the first person who got the code to work for her thesis. I hope the code will be taken over Mike Lainhart or future students in the shock wave lab.

My office mates, Lyatt, Eric, Albert, Mark, and Steven, thanks for sharing your joys and pleasures. Shingo, Brad, and Laura, thank you for your friendship and making my life fun. Kay, Irma, and Mike, in the Planetary Science office, thank you for your help. Steve Leroy provided me the TEXmacros and the instruction on how to use them.

Jim and Akiko Mori often treated a poor student, me, to delicious dinners during my busy days.

Finally, I heartily thank my husband, Satoshi. You pointed me in the right direction and encouraged me all the time. Thank you for your patience and for your partnership. You are super, honey!

Introduction

Impact between and upon planetary bodies is an important process in the formation and evolution of objects in the solar system. Impact craters are observed on nearly all of the solid surfaces of planets and satellites. Some asteroids and satellites are also considered to be the the result of impact on parent bodies.

Impact cratering on planetary surfaces has been studied particularly since lunar mapping started before the Apollo era in the 1960s. The analytical and experimental approaches which established the scaling of impact craters, that is, the relationship between the impactor size, density, and velocity versus crater diameter, depth, and ejecta mass was pioneered by Gault [1973], Chabai[1977], and more recently by Schmidt, Housen, and Holsapple [Holsapple and Schmidt, 1982; Schmidt and Housen, 1987]. Numerical simulation began in this field in the 1960's, by Bjork [1961], O'Keefe and Ahrens [1977], Orphal [Orphal et al. 1980], and others.

Since then, the various studies have been performed describing giant planetary impact [Benz et al. 1986]. Previous studies were restricted to the environment without an atmosphere, to avoid the complication of the problem. However, many of the planets are covered by an atmosphere, particularly the Earth, Venus, and outer planets and some of their satellites have thick atmospheres. These atmospheres affect impact cratering and also related impact processes, such as ablation of the meteoroids in the atmosphere. Therefore, it is important to take into account the atmospheric effects in impact processes.

Most previous studies in the field of impact processes (experimental or numerical) treated normal impacts rather than oblique impacts. However, the most possible impact angle is 45° from the zenith. Therefore, the obliqueness of impact processes is important to take into account.

Both atmospheric effects and obliqueness of impact processes are investigated in this thesis. An analytical approach is used in the present study of impact processes on Venus. Another approach used in this thesis is relatively new numerical simulations used Smoothed Particle Hydrodynamics method. This is applied to three-dimensional impact problems including an atmosphere. The numerical code developed here is tested in the prediction of the phenomena of the impact of Comet Shoemaker-Levy 9 on Jupiter.

References

Benz, W., W. L. Slattery, and A. G. W. Cameron, 1986. The Origin of the Moon and the Single Impact Hypothesis - I, *Icarus*, **66**, 515-535.

Bjork, R. J., 1961. Analysis of the Formation of Meteor Crater, Arizona: A Preliminary Report. *J. Geophys. Res.*, **66**, 3379-3387.

Chabai, A. J. Influence of Gravitational Fields and Atmospheric Pressures on Scaling of Explosion Craters. *Impact and Explosion Cratering*, edited by Roddy, D. J., R. O. Pepin, and R. B. Merrill, pp. 1191-1214, Pegamon, New York, 1977.

Gault, D. E., 1973. Displaced Mass, Depth, Diameter, and Effects of Oblique Trajectories for Impact Craters Formed in Dense Crystalline Rocks. *The Moon*, **6**, 32-44.

Holsapple, K. and R. M. Schmidt, 1982. On the Scaling of Crater Dimensions II: Impact Processes. *J. Geophys. Res.*, **87**, 1849-1870.

O'Keefe, J. D. and T. J. Ahrens, 1977. Meteorite Impact Ejecta: Dependence of Mass and Energy Lost on Planetary Escape Velocity. *Science*, **198**, 1249-1251.

Orphal, D. L., W. F. Bordon, S. A. Larson, and P. H. Schultz, 1980. Impact Melt Generation and Transport. *Proc. 11th Lunar Planet. Sci. Conf., Geoch. Cosmoch. Acta. Special Issue*, 2309-2323.

Schmidt, R. M. and Housen, K. R., 1987. Some Recent Advances in the Scaling of Impact and Explosion Cratering. *Int. J. Impact Eng.*, **5**, 543-560.

Abstract

This thesis consists of four chapters. The first chapter describes the numerical method known as Smoothed Particle Hydrodynamics (SPH), that is used in present calculations relating to oblique impact on a planet with an atmosphere. Numerical test results are presented to demonstrate the validity of the present computer code. The SPH code is applied to Comet Shoemaker-Levy 9 impact on Jupiter, particularly the disintegration of the comet in the Jovian atmosphere and the evolution of the vapor plume. These calculations are described in chapter II. In order to interpret the phenomena observed in the impacts, numerical predictions are compared with the observational data. These comparisons are summarized in chapter III. Chapter IV considers analytical models of the formation of radar dark and/or bright halos surrounding impact craters discovered on Venus as a result of the Magellan mission. The surface features caused by the atmospheric shock waves associated with impacts are modeled and applied to the observed Venusian radar features.

Paper I:

The SPH method used for a series of impact calculations is tested. From the performance tests, we infer that the tree structure method for a vectorizing computer code can be applied when the number of particles, N, $\gtrsim 10^4$. Most of the calculations are performed using a CRAY-YMP at Jet Propulsion Laboratory or a CRAY-C90 at Goddard Space Flight Center. Tests for one-dimensional shock propagation show that the developed code yields an error of less than several percent in density and pressure, upon comparison with the analytical impedance-match solution. For spherical, three-dimensional impact of a projectile upon a silicate half-space, the shock wave attenuation of pressure and density calculated by the SPH code is very similar to the results obtained with a finite-difference Lagrangian continuum code (previously obtained by Ahrens and O'Keefe, [1977]). For example, the shock pressures in the near field agree within 15 % differences, whereas the shock pressure in the far field, at 10 projectile radii, differs by a factor of 2 from that calculated previously using a two-dimensional axisymmetric Lagrangian code.

Paper II:

The impact of fragments of Comet Shoemaker-Levy 9 on Jupiter and the resulting vapor plume expansion are investigated by conducting three-dimensional numerical simulations using the Smoothed Particle Hydrodynamics (SPH) method. An icy body, representing the cometary fragments, with a velocity of 60 km/sec and a diameter of 2 km can penetrate to 350 km below the 1-bar pressure level in the atmosphere. Most of the initial kinetic energy of the fragment is transferred to the atmosphere between 50 km and 300 km below the 1-bar pressure level. The shock-heated atmospheric gas in the wake is totally dissociated and partially ionized. Scaling our SPH results to other sizes indicates that fragments larger than $\sim$ 100 m in diameter can penetrate to below the visible cloud decks. The energy deposited in the atmosphere is explosively released in the upward expansion of the resulting plume. The plume preferentially expands upward rather than horizontally due to the density gradient of the ambient atmosphere. It rises $\geq 10^2$ km in $\sim 10^2$ seconds. Eventually the total atmospheric mass ejected to above 1 bar is ≥ 40 times the initial mass of the impactor. The plume temperature at a radius $\sim 10^3$ km is $> 10^3$ K for 10^3 seconds, for a 2-km fragment. We predict that impact-induced plumes will be observable with the remote sensing instruments of the Galileo spacecraft. As the impact site rotates into the view of the earth some 20 minutes after the impact, the plume expansion will be observable using the Hubble Space Telescope and from visible and infrared instruments on ground-based telescopes. The rising plume reaches $\sim$ 3000 km altitude in $\sim$ ten minutes and will be visible from the earth.

Paper III:

Preliminary observational data from the impact of fragments of Comet Shoemaker-Levy 9 (SL9) are compared with smoothed particle hydrodynamic (SPH) and radiative calculations to determine the energies of individual SL9 fragments and the equivalent diameter of the SL9 progenitor. The Hubble Space Telescope (HST) images of the G impact-induced plume demonstrate that it achieved a height of ~3300 km [Hammel et al., 1994]. This is in close agreement with the SPH calculations for a 7×10^{28} erg or 2 km ± 0.3 km diameter solid ice impactor at 60 km/sec. Comparison of the R fragment impact-induced plume brightness in the 8 to 12 μm band, as recorded by the NASA Infrared Telescope Facility (Mauna Kea, HI) [Orton et al. 1994], with our radiative predictive calculations yields a kinetic energy of 4×10^{28} ergs or a diameter of 1.6 ± 0.3 for the R fragment. Using the G and R impacts to calibrate Weaver et al.'s [1994] detailed photometric determination of the relative diameters of pre-Jovian impact projectiles in the SL9 chain from HST images yields revised values for the 11 largest fragment diameters. Adding the inferred masses from the plume and radiative calibration of Weaver et al.'s catalog yields an SL9 progenitor equivalent (ice) diameter of 4.1 ± 0.6 and 3.5 ± 0.5 km, respectively. This compares to a 7.7 km diameter progenitor inferred by Weaver et al. and a 2 km diameter progenitor obtained using tidal break-up modeling by Scotti and Melosh [1993] and Asphaug and Benz [1994]. We also examined the inferred position of Jupiter derived H_2O impact ejecta from the hypothetical (3 to 5 bar) cloud deck and find that although Jupiter derived impact induced plumes having radius of $> 10^3$ km and achieved altitudes of 3×10^3 km, the contained Jovian water ejecta is restricted to the interior of the plume and would be masked from Earth observations by the surprisingly opaque plume. On the basis of Bjorker et al.'s [1994] observations of thirty minutes' water emissions from the plumes of the impact sites of fragments G and K Field and Ferraro's [1994] analysis which indicates that even if SL9 fragments are 50% porous, upon being subjected to entry, the ram pressures, upon reaching the level of 1 bar, squeeze-out virtually all porosity and the present, self-consistent kinemetric and radiative coupling of the SL9 impactor, we conclude: 1) there is no evidence that SL9 was anything but a comet as first suggested by the coma, 2) penetration of 2 km diameter fragments occurs to depths of ~ 300 km, even for a porous comet, as calculated by the present SPH method and by other groups using finite difference methods [Zahnle and MacLow, 1993, Boslough et al., 1994].

Paper IV:

A paraboloidal bow shock model was developed in order to estimate the surface distribution of gas shock-induced modifications surrounding venusian impact craters. We applied two-dimensional oblique shock dynamics to describe a three-dimensional paraboloidal - shaped bow shock impinging upon an assumed incompressible venusian surface. The effects of the hypersonic atmospheric shock acting on the venusian surface are considered in terms of maximum gas pressure, the density, the particle velocity, and the temperature, for varying angles and velocities of impact. The maximum boulder size that can be saltated by the shockwave induced gas flow and the degree of mutual collision of the surface materials are also considered. The present calculations quantitatively predict the areal extent of the gas shock perturbed surface for normal and oblique impact as a function of impact angle and velocity, and radii of impactors. For a 1 km-radius stony meteorite impacting at 20 km/s, the radius of the disturbed area extends ~ 10-17 times the 3-5 km crater radius. The perturbed surface affects the surface radar properties and the present results can provide an explanation of the wide "dark/bright halos" surrounding some of venusian impact craters observed via Magellan imagery. For example, a ~ 50 km radius bright halo within a ~ 20 km dark halo is observed around the 3.1 km-radius crater located at 16.5° north latitude and

334.4° longitude. The average value of the radar backscatter cross section of the $\sim$ 20 km radius dark halo indicates that $\sim$ 50 cm-thick layer of porous lithologic material is superimposed upon the undisturbed surface. The occurrence of the bright halo indicates that the surface roughness in this region is $\sim$ 30% greater than that of the surrounding original surface. The present model can relate the observed crater halo radii to the impact parameters, such as impact velocity and angle, and the impactor radius.

Table of Contents

List of Figures

PAPER I:

PAPER II:

PAPER III:

PAPER IV:

List of Tables

PAPER I:

PAPER III:

PAPER I

Smoothed Particle Hydrodynamics Methods: Review and Numerical Tests

Abstract

The SPH method used for a series of impact calculations is tested. From the performance tests, we infer that the tree structure method for a vectorizing computer code can be applied when the number of particles, N, $\gtrsim 10^4$. Most of the calculations are performed using a CRAY-YMP at Jet Propulsion Laboratory or a CRAY-C90 at Goddard Space Flight Center. Tests for one-dimensional shock propagation show that the developed code yields an error of less than several percent in density and pressure, upon comparison with the analytical impedance-match solution. For spherical, three-dimensional impact of a projectile upon a silicate half-space, the shock wave attenuation of pressure and density calculated by the SPH code is very similar to the results obtained with a finite-difference Lagrangian continuum code (previously obtained by Ahrens and O'Keefe, [1977]). For example, the shock pressures in the near field agree within 15 % differences, whereas the shock pressure in the far field, at 10 projectile radii, differs by a factor of 2 from that calculated previously using a two-dimensional axisymmetric Lagrangian code.

1. Introduction

In this section, the numerical techniques used in chapters II and III are discussed. The computational method employed in these sections, called Smoothed Particle Hydrodynamics (SPH), is used to investigate three-dimensional impact processes on planetary surfaces. The SPH method was originally developed independently by Lucy [1977], for the fission of protostars, and Gingold and Monaghan [1977], for rotating polytropic stars. The SPH method is a fully Lagrangian technique which treats fluids as collections of individual elements (particles) and applies a smoothing function (kernel function) with a characteristic scale length to smear their masses over the entire space. Local density and related physical quantities, e.g., internal energy, are calculated by summing particles interaction at each particle position using the smoothing function. The equation of state (EOS) is, then, applied to each particle to calculate the pressure in each position from the density and internal energy.

This method is highly useful for hydrodynamic problems involving large distortions such as are common in hypervelocity impact problems. Finite-difference methods have been long used to investigate problems in the field of shock-wave physics. However, this method is not easily expanded to three-dimensional coordinate systems because of the problems which arise with severe mesh-grid distortion. Therefore, most finite-difference calculations are limited to treating two-dimensional axisymmetric problems. In contrast, the SPH method is a totally mesh-free method. The physical quantities associated with particles, such as the position and velocity, satisfy the conservation of momentum relation at all times, so that the total dynamical system is described.

A SPH code was originally designed and developed for the astrophysical problems. Applications of this technique have been extended to the materials engineering of hypervelocity impact [Cloutman, 1991 and Stellingwerf, 1990] and planetary impact problems. Various problems employing the SPH method which have been studied in planetary sciences include: the giant impact of Mars-sized planetary body onto the Earth, as a mechanism which has been suggested for the moon formation [Benz *et al.* 1986, 1987, 1989 and Cameron and Benz, 1991], a planetesimal impact onto proto-Mercury to explain the anomalously high mean density (6.5 g/cm^3) of Mercury [Benz *et al.*, 1988], asteroid-asteroid collision [Smither, 1992], the impact process of meteorites on a plane planetary surface [Pongracic, 1988], cometary impact onto the earth, for the delivery of organic materials [Chyba *et al.*, 1990], and, recently, Asphaug and Benz [1994] and Solem [1994] studied the 1992 break-up of Comet Shoemaker-Levy 9 at perijove. Pongracic [1988] and Chyba *et al.* [1990] employed the geometry of spherical impactors upon plane surface-targets, whereas the others studied the collisional processes between self-gravitational spherical bodies.

The SPH method and associated programming techniques have been investigated and improved by many workers since the original work of Lucy [1977] and Gingold and Monaghan [1977].

The initial work of Gingold and Monaghan [1977] represented solid-body rotation, gravitational potential, and magnetic fields. Since then, material strength [Benz and Asphaug, 1993], radiation [Lucy, 1977, Monaghan, 1989], thermal conduction [Brookshaw, 1986, Monaghan 1988], and special relativity [Monaghan, 1985] have been incorporated into the SPH method.

The method had some problems relating to the stability of the shock fronts and their effect upon surrounding media. Tests of various kernel functions and the application of artificial viscosity have provided insights into obtaining improved shock stability and accuracy. To increase the performance, the "link lists" method [Benz, personal communication] or hierarchical "tree structure" method [Barnes and Hut, 1986] have been utilized. Several good reviews on SPH methods are available, including Benz [1989], Monaghan [1992], and Cloutman [1990]. In the following section, the fundamentals of the SPH method are outlined. Programming techniques and tricks to save CPU time are also discussed. In the last section of this chapter, some test results of the present code are presented.

2. Equations

The main innovation of SPH method is the use of point masses which are radially distributed via a kernel function. Fluid motion in an SPH code is described by the general equations of conservation of momentum, energy, and mass, and the EOS of the various media...... as in other problems of fluid dynamics. The physical properties of each particle - - - density, specific internal energy, and pressure, are calculated by summed quantities for each particle by weighted kernel functions. The latter contains a characteristic, distance, h, between particles. The fluid system is defined in terms of N spatially symmetric particles each with a mass of M. Particles are smeared out in space with the interpolation, or kernel, function, $W(\vec{r}-\vec{r_j},h)$, where h is the kernel width, and $\vec{r}$ and $\vec{r_j}$ represent an arbitrary field position and position of particle j, respectively.

The kernel function satisfies the conditions as follows:

(a) Integration over the space becomes unity,

$$\int W(\vec{r}-\vec{r_j},h)d\vec{r} = 1 \tag{1}$$

(b) The limit at $h \rightarrow 0$ is the δ function at $\vec{r}-\vec{r_j}$,

$$\lim_{h\rightarrow 0} W(\vec{r}-\vec{r_j},h) = \delta(\vec{r}-\vec{r_j}), \tag{2}$$

and (c) the function, W, and the first spatial derivative is continuous.

Then a function, $A(\vec{r})$, is defined as:

$$A(\vec{r}) \equiv \int\int\int A(\vec{r_j})W(\vec{r}-\vec{r_j},h)d\vec{r} \tag{3}$$

The right-hand side of the equation (3) is equivalent to

$$= \int\int\int \frac{A(\vec{r_j})}{\rho(\vec{r_j})} W(\vec{r} - \vec{r_j}, h)\rho(\vec{r_j})d\vec{r} \tag{4}$$

For the numerical evaluation, the equation (4) can be approximated by summation from the contribution from the element j with the mass, M_j, and the position of the center of the mass, $\vec{r_j}$. Then the function A at $\vec{r_i}$ is expressed as

$$A(\vec{r_i}) \simeq \sum_{j=1}^{N} M_j \frac{A(\vec{r_j})}{\rho(\vec{r_j})} W(\vec{r_i} - \vec{r_j}, h) \tag{5}$$

A is also differentiable using the differential kernel function, W, as

$$\nabla A(\vec{r_i}) = \sum_{j=1}^{N} M_j \frac{A(\vec{r_j})}{\rho(\vec{r_j})} \nabla W(\vec{r_i} - \vec{r_j}, h) \tag{6}$$

2.1 Mass conservation

The density as a function of radius from the center of a particle is directly described by replacing the function of $A(\vec{r_j})$ by $\rho(\vec{r_j})$ in the equation (5) such that

$$\rho(\vec{r_i}) = \sum_{j=1}^{N} M_j W(\vec{r_i} - \vec{r_j}) \tag{7}$$

An alternative way to calculate the density is to use the continuity equation which is expressed in terms of particle velocity, $\vec{v}$,

$$\frac{d\rho}{dt} + \rho\nabla \cdot \vec{v} = 0 \tag{8}$$

Equation (8) can be written in terms of the interpolation function as

$$\frac{d\rho(\vec{r_i})}{dt} = \sum_{j=1}^{N} M_j(\vec{v_j} - \vec{v_i})\nabla W(\vec{r_i} - \vec{r_j}) \tag{9}$$

[Monaghan, 1992]. Equation (9) is applicable to the boundary of a fluid without instability. When the equation (7) is used, the density drops artificially at a boundary and an instability occurs without the use of appropriate boundary conditions.

The application of equation (9) saves CPU time in calculations, since only one loop is required to solve the differential equations, for the conservation of momentum and mass, whereas a separate loop is required to calculate the density of particles using equation (7). Thus for greater numerical accuracy, equation (7) is recommended, whereas for the better performance, equation (9) has practical advantages [Monaghan, 1992]. For the applications in this thesis, Eq. (7) is used to assure mass conservation.

In the case where two different materials are treated in the code, such as atmospheric and rock materials, the density and internal energy are interpolated from all the particles independently of the material. The pressure is calculated assuming the EOS for the appropriate material of the particle.

2.2 Momentum conservation

As the purpose of this thesis is to describe problems of meteoroidal impacts onto planetary body surfaces, the essential forces in the equation of motion are: gravitational body forces and pressure gradients. The momentum equations for a non-rotating, inviscid fluid including shock dissipation term (artificial viscosity), q, is

$$\rho\frac{d\vec{v}}{dt} = \rho\vec{g} - \nabla(P + q) \tag{10}$$

and the particle velocity, $\vec{v}$, is

$$\frac{d\vec{r}}{dt} = \vec{v} \tag{11}$$

where $\vec{g}$ and P are the gravity and the pressure, respectively.

Various numerical expressions within the SPH formalism can be used to calculate $\nabla P/\rho$ [Gingold and Monaghan 1982]. To obtain a higher degree of accuracy, the relationship,

$$\frac{-1}{\rho}\nabla P = -\nabla\frac{P}{\rho} - \frac{P}{\rho^2}\nabla\rho, \tag{12}$$

is applied in the equation (10). By replacing $A = P/\rho$ and $A = \rho$ in equation (6), the right-hand side of the equation (12) becomes $2(P/\rho^2)M\nabla W$. To symmetrize the equation in terms of each i^{th} particle, and j^{th} particle, the numerical equation of momentum conservation becomes

$$\frac{d\vec{v}_i}{dt} = -\sum_{j=1}^{N} M_j(\frac{P_i}{\rho_i^2} + \frac{P_j}{\rho_j^2} + \Pi_{ij})\nabla_i W(|\vec{r}_i - \vec{r}_j|) + \vec{g}_i \tag{13}$$

where Π_{ij} is the coefficient term for the artificial viscosity, which is defined in a later section.

2.3 Energy conservation

Energy conservation under adiabatic conditions with the dissipation term is

$$\rho\frac{du}{dt} = -(P+q)\nabla\cdot\vec{v} \tag{14}$$

where u is the specific internal energy. Here, neither effects of radiation nor thermal conduction are taken into account; since we are interested in the initial phases of the impact process, these effects can be neglected. The numerical expression for the differential equation of the specific internal energy is obtained in a similar way as the equation of motion, and is given as:

$$\frac{du_i}{dt} = \frac{1}{2}\sum_{j=1}^{N} M_j(\frac{P_i}{\rho_i^2} + \frac{P_j}{\rho_j^2} + \Pi_{ij})(\vec{v}_i - \vec{v}_j)\cdot\nabla_i W(|\vec{r}_i - \vec{r}_j|) \tag{15}$$

The work done at $\vec{r}_i$ by the other particles at $\vec{r}_j$, due to compression or expansion of the materials, is summed for the change of the internal energy of the particle at $\vec{r}_i$.

2.4 Artificial viscosity

The point of employing artificial viscosity is to smooth out the shock discontinuities over a few grid points (or SPH particles) so as to avoid both infinite gradients at shock fronts and prevent the interpenetration of a particle into the other particles.

The coefficient of the artificial viscosity acting between particles i and j, Π_{ij}, is,

$$\Pi_{ij} = \frac{2}{(\rho_j+\rho_i)}[\beta\xi_{ij}^2 - \alpha\xi_{ij}(c_i+c_j)/2] \tag{16}$$

where c is the sound speed, $(\partial P_i/\partial \rho_i)^{0.5}$, α and β are constants, and ξ_{ij} is defined as

$$\xi_{ij} = min[(\vec{v}_i - \vec{v}_j) \cdot (\vec{r}_i - \vec{r}_j), 0] \frac{h}{[(\vec{r}_i - \vec{r}_j)^2 + \eta^2]} \tag{17}$$

$\eta^2 \sim 0.01h^2$, $\alpha \sim 1$, and $\beta \sim 2$ were found by Monaghan [1991] to yield stable results. The first β term of the numerator of equation (16) gives rise to an effective shear and bulk viscosity. The second α term is equivalent to Von Neumann-Richtmyer's [1945] viscosity. This was originally introduced for finite-difference calculations. This form of artificial viscosity permits conservation of linear and angular momentum. With the artificial viscosity of equation (16) and (17), the shock front spreads over a distance $\sim$ (2-3)h [Monaghan 1992].

Expressions of equation of motion (equation 1.13) and energy conservation (equation 1.15) involving particle expression of artificial viscosity become

$$\frac{d\vec{v}_i}{dt} = -\sum_{j=1}^{N} M_j(\frac{P_i}{\rho_i^2} + \frac{P_j}{\rho_j^2} + \frac{2}{(\rho_j + \rho_i)}[\beta\xi_{ij}^2 - \alpha\xi_{ij}(c_i + c_j)/2])\nabla_i W(|\vec{r}_i - \vec{r}_j|) + \vec{g}_i \tag{18}$$

and

$$\frac{du_i}{dt} = \frac{1}{2}\sum_{j=1}^{N} M_j(\frac{P_i}{\rho_i^2} + \frac{P_j}{\rho_j^2} + \frac{2}{(\rho_j + \rho_i)}[\beta\xi_{ij}^2 - \alpha\xi_{ij}(c_i + c_j)/2])(\vec{v}_i - \vec{v}_j) \cdot \nabla_i W(|\vec{r}_i - \vec{r}_j|) \tag{19}$$

2.5 Kernel function

Several interpolating functions satisfying the definitions of equations (1) and (2) are used in practice (Table 1.1). The most widely used kernel function is the Gaussian kernel (equation 1.20, below) [Gingold and Monaghan, 1977]. Several kernels based on the spline function [Monaghan and Lattanzio, 1985] are also widely applied. A Super-Gaussian function [Cloutman, 1990] can also satisfy equations (1) and (2).

Generally Gaussian kernel functions are spread over a wider region than spline functions with the same h. Spline kernels offers no interaction between particles beyond the region of $|\vec{r}_{ij}| = 2h$, while Gaussian and Super-Gaussian kernels require the interaction between particles within $\leq 3h$, and the contribution by the particles

Kernel Function	Function
Exponential Kernel[1]	$\frac{1}{\pi h^3}\exp\left(-\frac{\lvert\vec{r}\rvert}{h}\right)$
Gausian Kernel [2]	$\frac{1}{\pi^{3/2}h^3}\exp\left(-\frac{\lvert\vec{r}\rvert^2}{h^2}\right)$
Super Gausian Kernel [3]	$\frac{1}{\pi^{3/2}h^3}\left(2.5-\left(\frac{\lvert\vec{r}\rvert^2}{h^2}\right)\right)\exp\left(-\frac{\lvert\vec{r}\rvert^2}{h^2}\right)$
Spline Kernel [4]	$\frac{1}{\pi h^3}\left(1-1.5\left(\frac{\lvert\vec{r}\rvert^2}{h^2}\right)+0.75\left(\frac{\lvert\vec{r}\rvert^3}{h^3}\right)\right)$ (if $0 \geq \lvert\vec{r}\rvert \geq h$)
	$\frac{1}{4\pi h^3}\left(2-\frac{\lvert\vec{r}\rvert}{h}\right)^3$ (if $h \geq \lvert\vec{r}\rvert \geq 2h$)
	0 (otherwise)

Table 1. The main kernel functions for three-dimensional calculations are listed. h is the kernel width, and $\vec{r}$ is an arbitrary position vector. 1. Wood [1981], 2. Gingold and Monaghan [1977], 3. Monaghan [1992] and 4. Monaghan and Lattanzio [1985].

outside of the area is negligible [Pongracic, 1988]. The cut-off of the spline function restricts the number of particles involved at any point in the calculation, and results in faster computing. An unphysical negative value of W appears at some distances when Super-Gaussian is applied. Previously an exponential kernel [Wood, 1981] was also employed in astrophysical calculations. However, this kernel function spreads in space over a distance, $\sim 9h$. The particles within $\sim 9h$, then, are required to be involved in the summation [Table 1.1].

The Gaussian kernel employed in the series of calculations is:

$$W(\vec{r}) = \left(\frac{1}{\pi h^2}\right)^{d/2} exp(-|\vec{r}|^2/h^2), \tag{20}$$

where d is a dimension of the system.

The differential form of Gaussian kernel is:

$$\nabla_j W(\vec{r_i}-\vec{r_j}) = \frac{2(\vec{r_i}-\vec{r_j})}{h^2} W(\vec{r_i}-\vec{r_j}) \tag{21}$$

Material	ρ_0 [kg/m^3]	a	b	A_1 [GPa]	B_1 [GPa]	u_0 [MJ/kg]	A_2	B_2	u_s [MJ/kg]	$u_{s'}$ [MJ/kg]
Granite[⋆1]	2680	0.5	1.3	18	18	16	5	5	3.5	18
Water[⋆2]	998	0.7	0.15	2.18	13.25	7	10	5	0.419	2.69
Ice(hpp)[⋆2]	1293	0.3	0.1	10.7	65	10	10	5	0.773	2.04
Anorthosite(lpp)[⋆2]	294	0.5	1.5	71.	75	487	5	5	5	18

⋆1 : Allen [1967]
⋆2 : O'Keefe and Ahrens [1982]

Table 2. The parameters of the Tillotson equation of state for granite from Allen [1967], and water, ice, and anorthosite, from O'Keefe and Ahrens [1982].

The kernel width, h, should be $h \geq \frac{l}{2}$, and $h \simeq l$ is recommended by Cloutman [1990], where l is the size of particle. Monaghan [1988] assumed the kernel width h was a function of time and $h \propto (1/\rho)^d$, that is, $\propto (1/N)^{1/d}$. The condition of $h \ll l$ results in the ballistic motion of particles without any interaction between particles, and physically discontinuous materials are obtained.

3. Equation of State

The EOS is required to complete solving the differential equations discussed in the section 2. In our calculations, the Tillotson EOS [Tillotson, 1962] is employed for materials such as rock, water, and ice. The parameters for granite and for water, ice, and anorthosite are taken from Allen [1967] and O'Keefe and Ahrens [1982], respectively [Table 1.2].

Rocks are used to represent planetary surfaces and stony meteorites, and icy materials represent cometary bodies. The Tillotson EOS has three different phases. It represents the linear shock particle-shock velocity at the low pressure state (or the cold expanded state) and it extrapolates to the Thomas-Fermi limit at the high pressure state and compressed gas state. Between these phases, a smooth transition from the cold state to the hot state is achieved.

(a) The compressed stage to a higher density ($\rho > \rho_0$, where ρ_0 is a reference density) or the cold expanded state ($u < u_s$, where u is the specific internal energy and u_s is the specific incipient vaporization energy) is expressed as

$$P_c = (a + \frac{b}{\frac{u}{u_0 \eta^2} + 1}) u\rho + A_1 \mu + B_1 \mu^2, \tag{22}$$

where $\eta = \rho/\rho_0$, $\mu = \eta - 1$, u_0 is a parameter that is close to the vaporization energy, and a, b, A_1, and B_1, are material properties. Here $a + b = \gamma'(\rho_0)$, where γ' is the Gruneisen parameter at zero pressure.

In the cold state, the cutoff of the pressure at the low density states (that is, if $\rho/\rho_0 < 0.8 \sim 0.95$, $P_c = 0$) has to be applied to avoid the negative pressures.

(b) The expanded hot state ($\rho < \rho_0$ and $u > u'_s$, where u'_s is a complete vaporization energy) is expressed as

$$P_e = au\rho + (\frac{bu\rho}{\frac{u}{u_0 \eta^2} + 1} + A_1 \mu \exp(-B_2(\frac{1}{\mu} - 1))) \exp(-A_2(\frac{1}{\mu} - 1)^2), \tag{23}$$

where A_2 and B_2 are parameters. When $\eta \ll 1$, this equation becomes, approximately, that of an ideal gas.

(c) The transition between (a) and (b), that is, $u_s < u < u'_s$ and $\rho_0 > \rho$ becomes

$$P_t = \frac{P_e(u - u_s) + P_c(-u + u'_s)}{u'_s - u_s} \tag{24}$$

The Tillotson EOS is not able to describe a two-phase mixture of a material, such as solid and gas phases, correctly. Other equations of state, such as ANEOS [Thompson and Lauson, 1972] or SESAME [Lyon and Johnson, 1992], are designed for treating two phases simultaneously; however, the complication of the programming and thereafter the consumption of central processing unit (CPU) time are inevitable.

Benz *et al.* [1990] reported that the difference between using the ANEOS and the Tillotson EOS on the flow field was negligible, compared to other effects, such as the initial geometry of the particles, in their series of calculations of Moon formation.

For the atmosphere, an ideal gas EOS is employed,

$$P = \frac{\rho RT}{\mu'} = (\gamma - 1)\rho u, \tag{25}$$

where R is the gas constant, 8.31[J/mol k], and $R/\mu' = C_p - C_v = (\gamma - 1)C_v$, where C_p is the specific heat at constant pressure, C_v is the specific heat at constant volume, and μ' is the molecular weight. Here γ is C_p/C_v, or the polytropic exponent, where $\gamma = 1.2$ for CO_2 and $\gamma = 1.4$ for H_2.

The sound speed is obtained from the EOS of equations (22) - (25) with

$$c^2 = (\frac{\partial P}{\partial \rho})_s \tag{26}$$

To summarize this and the previous section, equations used in the code are equation (7), equations (18) and (19), and equation (20), to calculate densities of particles, to calculate the change of velocities and specific internal energies, and for the kernel function, respectively. The EOS discussed in this section (equation (22)-(25)) are also included to calculate the pressure of each particle.

4. Numerical Techniques

4.1 Time integration

To minimize computational time, it is convenient to control the time step. A suitable time step, δt, can be obtained from Courant - Friedrichs - Levy (CFL) criterion as

$$\delta t = \zeta min[(\frac{h}{c_i}), (\frac{h}{v_i}), (\frac{h}{\frac{dv_i}{dt}})^{0.5}] \tag{27}$$

where ζ is a constant. To obtain reasonable accuracy, ζ should be $\simeq 0.25$ [Gingold and Monaghan, 1983], or ≤ 0.5 [Cloutman, 1990].

ζ	3rd order [%]	4th order [%]
0.25	0.04	0.01
0.5	0.3	0.06
0.67	-	0.3
0.75	0.9	0.55

Table 3. The dependence of the deviation on the order of Runge-Kutta integrator and the parameter of CFL condition, ζ. The third and the fourth order of Runge-Kutta integrator are compared. The fourth order integrator is more accurate with the same proportional constant, ζ. A larger value of ζ can be applied for a higher order integrator to obtain the same accuracy.

Numerical integration of equations (13) and (15) is generally conducted using a predictor-corrector or leapfrog method [Monaghan and Gingold, 1983]. The fourth-order predictor-corrector method was first used by Wood [1981]; however, most of the applications are carried by the second-order method, because only two iterations, with single computation of momentum calculation per cycle, is required. Benz employed a second-order Runge-Kutta method with an adaptive time step [Benz 1989]. Although this required two stages of evaluation of forces for each SPH particle, the time step can be taken $\sim$ 3 times larger than using other integrating methods.

In this thesis, the fourth-order Runge-Kutta method is performed to integrate the ordinary differential equations of equation (13) and (15). It requires four integrations in one time step and results in consuming about twice as much CPU time as the second order integrator. However, a much wider range of time steps can be achieved for a given cycle. Thus a larger value of ζ can be used to obtain the same accuracy. In Table 1.3, the errors in the total energy conservation which resulted from the impact calculations employing a third- and fourth-order Runge-Kutta integrator are compared.

Here the errors represent the deviation from the initial total energy of the system after $\sim$ 400 cycles. If the order is reduced, a smaller time step is required to obtain the same accuracy. As a result, the total time to calculate a problem to a given real time duration becomes similar in both cases. Depending on problems, an average, $\zeta > 1.5 \sim 5.0$, or more, can be achieved with the fourth-order Runge-Kutta integrator. The advantage of using the high-order Runge-Kutta method is that we can adjust the accuracy by simply changing the constant, ζ, rather than changing the logic of integrator.

4.2 Boundary conditions

To construct a target from a collection of particles, these are initially placed within a hemispherical or rectangular parallelepiped container for a planer half-space. In all cases, we employ mirrored symmetry and utilize one-half or approximately one-eighth of the particles in actual problem in our calculation. Velocities of particles at the outer edge of the target box (both on the lateral edges and the bottom) are set to zero at all the times, so that the target is confined by a solid reflective wall. This boundary condition restricts the duration of the calculation, since an unphysical reflection wave is produced at the boundary of the target box, when the shock wave reaches a lateral or bottom boundary.

4.3 Initial conditions

In a gravity field, the positions of target particles, such as these at the planetary surfaces, need to be hydrostatically stabilized before the main program calculation is performed. Two methods are used to define the initial position and the mass of particles.

1. All particles are assumed to have the same mass and we pre-set the vertical distances between particles so these are in hydrostatic equilibrium.

2. All particles are located at the equal distances. However, the mass of particles

at a given height are initially set to be proportional to the density at the expected particle position.

The advantage of the approach 1. is that it is not necessary to handle particles with different masses and the resulting unphysical motion due to the collision of particles with different masses. The disadvantage of approach 1 is that, in a gravity field, particles are compressed at depth and their positions can not be resolved. If the number of particles in the vertical direction exceeds ~ 20, this problem is encountered in the terrestrial gravity field. Therefore, the distribution of particles along the gravity field has to be decided by the spatial resolution and accuracy desired.

Either method of initializing particles can be used to set particles in their initial position. The initial configuration can be examined by repeatedly setting all velocities to zero after $\sim 10^2$ iterations. This pre-run test of the stability of initial positions avoids excessive oscillation and unphysical motion once a full-scale calculation has begun.

4.4 Tree code

Direct calculation of the motion of SPH particles uses CPU time in proportion to the square of the number of particles ($\propto N^2$), as all force calculations for N particles required summation over N particles. The larger the number of particles employed in a calculation, the better resolution is achieved. As N increases, however, this results in a large increase of computational time. Therefore, it is desirable to involve as many particles as possible without increasing the computational time. Since direct calculation of N particles with N particles is not practical for large number of N, a hierarchical tree structure has been developed [Barnes and Hut, 1986]. The tree structure method relates all the particles as "a tree" by classifying their position. The tree framework is used to identify neighbor particles of any given particle. This bookkeeping method of keeping track of neighbor particles is required in every time step. However, forces from interaction with distant particles are thus skipped, and CPU time is saved. Utilizing a tree structure requires CPU time in proportion to $(N \log N)$.

In cases of involving randomly distributed particles interacting with a self-gravitational force, Benz et al. [1988] suggested that for calculations involving particles when $N > 2000$ on a CRAY YMP or $N = 200$ on a SUN SPARC (10) station, the tree code is more effective in saving CPU time. In the applications of this thesis, the positions of particles are well ordered initially, and the relative positions of most particles remain close to the initial positions even after an impact. Therefore, the sequential access to particle arrays in memory is less time consuming than random access. Moreover, most parts of the present code including tree construction can be vectorized, when employing a vector machine, such as CRAY-YMP [Makino, 1990]. Therefore, the number of particles with which the tree code is more effective than the direct summation method has changed. In practice, in our case, if the number of particles involved in the calculation is more than $\sim 10^4$, the tree method is more effective than the direct summation of all particles on the CRAY machines we used. In the next section, the detail analyses of performance, which depend upon programming logic, and the number of particles, are discussed.

4.5 Performance tests

In this section, the performance of the present code on various machines is tested. The CPU time for a single cycle of the calculation as a function of number of particles and logic are shown in figure 1.

We employed a CRAY-YMP, CRAY-C90, and SUN Sparc 10 as test machines. Programs running on CRAY-YMP and -C90 were maximally vectorized. The dotted line represents an N^2 slope, which represents the direct summation method, whereas the dashed line represents an NlogN slope, which characterizes the performance of a

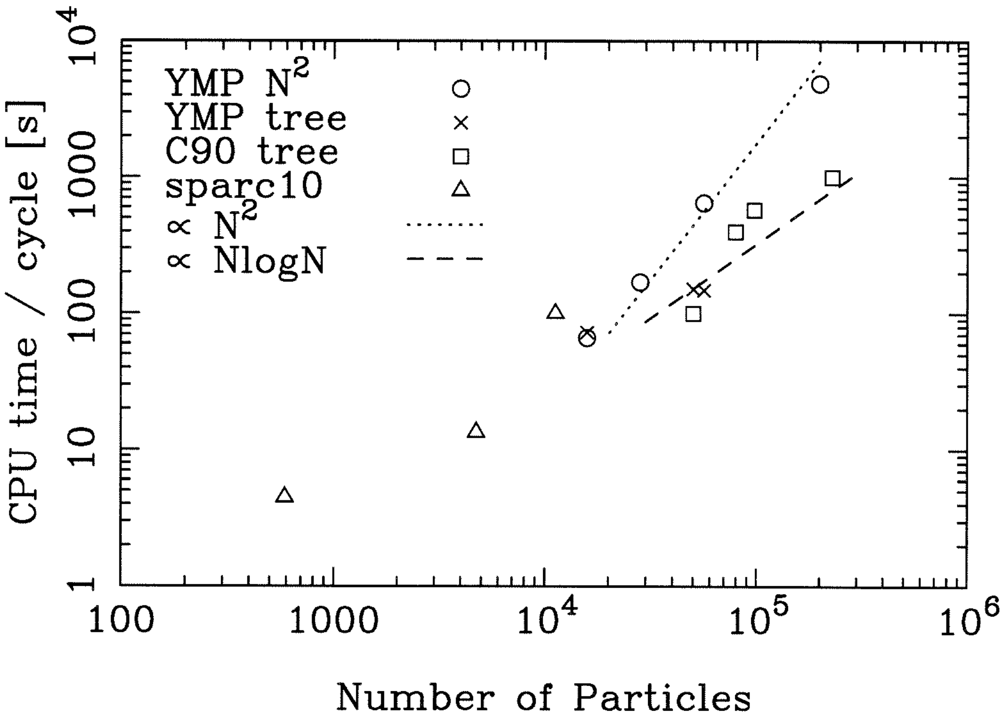

Figure 1. Central processing unit (CPU) time [s] for a cycle as a function of number of particles (N) is shown. ○ represents the CPU time on CRAY-YMP using the direct summation method; × represents the CPU time on CRAY-YMP using the tree structure; □ represents the CPU time on CRAY-C90 using the tree structure; and △ represents the CPU time in SUN Sparc 10 using the direct summation method. The dotted line represents an N^2 slope, whereas the dashed line represents an NlogN slope, which characterizes the performance of the tree structure. If symmetry is taken into account, the actual CPU time is decreased by factor of 2 and 8 for oblique- and normal-impact.

tree structure. Some results of a tree code calculation do not fall along the NlogN line, because computational performance also depends on the size of the original memory employed to construct a tree. Recent performance data announced by the CRAY Co. show that their C90 machine runs at ~ 1000 Mflops. This is some three times faster than YMP (333 Mflops). If the number of total particles becomes N> 10^4, the tree-structured code is more effective than a vectorized code using a direct summation method on the CRAY machine. The tree-structured code without any vectorization is not effective in saving computer time on the CRAY machine.

The characteristic of symmetry of the target and the impactor can reduce the number of particles involved in a calculation. As already mentioned, in the case of oblique impact, only particles in a half space (0.5N) need to be considered. By using the symmetry of the plane along the impact trajectory, the physical parameters of the particles are reflected to the particles in the other half-space. In the case of normal impacts, only $\sim 1/8$ of N particles need to be employed. Therefore, the symmetry of the problem can save considerable computational time.

Until a particle 'feels' some movement from the propagation of shock waves, the particle does not need to be employed in the calculation. Therefore, calculations can begin using only a small portion of the complete target. The target box can be expanded gradually to take into account the larger space encompassed by the original particles' motion at later times. This method saves enormous quantities of CPU time.

5. Numerical Tests

5.1 One-dimensional shock propagation

Several comparisons with analytic solutions are performed to test the present SPH code. The first test is performed for plate to plate impact. The propagation of the shock wave and the physical parameters are compared with analytical solution of the impedance match method. The impedance match method describes the propagation of a one-dimensional shock wave upon planar impact of one material upon another [from Ahrens 1987]. The present SPH code employs the Tillotson EOS; however, for the shock properties in the compressional stage of solid materials, the Tillotson EOS virtually duplicates the linear shock velocity-particle velocity relation (Eq. 1.28). If the projectile and the target are of the same materials, the propagation

c_0[km/s]	s	ρ_0[kg/m^3]
3.68	1.24	2630

Table 4. The shock parameters for granite from Melosh [1990] in which the data from Kieffer and Simonds [1980] is manipulated.

speed of a shock wave is empirically described as

$$U_s = c_0 + s u_p \tag{28}$$

where u_p is the particle velocity, and $u_p = 0.5V_i$, where V_i is the impact velocity. Hugoniot equations prescribe shock pressure, P, and shock density, ρ, as

$$P = \rho_0 U_s u_p \tag{29}$$

and

$$\rho = \rho_0 \frac{U_s}{U_s - u_p} \tag{31}$$

respectively. The parameters used to calculate shock properties of granite are shown in Table 1.4.

One of our results is shown in figure 2. Here the projectile and the target are described by 10 × 10 particles, in width, parallel to the impact surface and 30 particles in length along the impact direction. The initial distance between particles, d, is 1 km. Both materials are granite and the impact velocity is 10 km/s. The kernel width, h, used is the original particle distance, that is 1 km, and a constant mass for every particle is assumed. Since a one-dimensional shock wave is considered, lateral motion is not taken into account. Particle position, density and pressure profiles along the impact direction are shown as a function of time after the impact in the figure 2. The calculated positions of the shock wave and the boundary between the projectile and the target are shown via dashed lines and dotted lines. Initial density, the shock compressed density and the pressure calculated from equation (30) and (31) are indicated with solid lines in figure 2 (b) and (c). The shock discontinuity is confined to $\sim$ 2-3 particles. The difference between the average shock density and pressure calculated in our code and those of analytical solutions are several percent. Some instability in the shocked region is observed; however, the amplitude of the instability in the pressure and density profiles is less than $\pm \sim 10$ %. We conclude that the SPH code can represent physical properties properly within these errors.

The effect of varying the kernel length, h, was also tested. If $h \simeq 2d$ is assumed, although the wavelength of the oscillation of shocked properties increases, the shocked region becomes smoother than the case of $h \simeq d$. In this case, a shock front became more widely distributed and to properly describe the shock front requires more particles. On the other hand, if $h \leq 0.5d$ is used, the shocked material properties oscillate with amplitudes greater than $\pm$ 10% with respect to their mean value. However, in this case, a shock front is well defined over a length scale of $\leq 2d$. A compromise configuration with h $\sim$ d is employed in this thesis. The effect of changing impact velocity, materials, EOS's, and varying dimensions were also tested for impact. Variation in these parameters had no effect other than those already mentioned.

5.2 Three-dimensional shock propagation

Impact problems in the three dimensions were also examined. The impact of spherical projectiles onto a half-space planar target was previously described using the axisymmetric Lagrangian finite-difference (HELP) code [Ahrens and O'Keefe, 1977]. As in Ahrens and O'Keefe [1977], the SPH code was used to study the impact of a 10 km-diameter projectile at impact velocities (V_i) of 15 and 45 km/s. The Tillotson EOS for anorthosite was used for the projectile and the target. The problem studied by Ahrens and O'Keefe [1977] was thus run with the present three-dimensional SPH

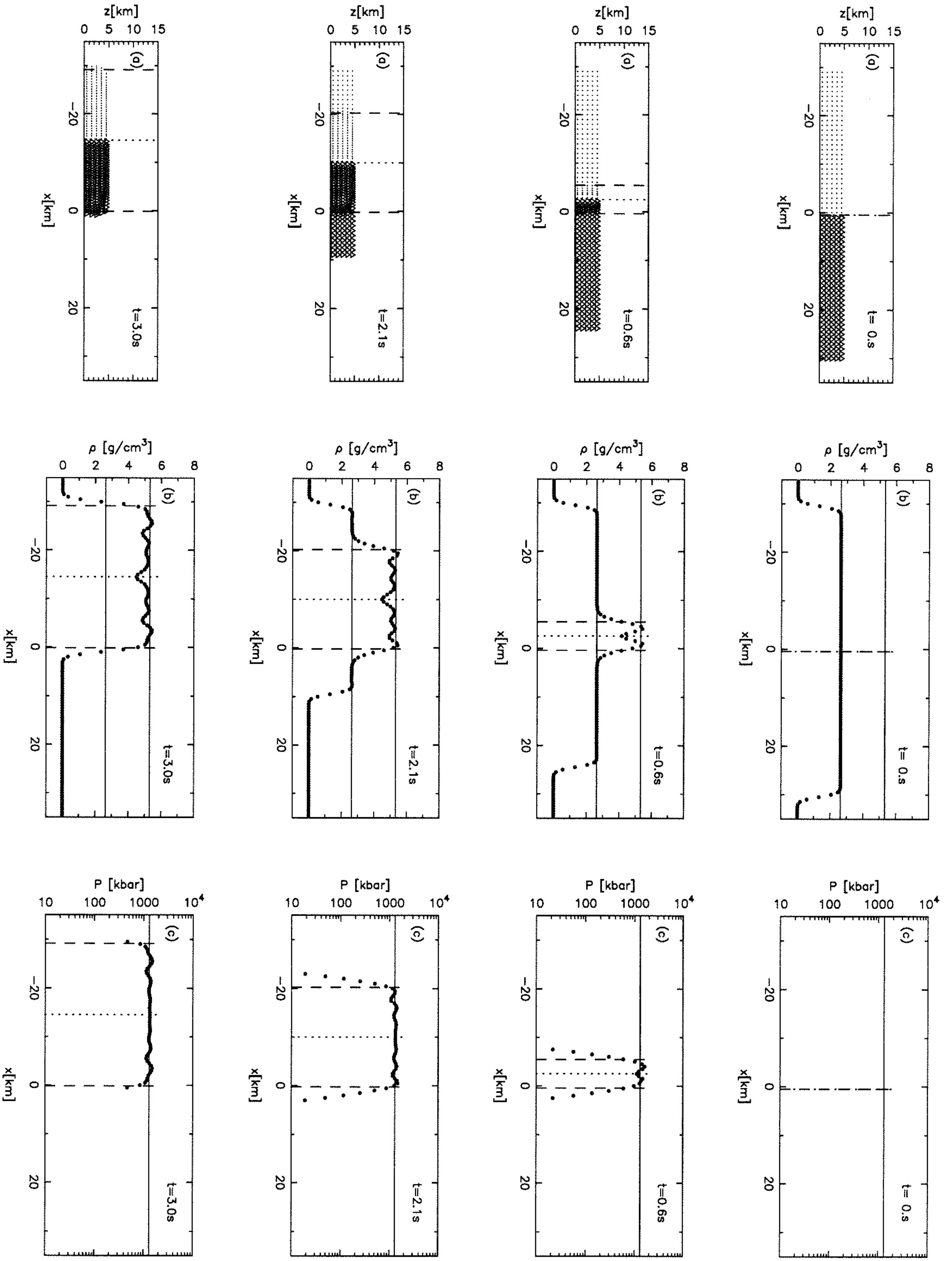

code. The peak shock pressure as a function of the target depth, *d*, for the two

Figure 2. One dimensional numerical test for the shock propagation. Projectile-target position, density, and pressure profiles for impact of granite projectile into target at 10 km/s. (a) half-space particle positions, (b) density and (c) pressure profiles at same times 0., 0.6, 2.1, and 3.0 seconds from the top to the bottom. The projectile and the target are described by 10 × 10 particles in width (impact surface) and 30 particles in length (impact direction). The analytically calculated positions of the shock wave and the boundary between the projectile and the target are shown in dashed lines and dotted lines, respectively. (a) Triangles and dots represent the projectile and the target particles, respectively. (b) and (c) The initial density (2.63 g/cm^3) and the yields impedance match solution (a shock density of 5.32 g/cm^3 and a shock pressure of 1300 kbar) are shown with solid lines. Both profiles are calculated every 0.5 km distance and shown with large dots.

codes are compared in figure 3. In figure 1.3 (a), the positions of particles in the center plane are shown. In this case, the radius of the projectile is equal to 4 particle spacings. In figure 3 (b) and (c), the pressure profiles for V_i equal to 15 and 45 km/s are described with dotted lines. The solid lines are the peak pressure profiles from Ahrens and O'Keefe [1977]. The dashed lines are a fit to the peak pressure of the results of the SPH code. The results of impedance matching for the impact velocities are shown with arrows in both cases. To conserve radial momentum of the detached shock wave, if it were ideally hemispherical, the peak pressure should theoretically attenuate in proportion to d^{-2}, where d is radial depth. Therefore, for comparison, the slope of d^{-2} is also shown with a dashed line in an arbitrary position in figure 3(b) and (c).

At the depth less than <2R (R is projectile radius), both the Lagrangian finite-difference code and SPH code agree very well, and they also agree with the analytical impedance-match solution. The difference of the peak pressure in the near field between two codes is less than ~ 15%. However, in the far-field, the shock attenuation described by the SPH code is less dependent on impact velocity than that of the finite-difference code. The peak pressure differs by a factor of 2 to 4 at 10 R in the three-dimensional SPH code, versus, the two-dimensional axisymmetric HELP code. Even if the number of particles in the projectile is increased, the pressure profiles from the SPH code do not change dramatically. The powers of attenuation slopes in the far field are -3.0, -2.0, and -1.45, for V_i = 45, 15, and 5 km/s, respectively, in the case of HELP calculations, whereas these are -2.1 and -1.75 for V_i = 45 and 15 km/s in the case of SPH calculations. We note that the intersection of the near and far-field attenuation regime for the SPH code has less dependence on impact velocity than in the case of the finite-difference code.

The benchmark test performed between an axisymmetric SPH code and Sandia's CTH (Eulerian) code for the same initial conditions, physical parameters, and resolutions shows that the energy is attenuated somewhat more rapidly with distance in the CTH code than in an SPH code similar to ours [Boslough et al. 1994]. We conclude that slight differences exist between currently used simulation codes. These differences, some of which are highlighted above, are attributed to the characteristics of codes.

The interaction between particles obtaining different masses is treated in the series of SPH numerical simulations. This can be tested in the case of the entry of a comet into the Jovian atmosphere [Takata et al., 1994]. The mass of a cometary particle is set $> 10^2$ times that of an atmospheric particle, however the atmospheric pressure in the cometary front surface is in the same order of the ram pressure, $\rho_0 V_i^2$. Therefore even if particles with different masses are treated in a code, results are still valid.

6. Conclusions

The SPH method used for a series of impact calculations is tested. From the performance tests, the tree-structure method for vectorization of the code can be applied when the number of particles, $N, > 10^4$. Most of the calculations we performed used a CRAY-YMP at the Jet Propulsion Laboratory or the CRAY-C90 at Goddard Space Flight Center. Tests of one-dimensional shock propagation show that the de-

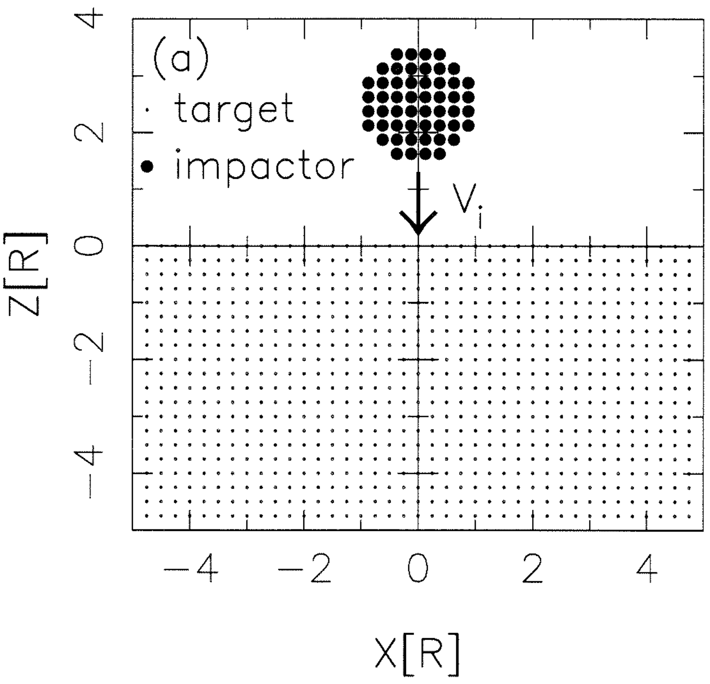

Figure 3. Three-dimensional test of the present SPH code. Peak shock pressures as a function of depth calculated for impact of spherical projectile onto target half-sphere using present three-dimensional SPH code. The results are compared with the one using axisymmetric Lagrangian code [Ahrens and O'Keefe, 1977]. The impactor size is 10 km. The Tillotson EOS of the anorthosite is used. (a) the initial particle position in the center plane. Here · and • symbols represent target and impactor particles, respectively. In (b) and (c), the pressure profiles for $V_i = 15$ and 45 km/s as functions of depth and various time (from (1) to (8) for (b) and (10) for (c)). The results of impedance matching are shown with arrows. ··o·· shows the pressure profiles at the center of the target. The solid lines and dashed lines represent peak pressure profiles from Ahrens and O'Keefe [1977] and a fit of the peak pressure of SPH results. In the near field at the depth, less than <2R, both the Lagrangian code and SPH attenuation agree closely. In the far field, however, the SPH results yield an attenuation rate $\propto d^{-1.75}$ and $d^{-2.1}$, whereas the Lagrangian code yields $\propto d^{-2.0}$ and $\propto d^{-3.01}$ for $V_i = 15$ and 45 km/s, respectively.

Figure 3 - continued

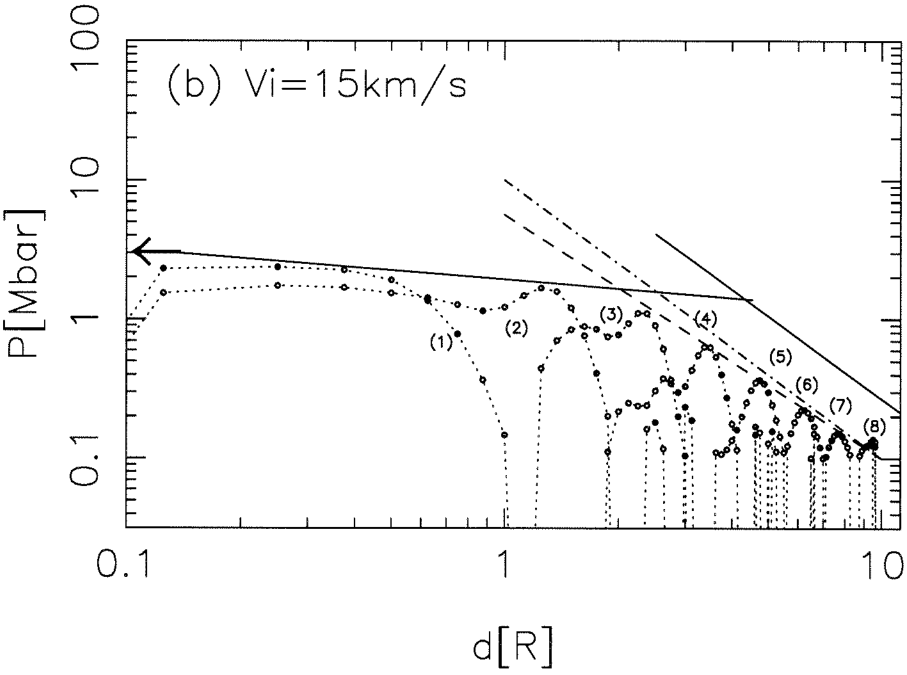

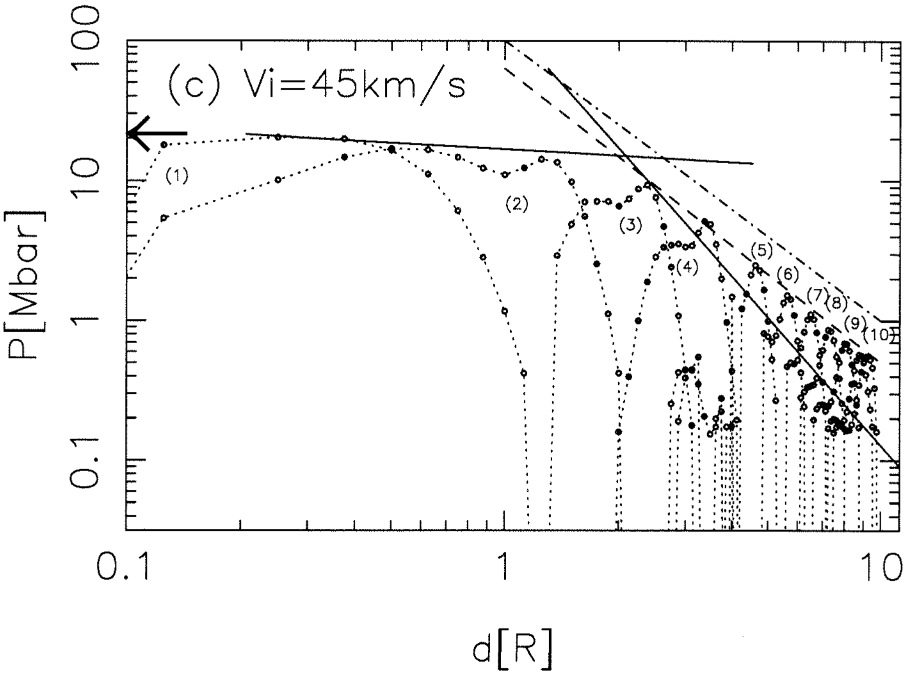

Impact velocity [km/s]	this work	Ahrens and O'Keefe [1977]
15	-1.75	-2.0
45	-2.1	-3.0

Table 5. Power coefficients for attenuation rate, q, where q represents P $\propto d^q$, in far fields of SPH calculation and HELP simulation are compared.

veloped code yields an error of only several percent in density or pressure, when the numerical solutions are compared with the analytical impedance-match solution. For spherical three-dimensional impact, near the impact point, the attenuation of shock pressure and the compression calculated by the SPH code are very similar to the results of a previous finite-difference code. The attenuation in the far-field (10 projectile radii) differs such that the pressure is a factor of 2 to 4 greater for SPH code relative to the previous two-dimensional axisymmetric finite-difference code results.

References

Ahrens, T. J., 1987. Shock Wave Techniques for Geophysics and Palanetary Physics. in *Methods of Experimental Physics, vol. 24A*, F. G. Sammis and T. L. Henyey, eds. Academic Press, London, p185-236.

Ahrens, T. J. and J. D. O'Keefe, 1977. Equation of State and Impact-Induced Shock-Wave Attenuation on the Moon in *Impact and Explosion Cratering*, Roddy, D. J., Pepin, R. O., and Merrill, R. B., eds. Pergamon Press, New York, p639-656.

Allen, R. T., 1967. (The data from Melosh, 1990.) Equations of State of Rocks and Minerals. *Interim Report to DASA*, DA49-146-XZ-462. *General Dynamics Report*, #GA MD 7834.

Asphaug, E. and W. Benz, 1994. Density of Comet Shoemaker-Levy 9 Deduced by Modeling Breakup of the Parent Rubble-Pile. *Nature*, **370**, 120-124.

Barnes, J. E. and P. Hut, 1986. A Hierarchical O(NlogN) Force-Calculation Algorithm *Nature*, **324**, 446-449.

Benz, W., 1988. Application of Smooth Particle Hydrodynamics (SPH) to Astrophysical Problems. *Com. Phys. Comm.*, **48**, 97-105.

Benz, W., 1989. Smooth Particle Hydrodynamics: A Review. In Numerical Modeling of Stellar Pulsation: Problems and Prospects. NATO Workshop, Les Arcs, France.

Benz, W. and E. Asphaug, 1994. Impact Simulation with Fracture 1., Method and Tests. *Icarus*. **107**, 98-116.

Benz, W., A. G. W. Cameron, and H. J. Melosh, 1990. The Origin of the Moon and the Single Impact Hypothesis -III, *Icarus*, **81**,113-131.

Benz, W., W. L. Slattery, and A. G. W. Cameron, 1986. The Origin of the Moon and the Single Impact Hypothesis - I, *Icarus*, **66**, 515-535.

Benz, W., W. L. Slattery, and A. G. W. Cameron, 1987. The Origin of the Moon and the Single Impact Hypothesis -II, *Icarus*, **81**, 113-131.

Benz, W., W. L. Slattery, and A. G. W. Cameron, 1988. Collisional Stripping of Mercury's Mantle, *Icarus*, **74**, 516-528.

Brookshaw, L., 1986. A Method of Calculating Radiative Heat Diffusion in Particle Simulations, *P. Ast. S. A*, **6**, 207-210.

Chyba, C. F., P. J. Thomas, L. Brookshaw, and C. Sagan, 1990. Cometary Delivery of Organic-Molecules to the Early Earth, *Science*, **249**, 366-373.

Cloutman, L. D., 1990, Basics of Smoothed Particle Hydrodynamics. Lawrence Livermore National Lab., UCRL-ID-103698, pp.47.

Gingold, R. A. and J. J. Monaghan, 1977. Smoothed Particles Hydrodynamics: Theory and Application to Non-Spherical Stars, *Mon. Not. R. Astr. Soc.*, **181**, 375-389.

Gingold, R. A. and J. J. Monaghan, 1983. On the Fragmentation of Differentially Rotating Clouds. *M. Not. R. Ast.*, **204**, 715-733.

Kieffer, S. W. and Simonds, C. H., 1980. The Role of Volatiles and Lithology in the Impact Cratering Process. *Rev. Gephys. and Space Phys.*, **18**, 143-181.

Lucy, L. B., 1977. A Numerical Approach to the Testing of the Fission Hypothesis. *Astron. J.* **82**, 1013-1024.

Lyon, S. and J. D. Johnson, 1992. SESAME : The Los Alamos National Laboratory Equation of State Data Base, *Los Alamos National Laboratory Report*, LA-UR92-3407.

Makino, J., 1990. Vectorization of a Treecode. *J. Comp. Phys.*, **87**, 148-160.

Melosh, H. J., 1990. Impact Cratering, A Geologic Process. Oxford University Press, New York, pp.245.

Monaghan, J. J., 1985. Particle Methods for Hydrodynamics, *Comp. Phys. Res.*, **3**, 71-124.

Monaghan, J. J., 1988. An Introduction to SPH, *Comput. Phys.*, **48**, 89-96.

Monaghan, J. J., 1992. Smoothed Particle Hydrodynamics, *Ann. Rev. Astro.*, **30**, 543-574.

Monaghan, J. J. and R. A. Gingold, 1983. Shock Simulation by the Particle Method SPH. *J. Comp. Phys.*, **52**, 374-389.

Monaghan, J. J. and J. C. Lattanzio, 1985. A Refined Particle Method for Astrophysical Problems, *Astron Astr*, **149**, 135-143.

O'Keefe, J. D. and T. J. Ahrens, 1982. Cometary and Meteorite Swarm Impact on Planetary Surfaces. *J. Geophys. Res*, **87**, 6668-6680.

Pongracic, H., 1988. Numerical Modelling of Large Body Impacts. *Ph.D. Thesis*, Monash Univ., Australia, 1988.

Smither, C. L., Three-Dimensional Modeling of Planetary Impacts, *Ph.D. Thesis*, Caltech, Pasadena, 1992.

Stellingwerf, R. F., 1990. Smooth Particle Hydrodynamics. *Lecture Notes in Physics, 395, Advances in the Free-Lagrange Method*, Springer-Verlag, Heidelberg FRG, 239-247.

Thompson, S. L. and H. S. Lauson, 1972. Improvements in the Chart D Radiation - Hydrodynamic CODE III: Revised Analytic Equation of State. Sandia National Laboratory Report, SC-RR-71-0714.

Tillotson, J. H., 1962. Metallic Equations of State for Hypervelocity Impact. *General Atomic Report*, GA-3216.

Wood, D., 1981. Collapse and Fragmentation of Isothermal Gas Clouds. *Mon Not R. Astr. Soc*, **194**, 201-218.

PAPER II

Comet Shoemaker-Levy 9: Impact on Jupiter and Plume Evolution

Comet Shoemaker-Levy 9: Impact on Jupiter and Plume Evolution

Toshiko Takata, John D. O'Keefe, Thomas J. Ahrens

Division of Geological and Planetary Sciences
California Institute of Technology
Pasadena, California 91125

and

Glenn S. Orton

Jet Propulsion Laboratory
California Institute of Technology
Pasadena, California 91109

Icarus, vol. **109**, page 3-19

Abstract

The impact of fragments of Comet Shoemaker-Levy 9 on Jupiter and the resulting vapor plume expansion are investigated by conducting three-dimensional numerical simulations using the Smoothed Particle Hydrodynamics (SPH) method. An icy body, representing the cometary fragments, with a velocity of 60 km/sec and a diameter of 2 km can penetrate to 350 km below the 1-bar pressure level in the atmosphere. Most of the initial kinetic energy of the fragment is transferred to the atmosphere between 50 km and 300 km below the 1-bar pressure level. The shock-heated atmospheric gas in the wake is totally dissociated and partially ionized. Scaling our SPH results to other sizes indicates that fragments larger than ~ 100 m in diameter can penetrate to below the visible cloud decks. The energy deposited in the atmosphere is explosively released in the upward expansion of the resulting plume. The plume preferentially expands upward rather than horizontally due to the density gradient of the ambient atmosphere. It rises $\geq 10^2$ km in $\sim 10^2$ seconds. Eventually the total atmospheric mass ejected to above 1 bar is ≥ 40 times the initial mass of the impactor. The plume temperature at a radius $\sim 10^3$ km is $> 10^3$ K for 10^3 seconds, for a 2-km fragment. We predict that impact-induced plumes will be observable with the remote sensing instruments of the Galileo spacecraft. As the impact site rotates into the view of the earth some 20 minutes after the impact, the plume expansion will be observable using the Hubble Space Telescope and from visible and infrared instruments on ground-based telescopes. The rising plume reaches ~ 3000 km altitude in $\sim$ ten minutes and will be visible from the earth.

1. Introduction

Comet Shoemaker - Levy 9 (SL-9) was discovered in March 1993 [Shoemaker et al., 1993]. Upon discovery, it was found to be highly fragmented, apparently as a result of a 1992 close passage (within the Roche Limit) of Jupiter. The fragments lie along a line, and are on a trajectory which will impact Jupiter between July 16 and 22 [Yeomans and Chodas, 1993]. Some 21 discrete fragments each exhibiting separate cometary comae have been reported by Jewitt et al. [1993].

Fragment sizes are still in debate. Observations with the Hubble Space Telescope (HST) indicate that the maximum fragment size is $\sim$ 4.3 km and 11 fragments are $\sim$ 3 km in size [Weaver et al., 1994]. Analytical modeling of tidal disruption and observation of the separation distance versus time of the comet fragments predicted that the original comet was $\sim$ 2 km in diameter [Scotti and Melosh, 1993]. Sekanina et al. [1994] derived, with slightly different assumptions, an initial diameter of 8-10km, similar to the upper limit obtained by HST observations. In either case, the total energy deposited in the Jovian atmosphere by the impact will be 10^{29} - 10^{31} erg; that is the equivalent of $\sim$ 10^6 - 10^9 Mtons of TNT. This is much larger than any explosion or impact observed on the earth (10^{23}-10^{24} erg: e.g., 60 Mton Soviet nuclear atmospheric explosion, 1908 Tunguska event) and it is comparable in energy to the Cretaceous-Tertiary extinction bolide [Alvarez et al., 1980]. Although SL-9 has visible comae [Shoemaker et al., 1993], no OH^- emission has been detected from the HST observation [Weaver et al., 1994]. Therefore, it is not clear whether it is a comet or an asteroid in origin. Yeomans and Chodas [1993] calculated an impact angle of 42° from the zenith and an impact velocity of 60 km/s. They predicted that the impact site will be 47-49 South latitude and it will be visible from the earth some 20 minutes after the impact. A scientifically interesting opportunity exists to observe the post-impact plume from the earth and the instruments on the Galileo spacecraft.

In this paper, we predict the post-impact state on Jupiter using pre-impact observational data. The impact mechanics during entry into the Jovian atmosphere and the possible post-impact effects including mass transport of the comet and atmosphere, and dimensions of the plume expansion are interest to potential observations. In order to investigate the SL-9 encounter with Jupiter and resulting post-impact phenomena, two stages of numerical simulations are employed. In the first stage, the entry of the comet into the Jovian atmosphere is modeled and the process of cometary mass shedding via hydrodynamic instabilities and disintegration of the comet are examined. We predict the distribution of the energy deposition in the atmosphere and the penetration depth of the cometary materials upon impact. In the second stage, the evolution of energy distribution by mass transport and the resultant plume are calculated with emphasis on the remote observable radiation characteristics.

2. Simulation Method

We used three-dimensional numerical simulations that employed to the Smoothed Particle Hydrodynamics (SPH) method. This technique has been applied to many astronomical problems [Lucy, 1977, Monaghan, 1992] and some engineering problems [Cloutman, 1990, Stellingwerf, 1990]. The SPH method is a fully Lagrangian particle method and treats materials as a collection of particles. Each particle mass spread out in the space according to a spatial distribution kernel function. Basically all the interactions of particles are calculated for the physical variables of each particle in each time step. The SPH formulation in Monaghan [1992] with the Gaussian kernel function was employed in our code.

Our code was tested by comparing results with one-dimensional shock wave analytical solutions (impedance matching) for impacts of granite on granite for a wide range of impact velocities (5 - 40 km/s). We found that the code had an error less than 3% in shock pressure. We also compared the results of three-dimensional calculation for the impact of a spherical projectile onto a planetary surface at the impact velocities of 5 to 45 km/s with the results of an Eulerian calculational scheme used by O'Keefe and Ahrens [1977] and Ahrens and O'Keefe [1977]. Both peak shock pressure profiles as a function of time agreed to within 15%.

Since the stagnation pressures encountered in the Jovian atmosphere are much greater than the expected yield strength of the comet (expected strength value is less than 100 bar), we didn't include it. Radiative heat transfer is not included, since in the Jovian atmosphere, methane is abundant, and this will result in an optically thick atmosphere at infrared wavelengths. Therefore, for the present short time scales ($< 10^2$ s), these assumptions are reasonable.

The thermal properties of materials, particles are characterized by their equation of state. For the cometary fragments, the Tillotson equation of state (EOS) for ice was used, with an initial density of 1 g/cm^3 [O'Keefe and Ahrens, 1982]. The Tillotson EOS provides the thermal properties of compressed and expanded phases of H_2O over a wide pressure range. The EOS is obtained from fitting shock-wave experimental data up to $\sim$ 1 Mbar and employing Thomas-Fermi theory above that pressure. For the atmosphere, an adiabatic ideal gas with the specific heat ratio $\gamma = C_P/C_V = 1.4$ is employed. Since neither dissociation nor ionization are taken into account in the ideal gas, the atmospheric temperature and pressure obtained in our calculations will be the upper bound.

The model of the atmospheric structure is derived from a smoothed average of the ingress and egress of the Voyager-1 radio occultation experiment [Lindal et al. 1981], assuming a mean molecular weight derived from the bulk composition which is 89% H_2 and 11% He by volume at all altitudes [Gautier et al. 1981]. At pressure greater than 1-bar, the temperature was derived assuming dry adiabatic conditions. The altitude is set to 0 km at the 1-bar pressure level. Constant Jovian gravity of

2325 [cm/s^2] is used in all the calculations.

Two sizes of comet fragments, 2 and 10 km in diameter, are investigated for the comet-entry model. An impact velocity of 60 km/s and an impact angle of 40° from the zenith are assumed for the comet entry. These two sizes encompass a possible range of the minimum and maximum fragment size of the largest fragment of SL-9. For the plume evolution, a cometary impactor of 400 m diameter, in addition to two diameters of impacts, i.e., 2 and 10 km, are examined. This size variation provides 4 orders of magnitude difference in impact energy and bound to expected range of cometary fragment sizes.

3. Disintegration of Comets - The First 10 Seconds

When a single impactor penetrates the Jovian atmosphere, the object compresses the ambient gas and a bow shock forms in front of the object. The object is also compressed, deformed, and ablated via Kelvin - Helmholtz and Rayleigh - Taylor instabilities as a result of the hydrodynamic stresses imposed by the atmosphere and the heat transfer from the shocked gas. In this section, the entry phase of the impact is studied to investigate the mechanics of cometary mass loss, via hydrodynamic instabilities, interaction of the cometary materials with the atmosphere, the disintegration of the comet, and subsequent mass and energy deposition profiles.

3.1 Model description

The SPH method describes the motion of materials by the use of a finite number of particles. The accuracy of the calculation depends on the number of particles of a comet and the atmosphere involved in a calculation. For the entry studies, Jovian atmospheric space is segmented into successive overlapping target boxes, each of which contains a total of 51840 particles stacked 45 × 36 horizontally and 32 vertically (figure 1(a)), and the successive calculation for each target box is performed.

This configuration was employed because of the resource limitation on the number of particles used in a calculation and the minimum number of particles representing the cometary fragment required for obtaining a desired accuracy. The dimension of each target box is approximately 20 km for a 2-km impactor and 80 km for a 10-km impactor. As a comet passed through the atmosphere, we employ successive calculations in each atmospheric box, until the cometary particles are dispersed and stopped. Successive calculations within 37 and 17 target boxes are performed for the 2 and 10 km diameter cometary fragments. The number of cometary particles (280) is chosen from the minimum number that can reproduce results of Eulerian code [O'Keefe and Ahrens, 1977], for a spherical comet.

The two kinds of particles, Jovian atmosphere and H_2O, interact with similar and different particles in the same way as the materials of single composition except for the different thermal properties - equation of state. The mass of each cometary particle is constant, whereas the mass of atmospheric particles varies as a function of altitude to simulate the Jovian atmospheric structure. The 2-km comet is placed initially at an altitude of $\sim$ 50 km (100-mbar pressure level), and the calculation for 10-km impactor starts at 0 km (1-bar pressure level). Above these altitudes, the energy loss of the impactor is negligible.

3.2 Mechanics of distortion of cometary body

Figure 1 shows the time history of (a) the internal energy and (b) velocity during entry into Jovian atmosphere of a 2-km diameter cometary fragment. We approximate the temperature profile by assuming the constant specific heat of $C_V \sim 1.5 \times 10^8$ erg/g·K for molecular hydrogen (the specific heat of H_2O is one order smaller than this value) is also superimposed in the legend of figure 1 (a). Only atmospheric particles on the center-plane and all the cometary particles are shown in figure 1.

As the comet penetrates the atmosphere, the gas is accelerated radially away

(a)

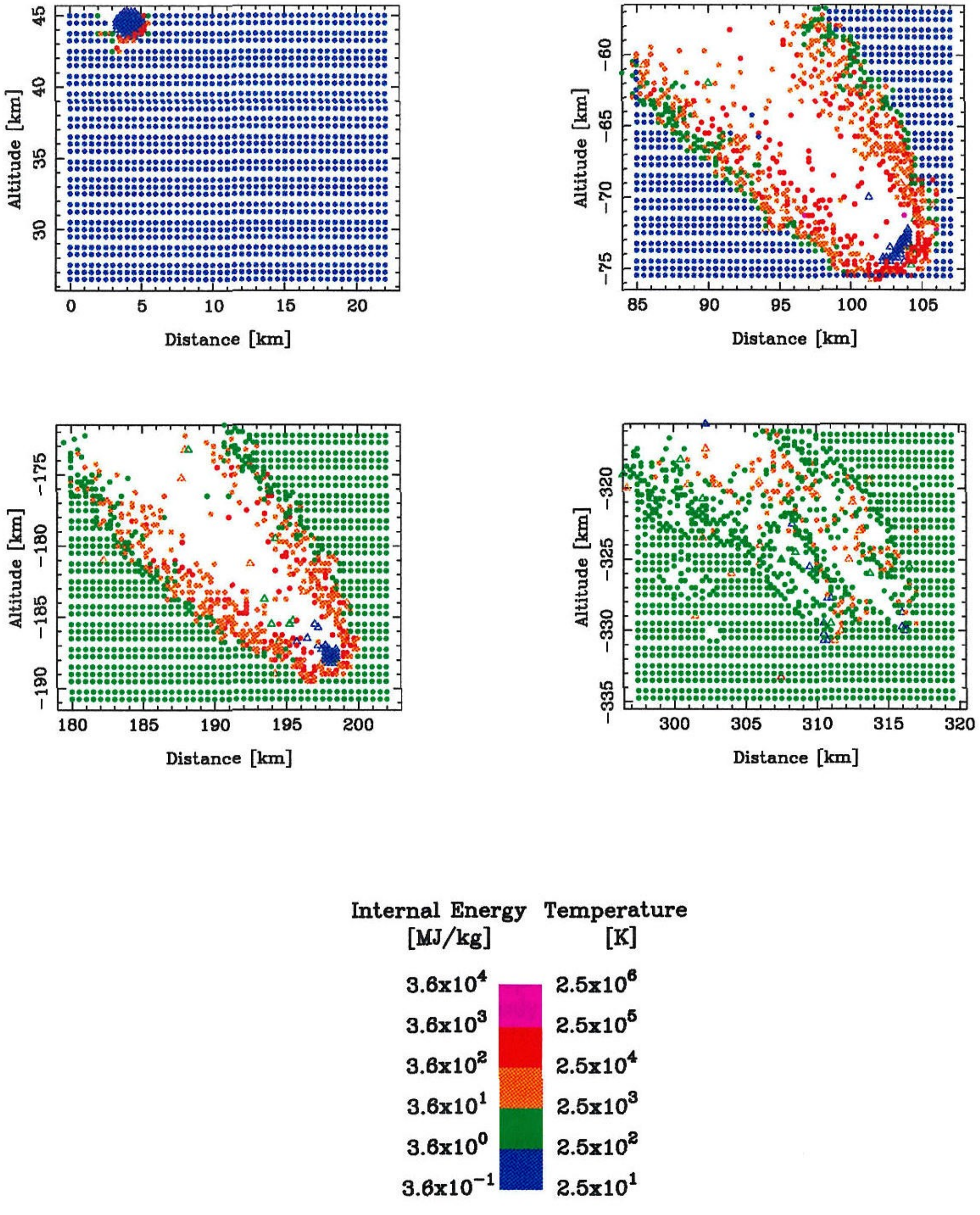
Altitude [km]
45
40
35
30
0
5
10
15
20
Distance [km]
Altitude [km]
-60
-65
-70
-75
85
90
95
100
105
Distance [km]
Altitude [km]
-175
-180
-185
-190
180
185
190
195
200
Distance [km]
Altitude [km]
-320
-325
-330
-335
300
305
310
315
320
Distance [km]
Internal Energy [MJ/kg]
Temperature [K]
3.6×10^4
3.6×10^3
3.6×10^2
3.6×10^1
3.6×10^0
3.6×10^{-1}
2.5×10^6
2.5×10^5
2.5×10^4
2.5×10^3
2.5×10^2
2.5×10^1

(b)

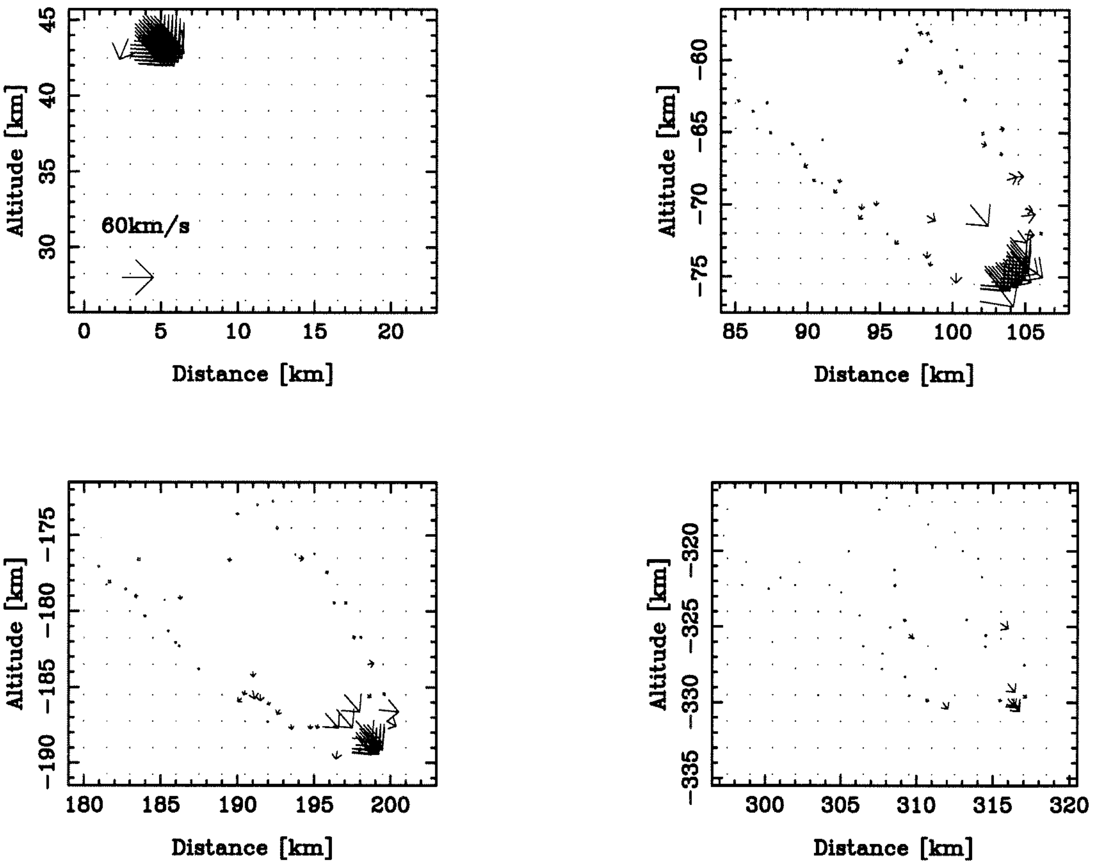

Figure 1. SPH calculations for the entry of a 2 km cometary fragment into the Jovian atmosphere. (a) The internal energy and temperature field at t = 0. s, t = 2.6 s, t = 5.5 s, and t = 11 s. Triangles and circles represent the cometary particles and the atmospheric particles, respectively. (b) The velocity vectors of particles at the same time steps as (a). Both show the atmospheric particles only on the center plane and all the cometary particles. t = 0. s represents the starting of the simulation; t = 2.6 s, deformation of the cometary body; t = 5.5 s, incipient disintegration of the comet; and t = 11.1 s, complete disintegration and deceleration of the comet.

from the normal to the trajectory, producing a cylindrical blast wave. At 2.6 seconds, when the comet penetrates to -75 km ($\sim$ 7-bar pressure level), the shocked gas pressure and the temperature within the bow shock in front of the comet reaches more than 10 kbar and 10^4 K, respectively. The heated atmospheric gas is left behind the impactor in a low-density and high-temperature wake. At this stage, the dynamic pressure causes significant flattening of the body and hydrodynamic instabilities form concurrently [Ivanov, 1988, Ivanov et al. 1992, O'Keefe et al. 1994]. The velocity and density differences between the melted/vaporized layer on the cometary surface and compressed atmospheric gas flow along its sides of the cometary surface result in Kelvin - Helmholtz instabilities on the cometary surface. These instabilities are produced in front near the centerline and also causes the ejection of cometary fragments into the gas flow [O'Keefe et al., 1994]. Rayleigh - Taylor instabilities also grow at the cometary surface and eject cometary materials into the atmospheric gas [O'Keefe et al. 1994, Ivanov, 1988].

The lateral spreading of the comet is confined by the strong bow shock surrounding the comet, with the cross sectional area never exceeding a few times its initial value. Hydrodynamic deformation and confinement of cometary materials are observed in numerical calculations of cometary penetration into an atmosphere [Boslough et al., 1993, Crawford et al., 1994, Vickery, 1993, Ivanov et al., 1992]. Experiments in which several fragments are fired into gas with a light gas gun show that a number of fragments of an impactor can be contained in a single Mach cone as the gas pressure and the Mach number increase. Lateral spreading of fragments was not observed in small-scale experiments conducted in a dense gas environment [Schultz and Gault, 1992]. In an exponential atmosphere, the dynamic pressure acting on an impactor increases as the impactor penetrates deeper into the atmosphere. The characteristic time of lateral spreading of an impactor, t_T, is

$$t_T = D/v_T \tag{1}$$

where D is the diameter of the impactor and v_T is the lateral velocity of spreading. Here v_T is estimated as

$$v_T = V(\rho_a/\rho_c)^{0.5} \tag{2}$$

where V is the velocity of a bolide and ρ_a and ρ_c are the densities of the atmosphere and the impactor, respectively [Melosh, 1989]. On the other hand, the characteristic time of penetration, t_N, is

$$t_N = H/V \tag{3}$$

where H is the scale height of the atmosphere ($\sim$ 20 km at the altitude of 0 km). In the case of SL-9 fragments, the characteristic time of lateral spreading is a few seconds, whereas the characteristic penetration time is $\sim$ 0.5 seconds. Therefore, the comet penetrates to higher gas pressure levels much faster than the rate of lateral spreading. Because of the high Mach number of the incident impactor and its long characteristic length ($\sim$ diameter of the impactor), there is a rapid increase of dynamic pressure from the bow shock acting on the lateral surfaces of the impactor. This relatively higher pressure prevents the lateral spreading of the projectile upon mechanical break-up. Therefore, it is not possible for the cometary radius to spread out by more than a factor of $\sim$ 2 as the comet fragments penetrate in the Jovian atmosphere with hypersonic velocity.

After the maximum spreading of the cometary material occurs, the mass of the deformed cometary fragment is shedded largely from its edges via break-off from Kelvin - Helmholtz instabilities (Fig. 1a). The main body becomes conical in shape due to the instabilities acting along the edge of the comet. This is seen in figure 1 (a) at t = 5.5 seconds. Because of the high hydrodynamic pressure, the cometary fragment starts to decelerate. The deceleration of the main body of the comet starts at $\sim$ -170 km (33-bar pressure level) for D = 2 km and at $\sim$ -270 km (100-bar pressure level) for D = 10 km. The cometary materials are strongly heated and vaporized as the comet penetrates deeper into the atmosphere. All the particles are dispersed, decelerated, and vaporized by t $\simeq$ 11 seconds [Figure 1].

3.3 Energy partitioning and deposition

Energy deposition and the dispersion of cometary materials in the atmosphere as a result of SL-9 fragment impact will significantly affect the local chemistry of the atmosphere and cause rapid upwelling of gas heated by the impact. In figure 2, the energy partitioning as a function of penetration time is shown in the case of D = 2 km. Upon fragment entry, the atmosphere gradually gains energy from the kinetic energy of the impactor. Upon deceleration of the comet, some 70% of the initial impactor kinetic energy is converted into internal energy of the atmosphere, while 20% is converted to kinetic energy of the atmosphere. This energy gives rise to a growing plume (fireball).

The partitioning of energy is similar for both 2-km and 10-km impactors. It takes $\sim$ 10 seconds and $\sim$ 20 seconds, respectively, for a cometary fragment with 2 and 10 km diameter to be stopped and be completely broken-up. The average internal specific energy deposited in the cometary materials is approximately 10^{12} erg/g. This is more than the ionization energy of ice ($\sim 7 \times 10^{11}$ erg/g for H^+ and OH^-) and the temperature exceeds $\sim 2.5\times10^4$ K. The average specific energy deposited in the atmospheric gas also becomes $\sim 10^{12}$ erg/g assuming that a cylindrical volume along the trajectory, with a radius of 5 km obtains 70% of the initial kinetic energy of a 2 km diameter comet. This volume contains approximately ten times the initial impactor mass. The resulting atmospheric temperature is approximately 10^4 K assuming the specific heat of the atmosphere is 10^8 [erg/gK]. All the molecular hydrogen can be dissociated and 10% of the H_2 can be ionized by this specific energy. All other constituents, such as NH_3, CH_4, and H_2O are ionized completely upon achieving this specific energy.

In figure 3, the energy deposition in the atmosphere per unit altitude is shown by solid lines in the case of D = 2 km and D = 10 km. Here the energy deposited

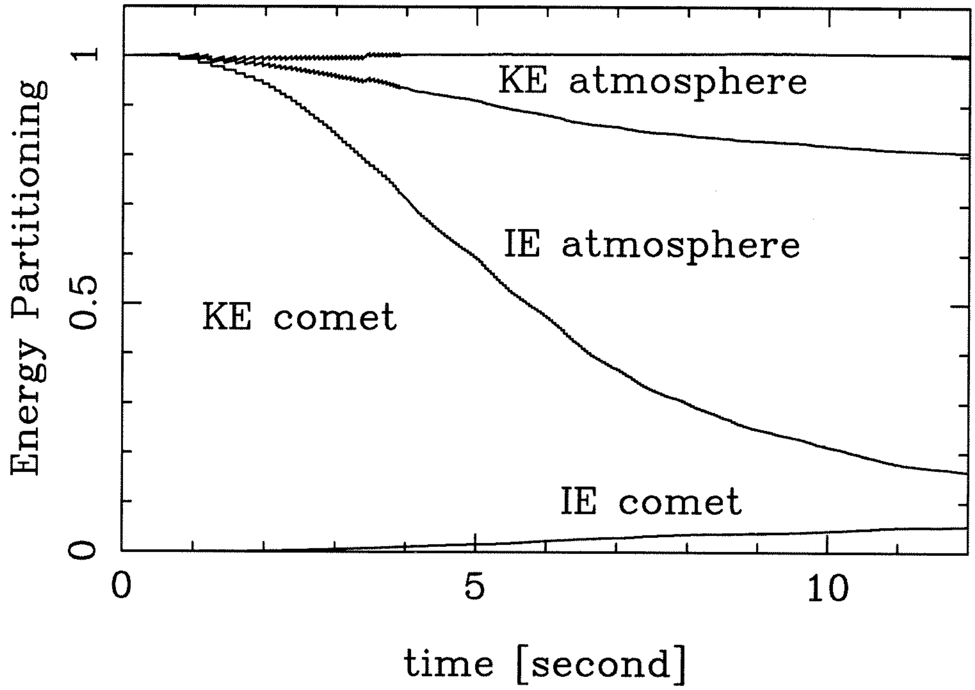

Figure 2. Energy partitioning of the 2km size impactor as a function of time. IE and KE denote internal and kinetic energy, respectively. The unit is the initial kinetic energy of the comet. The calculation was started at 50 km altitude. At 11 seconds, more than 90% of the kinetic energy of the comet fragment is transferred to the atmosphere. The release of the potential energy of a comet contributes the total final energy a little bit greater than 1.

in the disaggregated cometary materials is not included. The energy release from the comet to the atmosphere is most rapid in the -100 km to -250 km altitude range ($\sim$ 10-bar - $\sim$ 100-bar pressure level) for $D = 2$ km and -350 km to -480 km ($\sim$ 200-bar - $\sim$ 500-bar pressure level) for $D=10$ km. The fragments penetrate to an altitude of -350 km ($\sim$ 200-bar level) for $D = 2$ km, and -550 km ($\sim$ 800-bar level) for $D = 10$ km. Therefore, in both cases, cometary fragments penetrate to below the cloud decks of NH_3 ($\sim$ 0.5 bar), H_2S, NH_4SH ($\sim$ 2bar), and H_2O ($\sim$ 5 bar) [Atreya, 1986]. The

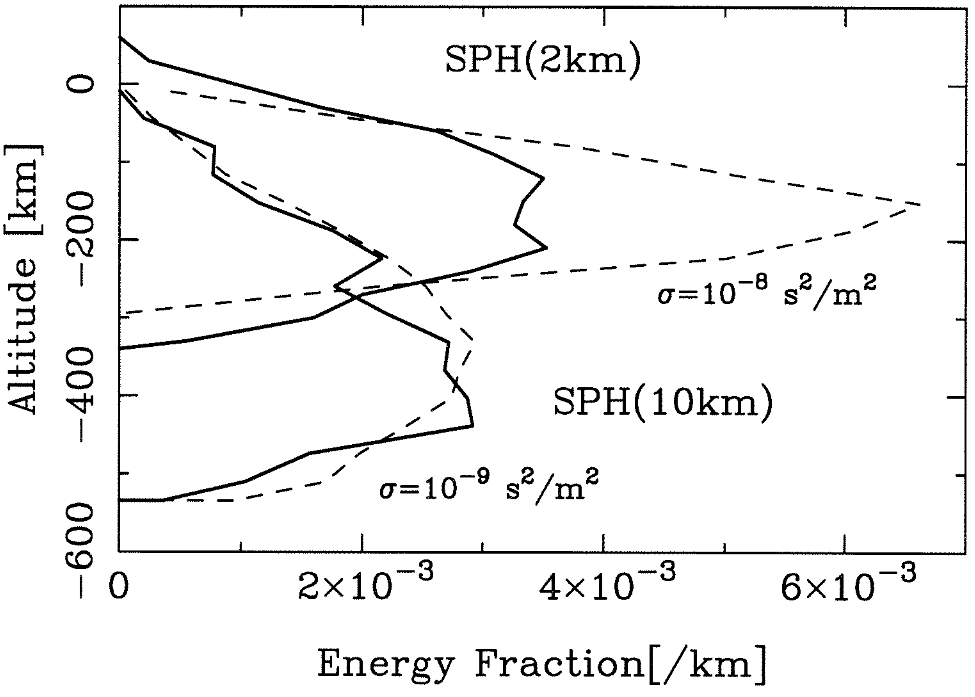

Figure 3. The fraction of the initial kinetic energy of a comet deposited in the atmosphere as a function of altitude for D = 2 km and D = 10 km. The unit of the horizontal axis is the energy fraction to the initial kinetic energy per unit altitude. The results of the SPH calculations are shown by solid lines. The energy deposit derived from the classical ablation model [Bronshten, 1983] with ablation coefficient, $\sigma = 10^{-13}$ and $\sigma = 10^{-12}$ s^2/cm^2 for D = 10 km object are shown in dashed lines. $\sigma \sim 10^{-13}$ s^2/cm^2 is the best fit to SPH result of D = 10km.

cometary materials are distributed over the cylindrical wake between -40 km and -350 km for D = 2 km, and between -150 km and -550 km for D = 10 km.

3.4 Scaling to other sizes

Since the impact resulting from only two sizes of cometary fragments has been examined, and the diameters of the 21 fragments are assumed to vary from $D \sim 10^2$ m to $D \sim 4$ km by Weaver et al. [1994], it is necessary to investigate a range of sizes.

In an exponential atmosphere, assuming that no ablation, breakup, or deformation of an impactor takes place, the pressure level of final penetration, P, is derived from the deceleration equation due to the drag force acting on the comet [Bronshten, 1983] as

$$P \propto P_0 \frac{\rho_c}{\rho_0} \frac{D}{H} \frac{\cos\theta}{C_D} \tag{4}$$

where ρ_0, P_0 are the density and pressure of the ambient atmosphere at 0 km in altitude, 0.16 kg/m^3, and 1 bar, respectively, H is the scale height, C_D is the drag coefficient, and θ is the angle of impact, measured from the zenith. In figure 4(a), the penetration pressure level for two fragment diameters of SL-9 obtained by SPH simulations are plotted with the symbol $\odot$. For other sizes, the best fit of line of the penetration-pressure level extrapolated from equation (4) and SPH results is shown by the solid line. Energy, E, is related to D via E = $\frac{1}{12}\rho_c\,\pi D^3 V^2$, where V = 60 km/s and $\rho_c = 1$ g/cm^3. Thus equation (4) provides an estimate of atmospheric penetration versus diameter. From the above scaling relation, a fragment with D = 1 km and a density of 1 g/cm^3 (ice) will have been totally stopped and ablated above the 100-bar pressure level ($\sim$ -270 km altitude). Icy fragments of D = 200 m and D = 100 m will be stopped and ablated at $\sim$ 20-bar pressure level ($\sim$ -135 km), and at $\sim$ 8-bar pressure level ($\sim$ -80 km), respectively. Therefore, most of the SL-9 fragments penetrate deeper than the visible cloud decks and most of their energy will initially be deposited at pressure levels less than 10^2 bar.

We have studied the impact of non-porous comets. If the cometary object has a certain degree of porosity, additional compressional heating will occur in the cometary body during the penetration and this will result in greater thermal energy becoming deposited in the comet at earlier stage. These effects will result in a shallower penetration depth of the impactor.

3.5 Comparison with other models

Since the time that SL-9 has been predicted to impact Jupiter [Shoemaker et al. 1993, Yeomans and Chodas, 1993], several other studies for the entry of a comet have been performed. The approaches used can be divided into two general methods. One is numerical simulation using hydrodynamic codes [this study, Crawford et al. 1994, Vickery, 1993, Moran and Tipton, 1993, Mac Low and Zahnle, 1994], and the other is the application of classical ablation models [Bronshten, 1982]; [Sekanina, 1993, Zahnle and Mac Low, 1994].

In figure 4(a), in order to compare results from all the models, the pressure levels of the final penetration are plotted. All the models except Sekanina's model agree that fragments of SL-9 larger than 1 km can penetrate deeper than the visible cloud deck. The interesting point is that the classical ablation model results in shallower penetration of a cometary body than obtained with hydrodynamic codes. The latter assume fluid rheology or low strength for the cometary materials. For example, our results indicate a comet of D = 200 m will reach the pressure level of 8 bar, whereas the classical ablation model predicts that a comet with the same mass will penetrate only to the 0.04-bar pressure level [Sekanina, 1993] or 0.8-bar pressure level [Zahnle and Mac Low 1994].

In the classical analytical model [Bronshten, 1982], the mass loss is obtained by assuming that a fraction α of the kinetic energy lost by the impactor is taken up by ablation processes. The rate of mass loss for an ablating comet is

$$\frac{dm}{dt} = -\frac{C_D}{2}\sigma S \rho_a V^3 \tag{5}$$

where S and m are the cross sectional area and mass of the impactor, respectively, and σ is the ablation constant $\sigma = \alpha/(C_D\xi)$. Here ξ is the ablation energy, which is variously assumed to correspond to melting, vaporization or even ionization. In this model, σ is based upon assumed values of α, ξ, and S. Experiments provide widely

(a)

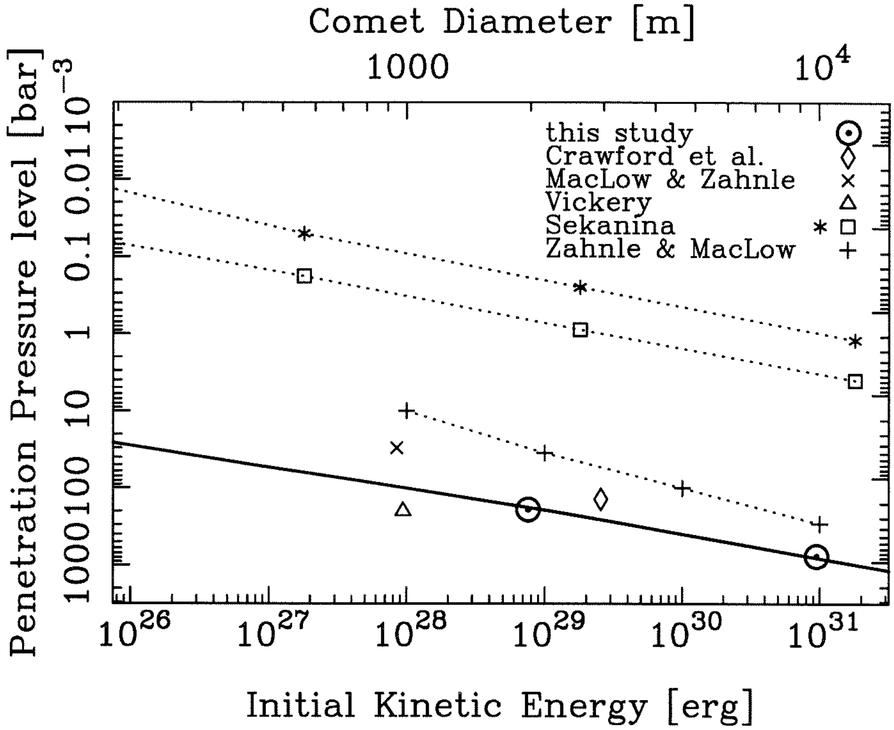

varying values of σ for different media, and hence, σ is uncertain to within 2 to 3 orders of magnitude [Bronshten, 1982]. Unfortunately, the predicted rate of ablation in the classical approach strongly depends on this highly uncertain parameter. For example, we plotted the energy deposition of the classical ablation model for $\sigma = 10^{-12}$ and $\sigma = 10^{-13}$ [s^2/cm^2] for D = 10 km with short dashed lines in figure 3 [Bronshten, 1982]. We note that a factor of 10 difference in σ yields a factor of ~5 difference in the pressure level of penetration. The present SPH results can fit with values of $\alpha \simeq 0.1$, $\xi \simeq 10^{12}$erg/g, and $\sigma \simeq 10^{-13}$ [s^2/cm^2]. Sekanina [1994] assumed spherically isotropic ablation (asterisks in Fig. 4a) and front surface ablation of a cylindrical impactor (squares in Fig. 4a) to define the cross sectional area. In his model, σ is assumed 2×10^{-11} [s^2/cm^2]. These assumptions result in a higher final altitude of penetration than obtained with the hydrodynamic codes. The model of Zahnle and

(b)

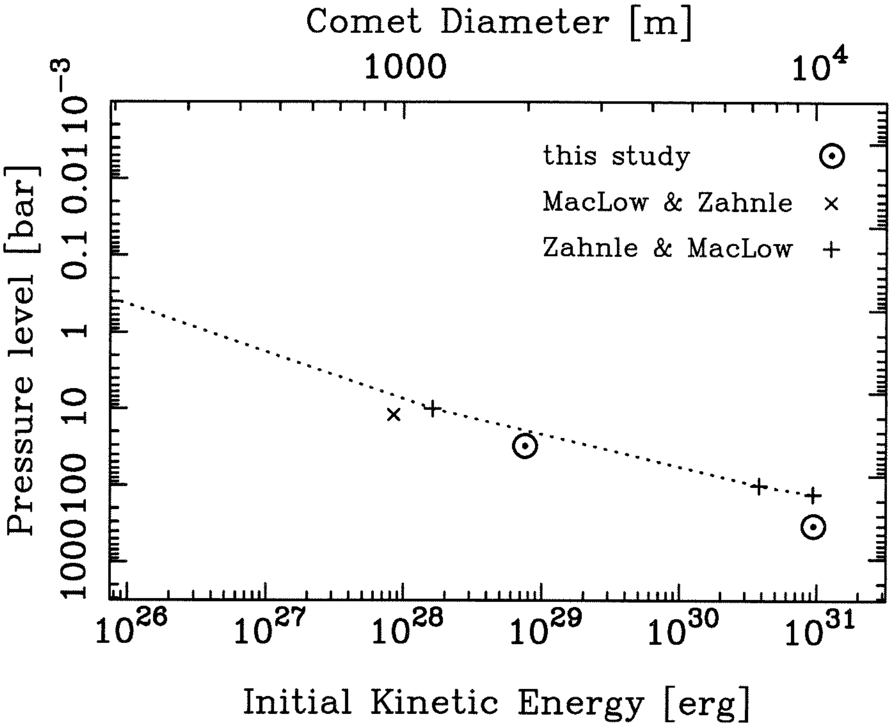

Figure 4. The penetration depth of a comet fragment as a function of initial kinetic energy for various models. The size is estimated from the initial kinetic energy assuming that the density of the comet is 1 g/cm^3 and impact velocity is 60 km/s. ⊙ represents SPH results for D = 2km and D = 10 km. The solid lines represent the scaled penetration depth extrapolated from SPH results. ◇ : Crawford et al. [1994]; △ : Vickery [1993]; × : Mac Low and Zahnle [1994]; $\cdots+\cdots$: Zahnle and Mac Low [1994]; $\cdots*\cdots$ and $\cdots\square\cdots$: rigid spherical body and cylindrical body of Sekanina [1993]. Crawford et al. [1994], Vickery [1993], Mac Low and Zahnle [1994] are numerical studies, whereas Zahnle and Mac Low [1994] and Sekanina [1993] are based on the classical ablation model [Bronshten, 1983]. (b) The pressure level of maximum energy deposition as a function of initial kinetic energy of impactor. All the data available from the studies of (a) are shown. The symbols are the same as (a).

Mac Low [1994] includes a break-up criterion in the classical ablation model. This provides a wider lateral cross sectional area, S. The cross sectional area increases exponentially with time as the comet penetrates the exponential atmosphere [Chyba et al., 1992]. Although their assumed ablation coefficient, $\sigma > 10^{-12}$ [s^2/cm^2], is lower than Sekanina's assumed value, their calculation still predicts higher termination altitude than results of hydrodynamic codes.

The results of Crawford et al. [1994] obtained with the 2D axisymmetric calculations of CTH code (2D/3D Eulerian code) is shown with the symbol of $\Diamond$ in figure 4 (a). The CSQ code used by Vickery [1993], which is 2D version of CTH code, also utilizes the ANEOS equation of state to describe cometary ice. ANEOS includes the effects of ionization and dissociation of the materials. In her calculation, Vickery obtained deeper penetration than the other models. Mac Low and Zahnle [1994] use a 2D axisymmetric code, ZEUS, with the gas equation of state for the impactor. A gas equation of state, such as used in Mac Low and Zahnle [1994], lacks a cohesive property, which tends to achieve plausible cometary densities, with the initial internal pressure of the gaseous comet $> 10^2$ bar. The flow around the comet results in a low pressure region behind the comet. The high pressure gradient between the trailing impactor surface and the atmospheric wake induces deformation at the trailing edge of the projectile. As a result, the expansion of gaseous comet occurs in addition to deformation along the leading surface of the projectile produced by instabilities. The resulting deformation of the gaseous comet leads to a toroidal shape. As a result, mass loss occurs from both the leading and trailing edges of the comet.

Mac Low and Zahnle [1994] suggested that more than 25 zones in radius are required to properly resolve the dynamical instabilities acting on an impactor in the case of two-dimensional axisymmetric simulation; otherwise, lower resolution of physical instability results in the deeper penetration of the comet. However, it is not certain, that it is important to resolve short wavelengths of Kelvin-Helmholtz instabilities for the present application, because analytical study of O'Keefe et al. [1994] demonstrated that the most effective wavelengths of Kelvin-Helmholtz instabilities, for the mass loss, is on the order of the size of the impactor, and the mass loss by small wavelengths will result in shedding only small amounts of mass. Moreover, it is not clear why the calculation of Mac Low and Zahnle [1994] resulted in slightly shallower penetration into Jupiter's atmosphere than the other models, for example, Vickery [1993] obtained much deeper penetration depths with more realistic equation of state with more than 25 radial zones. Therefore, the reason why Mac Low and Zahnle [1994] require more than 25 radial zones in the impactor is unclear, and the zoning problem will require more study.

Figure 4 (b) shows the pressure level of maximum energy deposit for the models where quantitative data are available. The depth of maximum energy release of the three calculations are actually quite similar.

3.6 Cylindrical expansion at 10 seconds

A simple model of the atmospheric wake from the impactor is a paraboloidal bow shock, in which low density and high pressure and temperature are achieved. The wake is 350 km below the cloud deck for D =2 km and 550 km deep for D = 10 km. From the self-similar solution for a cylindrical expansion [Zel'dovich and Raizer, 1967], and the assumption of paraboloidal bow shock geometry, the wake radius at Z_0 is $\sim (V\Delta t D)^{0.5}$; here Δt is the time after the comet passes through Z_0 [Takata et al. 1994]. We calculate that wake has a radius of ~ 30 km in the case of 2 km diameter cometary fragment, and ~ 110 km radius in the case of 10 km diameter cometary fragment at the 1-bar level by the time the fragment is completely disintegrated. Assuming that the shock-heated gas radiates as a black body at the cloud tops at $T \sim 10^4$ K, then the radiating power at 10^1 seconds after the impact is $\sim 10^{25}$ erg/s for the impact of a body with D = 2 km and $\sim 10^{26}$ erg/s for D = 10 km. The total radiated energies are still $\ll 1\%$ of the initial kinetic energy for both cometary sizes. However, the average radiant flux of Jupiter is $\sim 15 \times 10^3$ [erg/s cm^2], so the intense radiation from the shocked gas is approximately a factor of 10^7 to 10^8 greater than the flux from the ambient atmosphere. During and immediately after the entry of the cometary fragments, the resulting energy deposited in the atmosphere is explosively released in the upward expansion of this plume. In the following section, we investigate this process.

4. Evolution of the Explosive Plume - The Next 10^2 Seconds

Once the initial kinetic energy of a fragment of SL-9 is deposited in an atmospheric cylinder along its entrance trajectory in $\sim$ 10 seconds, the high-pressure heated gas inside the wake result in an atmospheric shock wave. Later, a fireball-like plume forms which is similar to that from an atmospheric nuclear explosion. In order to investigate the evolution of the plume expansion, we carried out the second SPH calculation using the energy deposition obtained in the first calculation described in the previous section.

4.1 Approach

For impact by a 2-km body, we distributed approximately a quarter million atmospheric particles representing a parcel of the Jovian atmosphere with dimensions 10^3 km long $\times$ 800 km wide, over an altitude interval from 350 km to -400 km [figure 5]. For 400-m and 10-km impactor, similar atmospheric boxes are constructed with $\sim 10^5$ atmospheric particles. However, the atmospheric parcel size varies with the magnitude of the energy deposited ($\sim$ 350 km wide for D = 400 m impact and $\sim$ 1000 km wide for D = 10 km impact). The mass and internal energy of each particle is initially set to match the Jovian atmosphere. The energy deposited by passage of a cometary fragment obtained by the SPH calculation discussed in the previous section [figure 3] is then placed in atmospheric particles in the cylindrical wake along the trajectory for both the D = 2 and D = 10 km cases [e.g., figure 5, t = 0 s]. For the D = 400 m impact, the results of classical ablation model with $\sigma = 10^{-13}$ s^2/cm^2, which is the best fit to SPH result, are applied to obtain the initial distribution of the impact energy.

The average specific energy along the trajectory is $\sim 10^{12}$ erg/g. The horizontal dimensions of these cylinders are approximately 8 km for D = 400 m, 13 km for D = 2 km, and 25 km for D = 10 km. The cylinders extend from altitudes of 50 km to -100 km for D = 400 m, from 50 km to -350 km for D = 2 km, and from 0 km to -550 km for D = 10 km at altitude. Initially, the velocities of particles are assumed to be zero and the atmospheric shock wave and the resulting plume are allowed to evolve. Calculations are carried out until the shock wave reaches the edge of the atmospheric box after approximately 10^2 seconds.

4.2 Plume development

Figure 5 shows the evolution of the plume as a function of time for the impact of a 2-km fragment. At t = 11 seconds, which is approximately equal to the time interval required for the cometary energy dissipation upon impact as measured from the time when the comet through the 1-bar level. The atmospheric gas starts to expand cylindrically along the fragment trajectory as a result of isentropic expansion of the shocked gas. The radius of the expanding shock wave at the 1-bar level is $\sim$ 30 km, in agreement with the analytical solution discussed in the previous section. In the 40° inclined cylindrical wake, the apparent atmospheric temperature is as high as $\sim 10^4$K, and the gas starts to move backward toward the entry direction of the impactor. The temperature in the legend of figure 5 is derived assuming the constant specific heat of $C_V \sim 1.5 \times 10^8$ erg/g·K, similar to figure 1.

As the comet penetrates the atmosphere, the gas is accelerated radially away from the normal to the trajectory, producing a cylindrical blast wave. At 2.6 seconds, when the comet penetrates to -75 km ($\sim$ 7-bar pressure level), the shocked gas pressure and the temperature within the bow shock in front of the comet reaches more than 10 kbar and 10^4 K, respectively. The heated atmospheric gas is left behind

(a)

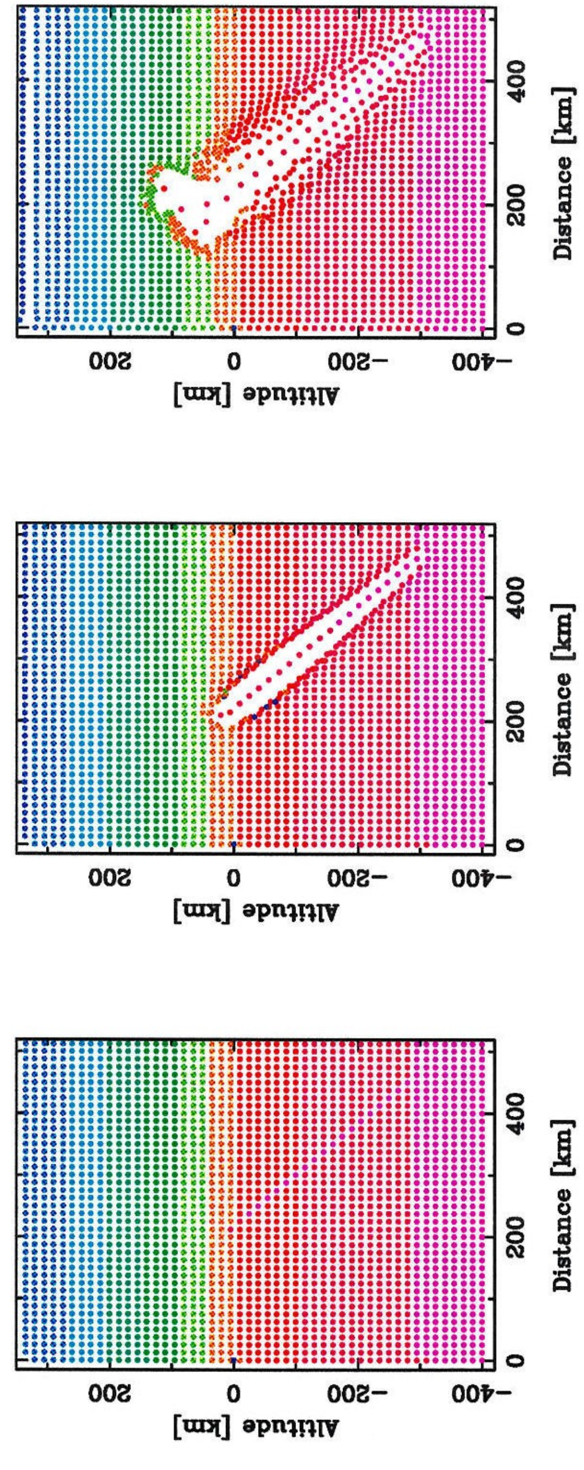
Altitude [km]
200
0
−200
−400
Distance [km]
0
200
400
Altitude [km]
200
0
−200
−400
Distance [km]
0
200
400
Altitude [km]
200
0
−200
−400
Distance [km]
0
200
400

(a)-continued

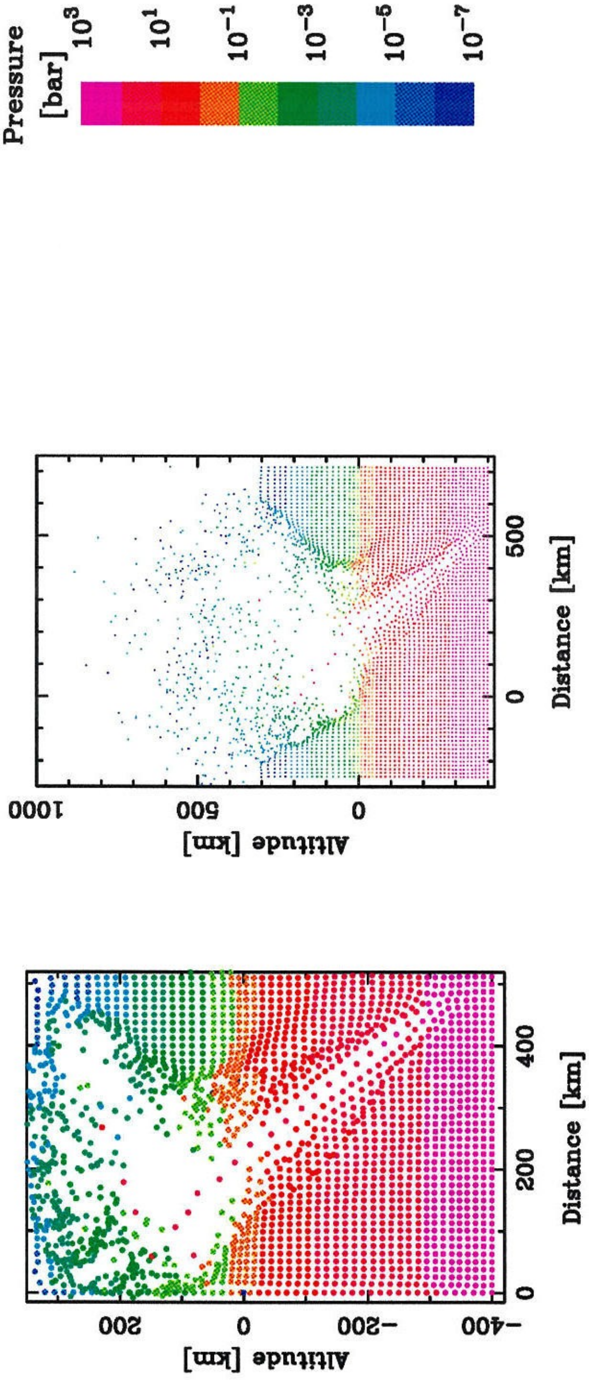
Pressure
[bar]
10^3
10^1
10^{-1}
10^{-3}
10^{-5}
10^{-7}
Altitude [km]
1000
500
0
Distance [km]
0
500
Altitude [km]
200
0
−200
−400
Distance [km]
0
200
400

(b)

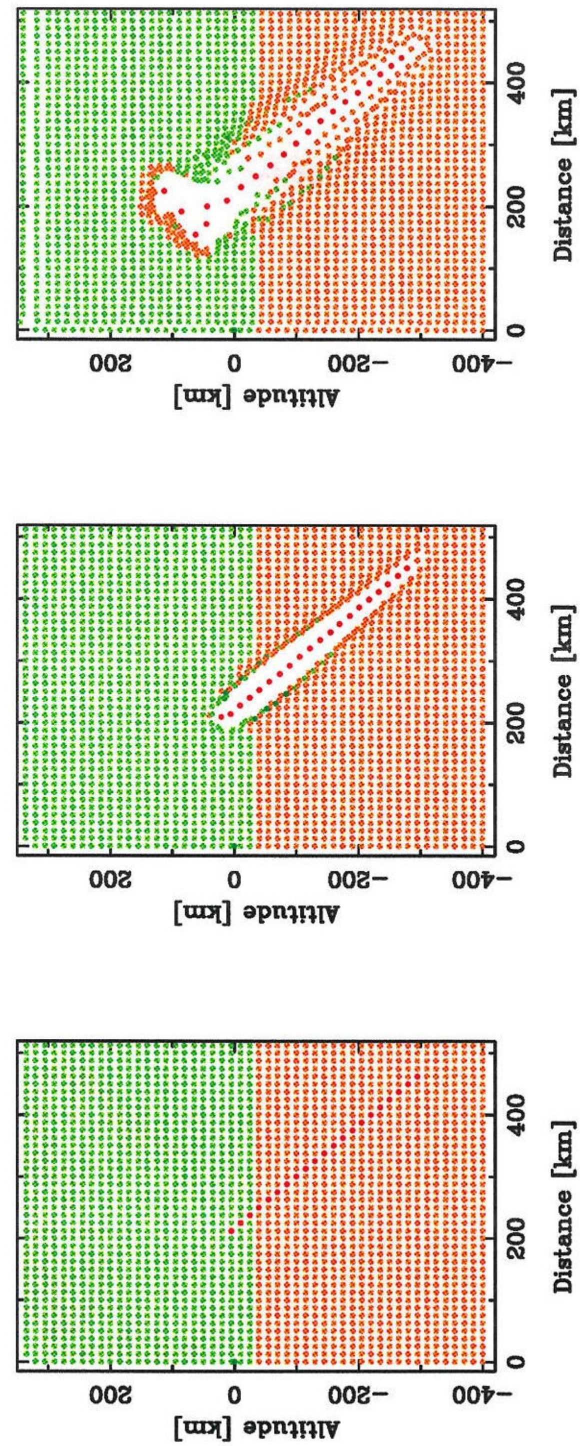
Altitude [km]
200
0
−200
−400
Distance [km]
0
200
400
Altitude [km]
200
0
−200
−400
Distance [km]
0
200
400
Altitude [km]
200
0
−200
−400
Distance [km]
0
200
400

(b)-continued

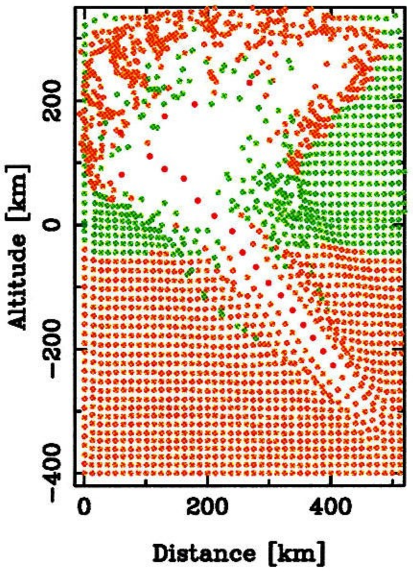
Altitude [km]
200
0
−200
−400
Distance [km]
0
200
400

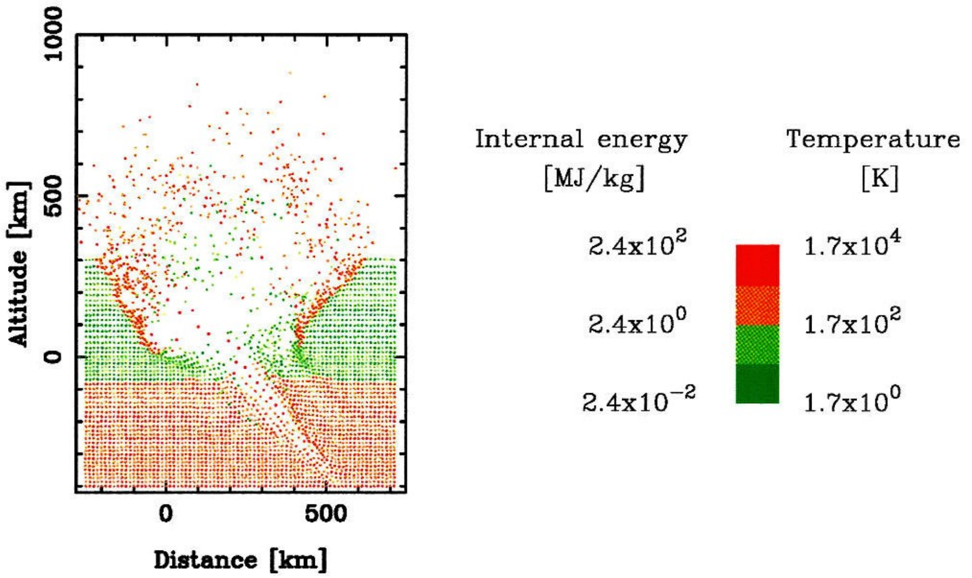
Altitude [km]
1000
500
0
Distance [km]
0
500
Internal energy
[MJ/kg]
2.4x10^2
2.4x10^0
2.4x10^{-2}
Temperature
[K]
1.7x10^4
1.7x10^2
1.7x10^0

(c)

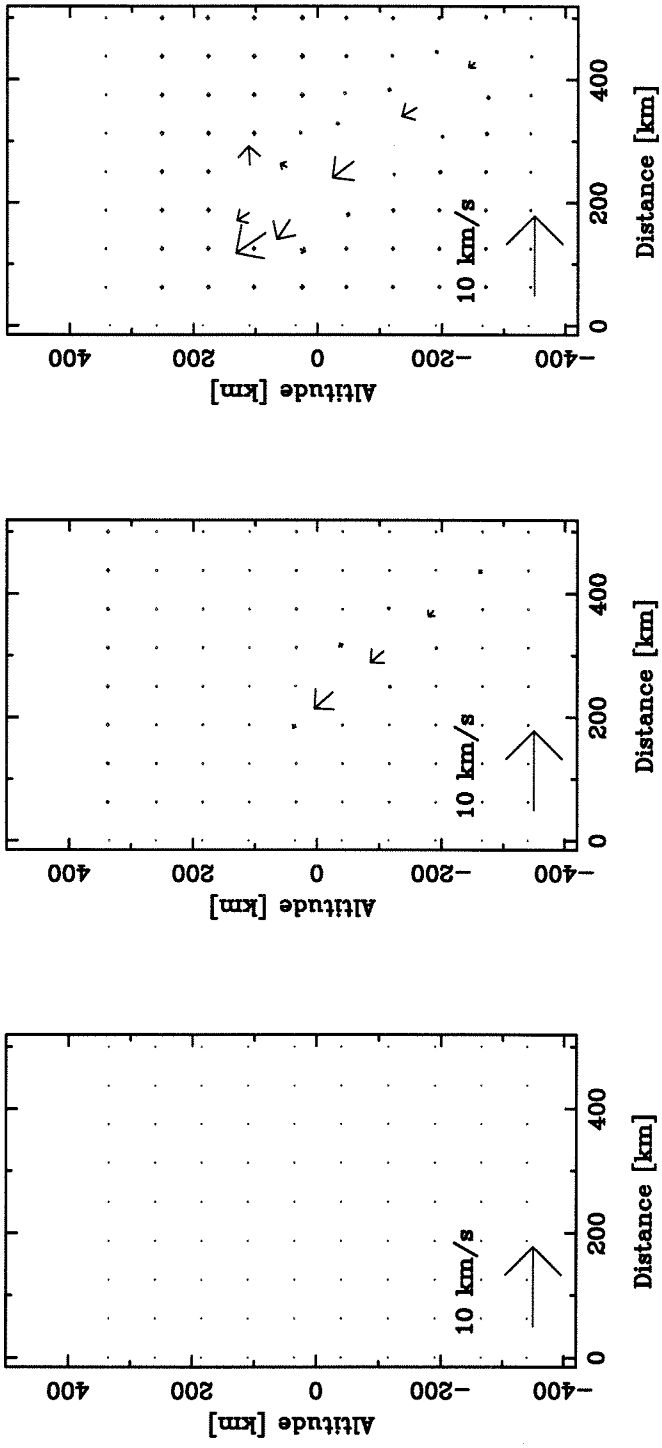
Altitude [km]
400
200
0
−200
−400
Distance [km]
0
200
400
10 km/s
Altitude [km]
400
200
0
−200
−400
Distance [km]
0
200
400
10 km/s
Altitude [km]
400
200
0
−200
−400
Distance [km]
0
200
400
10 km/s

(c)-continued

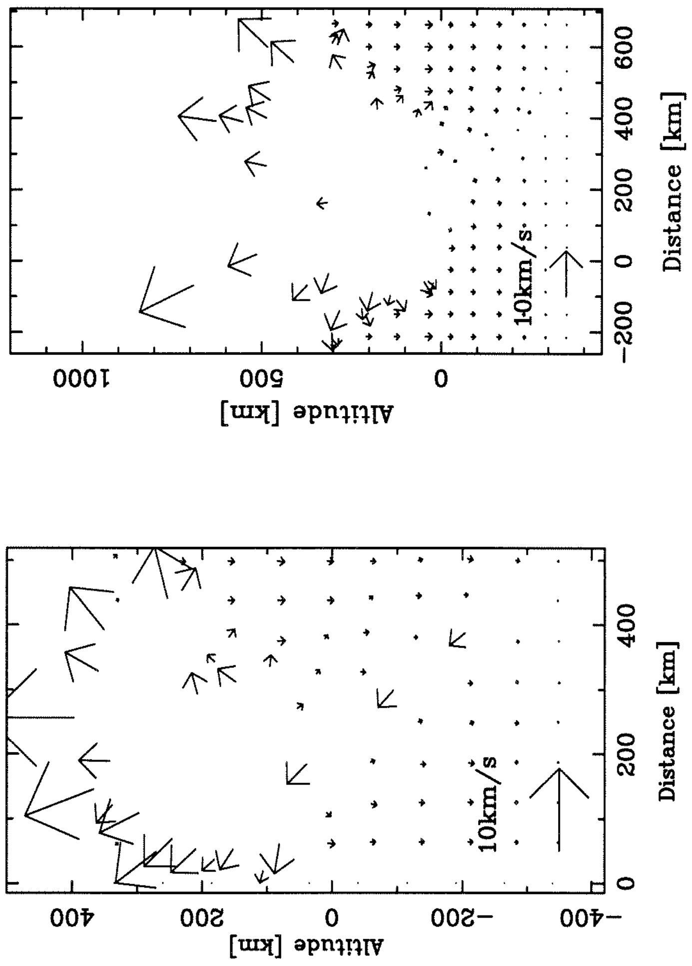

Figure 5. SPH calculations for plume evolution for D = 2 km. (a) Internal energy and the corresponding atmospheric temperature assuming $C_V = 10^8$ erg/g·K at t= 0 s, t = 11 s, t = 39 s, t = 83 s, and t=123 s. All particles are atmospheric particles. (b) Pressure field at same time as (a). (c) The velocity vectors of atmospheric particles at the same time steps of (a) and (b). t = 0 s represents the initial state of the calculation; t = 11 s, cylindrical expansion similar to the final stage of the comet-entry problem; t = 39 s, the incipient upward expansion of plume; t = 82 s, unconfined expansion of the plume; t = 123 s, growing plume and ejection of atmospheric gas.

the impactor in a low-density and high-temperature wake. At this stage, the dynamic pressure causes significant flattening of the body and hydrodynamic instabilities form concurrently.

At t = 39 seconds, the shock wave is still expanding cylindrically outward from the entry trajectory. However, the most significant phenomenon is the upward expansion of the plume. The atmospheric gas accelerates as it rises. In an exponential atmosphere, the plume grows faster vertically than horizontally. At this stage, the plume rises at a speed of $\sim$ 5 km/s and the plume-top reaches approximately 150 km altitude ($\sim$ 1 mbar pressure level). At $\sim$ 100 km ($\sim$ 8 mbar pressure level), the pressure of the expanding plume-head is a factor of 10^2 - 10^3 greater than the ambient atmospheric pressure at the same altitude. Kompaneets' solution [Zel'dovich and Raizer, 1967] shows that, if the pressure at the shock wave is more than 10^2 times the ambient atmospheric pressure at $\sim$ 1 atmospheric scale height above the explosion point, the explosive fireball is unconfined. If gravitational potential energy is neglected, the expanding plume will continue to accelerate to infinite velocity and expand up to infinite altitude. However, Kompaneets' solution do not take into account the gravitational potential energy. Therefore, explosive plumes caused by the impacts of 2-km size-fragments will be accelerated until all the energy is converted to the gravitational energy. In order to investigate the effect of buoyancy force on upward propagation of the plume, the same simulation was performed without gravity. As a result, the dominant dynamical mechanism inducing upward motion is the unconfined explosion resulting from pressure gradient in the atmosphere, and not buoyancy. Shock-heating of the atmospheric gas gives rise to an increase in the temperature of the plume head of $> 10^3$ K, and inside of the plume stalk, the temperature is still $\sim 10^4$ K.

At t= 82 seconds, the expanding fireball accelerates upward and the expansion velocity reaches ~10 km/s at the shock front. Because of the expansion of the highly pressurized gas into a near vacuum, the plume easily reaches an altitude of ~ 350 km (~ 1-μbar pressure level), i.e., > 15 scale heights above the one-bar level where the plume originates. Now a mushroom cloud-like plume develops more symmetric radial expansion. The expanding plume radius is approximately 250 km at this stage. The shock temperature of plume head is $\geq 10^3$ K. The temperature is still $\sim 10^4$ K inside of the fireball, since shock-heated gas with high internal energy is continuously funneled upward from deeper within the cometary trajectory to the base of the fireball - plume. The pressure at the shock front is still 10^2 times the ambient pressure at the same altitude, so the plume will continue to rise, until all the kinetic energy and internal heat is transformed into gravitational potential energy or is radiated to space.

At t = 123 s, some atmospheric particles reaches $\sim 10^3$ km, and the plume is still growing toward the upward.

In the case of the impact of a 10-km body, the same qualitative phenomena are observed. However, the energy source is $\sim 10^2$ greater than the case of D = 2 km, so that the scale length of the atmosphere affected is several times greater than the case of D = 2km.

The impact energy of D = 400 m is 2 order of magnitude smaller than the case of D = 2km. Although lateral expansion of shock wave resulting from the entry - wake is dominant, the upward plume can be observed. At 10^2 seconds, the lateral radial size of the shock expansion is $\sim 10^2$ km, and plume reaches 250 km at altitude. The temperature of the plume is ~ 500 K, which provides lower thermal contrast with the ambient atmosphere than the impact of a 2-km fragment, but still 3 factors larger than the ambient atmospheric temperature.

Two-dimensional fireball calculations were also conducted by Zahnle and Mac Low [1994] using the ZEUS 2D axisymmetric code. Their simulations assume an explosive energy source one order of magnitude less in energy than in the present simulation. Hence their fireball rose to altitudes of $\sim 200 - 10^3$ km depending on assumptions of energy source distributions.

4.3 Mass and energy transport

The simulations of plume evolution [figure 5] indicate that the rising plume induces the transport of the atmospheric gas from the troposphere to the upper stratosphere. Figure 6 (a) shows the excess atmospheric mass normalized by the initial cometary mass ($\sim 4 \times 10^{15}$ g) per unit altitude for the 2-km comet impact. Profiles of excess mass at four selected times are shown. The upward transport of the atmospheric mass by the plume can be seen. The vertical mass transport is not significant in the first 60 seconds, but atmospheric gas originating deeper than $\sim$ -150 km ($\sim$ 25-bar pressure level) is gradually transported to above that pressure level due to the plume expansion. The plume brings approximately 10^5 Mtons of atmosphere ($\sim$ 30 times the initial impactor mass) to above the 1-bar level for D =2 km in 10^2 seconds. At $\sim$ 200 seconds, most of the gas in the cylindrical wake can rise above the 1-bar level, and the total mass ejected to above 1-bar pressure level becomes ≥ 40 times the initial mass of the impactor.

Violent atmospheric convection results in vertical mixing of atmospheric constituents. In the bolide wake, the atmospheric gas has an average specific energy of $\sim 10^{12}$ erg/g (T $\sim 10^4$ K). Therefore, the molecular decompression products of vaporized constituents, such as H_2O, H_2S, NH_4SH, and NH_3, will be observable above their cloud decks. Moreover the shock drives reactions involving NH_3, H_2O, and NH_4SH as well as dissociation and ionization. Due to the resulting plume evolution, these constituents, their reacted products, and dissociation or ionization products will be observable above 1-bar to $\sim$ 1-μbar pressure level. PH_3 and N_2H_4 also exist below the 100-mbar pressure level and CH_4 is the most abundant minor species below 300

(a)

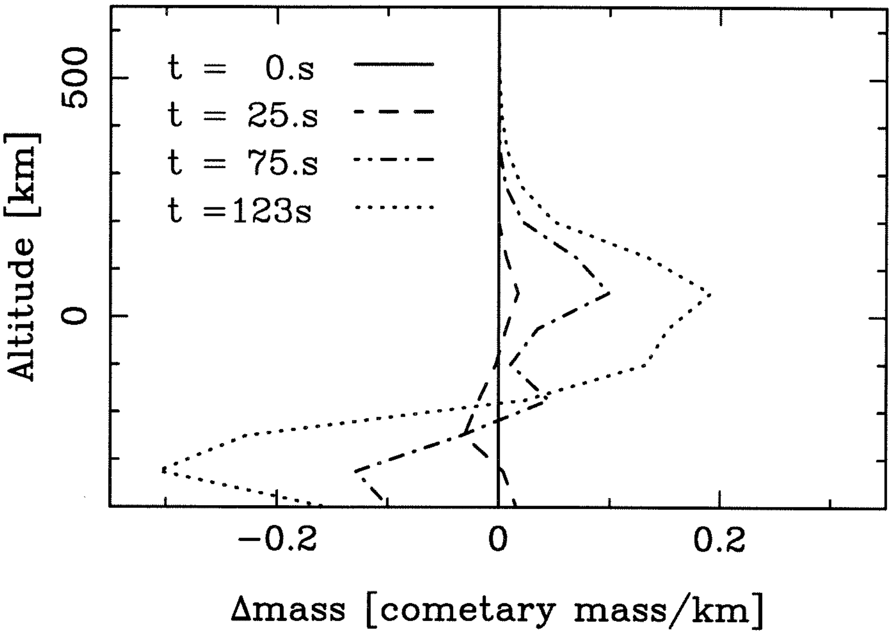
t = 0.s
t = 25.s
t = 75.s
t =123s
Altitude [km]
500
0
−0.2
0
0.2
Δmass [cometary mass/km]

(b)

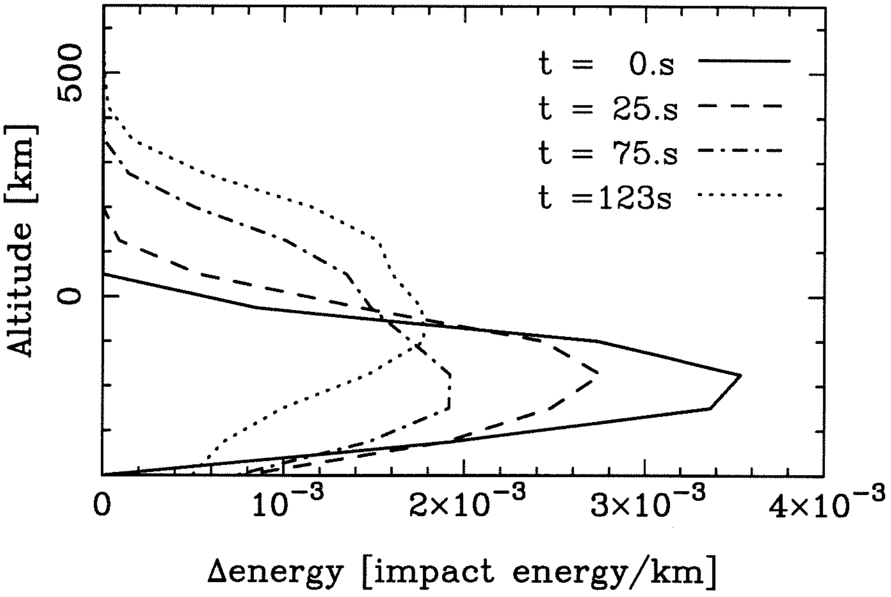
t = 0.s
t = 25.s
t = 75.s
t =123s
Altitude [km]
500
0
0
10^{-3}
2×10^{-3}
3×10^{-3}
4×10^{-3}
Δenergy [impact energy/km]

(c)

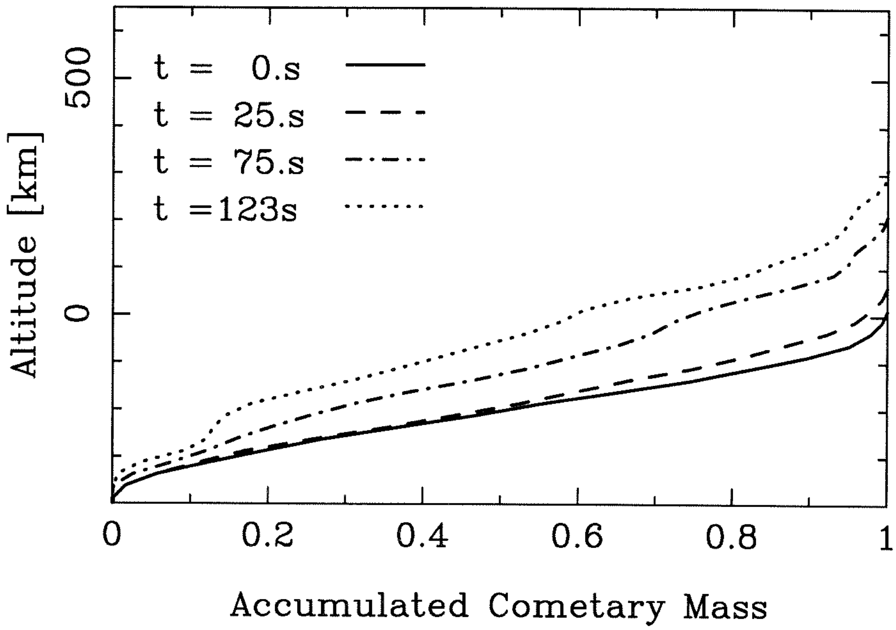

Figure 6. Mass and energy budgets versus altitude and time associated with plume evolution from 2 km diameter cometary impactor. (a) Excess and deficient of the mass of Jovian atmosphere normalized by the cometary mass (~ 4×10^{15} g) per unit altitude associated with the plume expansion at various times. (b) Excess energy of the Jovian atmosphere, normalized by impact energy (~ 7×10^{28} erg) per unit altitude at various time. (c) Accumulated fractional distribution of cometary mass along the altitude at various times.

km (10 μbar pressure) [Atreya, 1986]. These species will also be observable from their unique emission and reflectance spectra as the plume achieves high altitudes. In the center of the fireball, the density and the pressure are greatly decreased by the expansion of the plume, but the temperature is still $> 10^3$ K. The ratio of CH_4 to CO or HCN in the ambient atmosphere is 10^6 in the Jovian stratosphere. However, after shock heating and adiabatic cooling, if the C-N-O-H system achieves equilibrium, CO and N_2 from CH_4 and NH_3 are produced, and if disequilibrium reactions are dominant, HCN will be produced [Prinn and Fegley, 1989]. Therefore, a significant increase of CO and HCN will also be observable above the stratosphere.

Figure 6 (b) shows the distribution (normalized by impactor energy ~ 7×10^{28}

erg) of energy deposited per unit altitude corresponding to figure 6 (a). From figure 6(b), we find that some 20% of the initial kinetic energy of an impacting fragment is transported above $\sim$ 130 km ($\sim$ 1-mbar pressure level) and $\sim$ 40% of the initial kinetic energy of the impact reaches above 1-bar pressure level in 10^2 seconds. At 10^2 seconds, most of the energy deposited between 250 km and 350 km is the kinetic energy of the gas, whereas most of the energy deposited between 0 to 250 km corresponds to the internal energy of the atmosphere inside of the plume. The plume will transport most of the energy deposited in the deeper atmosphere to above 1-bar pressure level in $< 10^3$ seconds.

Although cometary materials are not included in the second SPH calculation, since most of them are vaporized during the entry of fragments, they will also ascend with the rapid upward gas flow. By tracing the atmospheric particles retaining the initial kinetic energy of the comet in the plume calculation and assuming that the distribution of the initial cometary mass is proportional to the distribution of the initial energy deposited at each altitude [figure 3], the distribution of cometary mass as a function of time and altitude is estimated for D = 2km impact (figure 6(c)). Gradual upward ejection of cometary mass is observed and > 40% of cometary materials rises above 0 km at 10^2 seconds, and > 80 % will ascend above the cloud decks. Once cometary materials are distributed in the upper atmosphere, they will condense at later times, and be a source of dust in the upper atmosphere. If the 2-km comet is spread out over an area of radius 10^3 km, a 1-μm thick dust layer is formed; such a layer is expected to significantly affect the optical depth in the latitude band where the impact site is located [Ingersoll, 1993; Stevenson, 1993].

5. Discussion - Later Effects on Jupiter and Observational Possibilities

Further investigation of the evolution of the expanding plume in the calculations using SPH hydrodynamics code without including a radiative term would be pointless, because the radiation will play an increasingly important role in transporting the deposited energy away from the impact site at later time. Assuming that all the deposited energy is carried upward by the atmospheric plume which is a factor of 40 more massive than the impactor, and all the energy is converted to gravitational potential energy, the plume can reach the altitude of $\sim$ 3000 km at $\sim$ 10 minutes for a 2-km fragment. The lateral spreading radius can be calculated using the self-similar relations [Zel'dovich and Raizer, 1967] and at the 1-bar level, the resulting plume diameter expands to 250 km at 100 seconds, 650 km at 10^3 seconds, and 10^3 km in an hour after impact of a fragment D = 2km. If the Jovian atmosphere and the plume were transparent so that the plume could emit the deposited energy to space directly, the radiative heat loss would become more important during the evolution of the plume.

The radiative behavior is controlled by the atmospheric opacity and is not easily calculated, because the opacity of atmospheric constituents changes as a function of temperature. In the ambient atmosphere, during the first 10^1 seconds, when the impactor releases its kinetic energy to the gas along its path, it will not lose its energy laterally by radiation due to the presence of CH_4, which is a strong IR absorber, and the existence of Jupiter's cloud deck will result in strong radiative scattering backward toward the entry direction. The inside of the plume becomes less dense as the plume develops between 10^1 to 10^2 seconds; the low density of the expanding plume leads to longer mean free paths, allowing radiative heat transfer to become dominant [Brode, 1968]. Assuming blackbody radiation behavior from a spherical area of radius $\sim 10^3$ km, the plume could emit for $\sim$ 1 hour with the average effective temperature, $T_e \simeq 10^3$ K, and eventually upon further mixing, Jupiter will lose the deposited energy in $\sim$ a week with the average $T_e \simeq 200$ K for a cometary impact of D = 2 km. From this approximation, the radiation will be dominant in the UV and visible wavelengths for the first $< 10^3$ seconds. Then as the plume expands and has a wider area of a radius $\simeq 10^3$ km, the effective radiative wavelength gradually shifts from visible to infrared. From the SPH results, Ahrens et al. [1994] found that after 10^2 seconds, the radiance is most intense at visible wavelengths for $D = 2$ km.

In the case of smaller objects, from our calculation of the 400-m impact, the first flash will be expanded in a relatively small region in 10^2 seconds up to the radial distance of 10^2 km with the temperature of $\sim$ 500 K at 1-mbar pressure level and up to the radial distance of 50 km at 1-bar pressure level. Assuming that the radiation occurs in the area of radius $\sim 10^3$ km for $\sim$ 1 hour, the average effective temperature, $T_e \simeq$ 300 K; that is approximately twice as high as the ambient atmospheric temperature. Therefore, for the smaller objects of $\sim 10^2$ m, the post-impact phenomena will be mainly observable in the infrared region.

The effect of the plume on the magnetosphere is hard to predict. The plume only reaches ~ 0.1 the altitude of the magnetosphere, although the expansion of the magnetosphere by ionized material of the cometary comae may produce observable electromagnetic effects. The observed dust tail of SL-9 may be trapped by the magnetosphere before and after the impact of solid fragments [Dressler and Sandel, 1993]. This also may form enhanced Jovian ring [Horanyi, 1993].

The Solid-State Imaging experiment on the Galileo spacecraft will be able to view the impact site directly from 1.6 AU away from Jupiter with a resolution of 2000 km [Johnson, 1993]. Even though the entry flash may occur in a smaller region ($< 10^2$ km), the radiated energy will be intense enough to be observed by the optical instruments directly, since the effective temperature is $\sim 10^2$ orders of magnitude greater than the intrinsic effective temperature of Jupiter ($\sim$ 120 K). Therefore, Galileo will be able to capture the moment of impact, entry flash, and the resulting plume evolution, even without detailed spatial resolution on the planetary disk.

The plume is expected to be in view of the earth at ~ ten minutes after the impact, rising over the SW horizon of Jupiter if enough mass is ejected into the space. Since this side of the planet will be in early morning darkness, initial detection must rely on observing its thermal radiation. However, at later time, the plume will be illuminated by the sun. The impact site will rotate into view from the earth at about 20 minutes after the impact. The plume will grow to sufficient size that it will be visible when observed from the ground-based instruments at this time for the impact of a radius $\geq 10^2$-m fragment. The Hubble Space Telescope and some ground-based instruments will be able to observe the radiated plumes that contain samples of the atmosphere below the cloud decks as well as the cometary materials.

The impact of the fragments is expected to occur over at period of seven days with more than 20 impacts. Because of the short rotation period of Jupiter (~ 10 hours), the impact sites of different fragments will be located at different positions at 48° S latitude on Jupiter. We can expect a band of width $10^3 - 10^4$ km at this latitude in which infrared radiation changes and in which atmospheric circulation may be disturbed.

We hope that our predictions will be utilized by observers who intend to observe the impacts and subsequent phenomena in the middle of July 1994. The event will also enhance our knowledge of the composition of Jupiter's troposphere as well as provide good tests for the various models of cometary impact and resulting plume evolution.

6. Acknowledgements

Research was supported by NASA and Cray Research Corp. All the SPH calculations were carried out on the CRAY-YMP at Jet Propulsion Laboratory. We thank W. W. Anderson for comments on this paper. We thank B. Sturtevant, D. A. Crawford, M. M. Mac Low, W. Benz, A. M. Vickery, H. Kanamori, A. P. Ingersoll,

D. J. Stevenson, J. Freidson, and K. Zahnle for helpful discussions. We also thank P. Weissman, M. A'Hearn, and K. Ziemelis for helpful comments and M. Lainhart for his technical support. We thank M.B. Boslough and an anonymous reviewer for improving the manuscript. Contribution number 5378, Division of Geological and Planetary Sciences, California Institute of Technology.

References

Ahrens, T. J. and J. D. O'Keefe, 1977. Equation of State and Impact-Induced Shock-Wave Attenuation on the Moon in *Impact and Explosion Cratering*, Roddy, D. J., Pepin, R. O., and Merrill, R. B., eds. Pergamon Press, New York, p 639-656.

Ahrens, T. J., T. Takata, J. D. O'Keefe, and G. S. Orton, 1994. Radiative Signals from Impact of Shoemaker-Levy on Jupiter. (abstract) *Lunar. Planet. Sci. XXV*, 5-6.

Alvarez, L. W., W. Alvarez, F. Asaro, and H. V. Michel, 1980. Extraterrestrial Cause for the Cretaceous-Tertiary Extinction. *Science* **208**, 1095-1108.

Atreya, S. K., 1986. *Atmospheres and Ionospheres of the Outer Planets and the Satellites.* Springer-Verlag, New York, pp.224.

Boslough, M. B., D. A. Crawford, M. E. Kipp, T. G. Trucano, and J. M. McGlaun, 1993. Simulations of Cometary Interaction with Jupiter: Preliminary 2D and 3D Calculations of the Sensitivity of the Event to Bolide Representation and Angle of Incidence. *Bull. Am. Astron. Soc.* **25**, 1043.

Brode, H. L., 1968. Review of Nuclear Weapons Effects. *Ann. Review. Nuclear Sci.*, **18**, 153-202.

Bronshten, V. A., 1983. *Physics of Meteoric Phenomena.* D. Reidel Publishing Co., Boston, pp.356.

Crawford D. A., T. G. Trucano, M. B. Boslough, M. E. Kipp, and J. M. McGlaun, 1994. The Influence of Body Shape on the Deformation and Breakup of Comet Shoemaker-Levy 9 Fragments as They Enter the Jovian Atmosphere. *Lunar. Planet. Sci. XXV*, 295-296.

Chyba, C. F., P. J. Thomas, and K. J. Zahnle, 1993. The 1908 Tunguska Explosion: Atmospheric Disruption of a Stony Asteroid. *Nature*, **361**, 40-44.

Cloutman, L. D., 1990, Basics of Smoothed Particle Hydrodynamics. Lawrence Livermore National Lab., UCRL-ID-103698, pp.47.

Dressler, A. J. and B. R. Sandel, 1993. Magnetospheric Effects of Comet Shoemaker-Levy. *EOS*, **74**, 43, 391.

Gautier, D., B. Conrath, M. Flasar, R. Hanel, V. Kunde, A. Chedin, and N. Scott. 1981. The Helium Abundance of Jupiter from Voyager. *J. Geophys. Res.* **86**, 8713-8720.

Horanyi, M., 1993. New Jovian Rings. *EOS*, **74**, 43, 391.

Ingersoll, A. P., 1993. Meteorological Effects of the Encounter of Comet P/Shoemaker - Levy (1993e) with Jupiter. *EOS*, **74**, 43, 391.

Ivanov, B. A., 1988. Simple Hydrodynamic Model of Atmospheric Breakup of Hypervelocity Projectiles. (abstract) *Lunar. Planet. Sci. XIX*, 535-536.

Ivanov, B. A., I. V. Nemchinov, V. A. Svetsov, A. A. Provalov, V. M. Khazins, and R. J. Phillips, 1992. Impact Cratering on Venus: Physical and Mechanical Models. *J. Geophys. Res.*, **97**, E10,16167-16183.

Jewitt, D., J. Luu, and J. Chen, 1993. Physical Properties of Split Comet Shoemaker-Levy 9. *Bull. Am. Astron. Soc.*, 25, 1042.

Johnson, T. V., 1993. Shoemaker/Levy Observations from Galileo. *Bull. Am. Astron. Soc.* **25**, 1044.

Lindal, G. F., G. E. Wood, G. S. Levy, J. D. Anderson, D. N. Sweetnam, H. B. Hotz, B. J. Buckles, D. P. Holmes, P. E. Doms, V. R. Eshleman, and G. L. Tyler, 1981. The Atmosphere of Jupiter: An Analysis of the Voyager Radio Occultation Measurements. *J. Geophys. Res.* **86**, 8721-8727.

Lucy, L. B., 1977. A Numerical Approach to the Testing of the Fission Hypothesis. *Astron. J.* **82**, 1013-1024.

Mac Low, M. M. and K. Zahnle, 1994. Explosion of Comet Shoemaker - Levy 9 on Entry into the Jovian Atmosphere. *Nature* submitted.

Melosh, H. J., 1989. *Impact Cratering*, Oxford University Press, New York, pp.245.

Monaghan, J. J., 1992. Smoothed Particle Hydrodynamics. *Ann. Rev. Astron. Astrophys.*, **30**, 543-574.

Moran, B. and R. Tipton, 1993. Simulation of a Comet Impact on Jupiter. *EOS*, **74**, 43, 389.

O'Keefe, J. D., and T. J. Ahrens, 1977. Impact - Induced Energy Partitioning, Melting, and Vaporization on Terrestrial Planet, *Proc. Lunar Sci. Conf. 8th*, 3357-3374.

O'Keefe, J. D. and T. J. Ahrens, 1982. Cometary and Meteorite Swarm Impact on Planetary Surfaces. *J. Geophys. Res.*, **87**, 6668-6680.

O'Keefe J. D., T. Takata, and T. J. Ahrens, 1994. Penetration of Large Bolides into Dense Planetary Atmosphere - Role of Hydrodynamic Instabilities. (abstract) *Lunar. Planet. Sci. XXV*, 1023-1024.

Prinn, R. G. and B. Fegley, Jr., 1989. Solar Nebula Chemistry: Origin of Planetary, Satellite and Cometary Volatiles. *Origin and Evolution of Planetary and Satellite Atmospheres*, p. 78-136, S.K. Atreya, J. B. Pollack, and M. S. Matthews eds., The Univ. of Arizona Press, Tucson.

Schultz, P. H. and D. E. Gault, 1992. On Surviving Atmospheric Entry. (abstract) *Lunar. Planet. Sci. XXIII*, 1235-36.

Scotti, J. V. and H. J. Melosh, 1993. Tidal Breakup and Dispersion of P/Shoemaker-Levy 9: Estimate of Progenitor Size. *Nature* **365**, 733-735.

Sekanina, Z. 1993. Disintegration Phenomena Expected During Collision of Comet Shoemaker - Levy 9 with Jupiter. *Science* **262**,382-387.

Sekanina, Z., P. W. Chodas, and D. K. Yeomans, 1994. Tidal Disruption and the Appearance of Periodic Comet Shoemaker - Levy 9. Submitted to *Astron. J.*

Shoemaker, C. S., E. M. Shoemaker, and D. H. Levy, 1993, IAU Circ., 5752.

Stevenson, D. J., 1993. After the First Minutes. *EOS*, **74**, 43, 390.

Stellingwerf, R. F., 1990. Smooth Particle Hydrodynamics. *Lecture Notes in Physics, 395, Advances in the Free-Lagrange Method*, Springer-Verlag, Heidelberg FRG, 239-247.

Takata, T., T. J. Ahrens, and R. J. Phillips, 1994. Atmospheric Effects on Cratering on Venus, submitted to *J. Geophys. Res.*

Turco, R. P., O. B. Toon, C. Park, R. C. Whitten, and J. B. Pollack, 1982. The Analysis of the Physical, Chemical, Optical, and Historical Impacts of the 1908 Tunguska Meteor Fall. *Icarus*, **50**, 1-52.

Vickery, A. M. 1993. Numerical Simulation of a Comet Impact on Jupiter. *EOS*, **74**, 43, 391.

Weaver, H. A., P. D. Feldman, M. F. A'hearn, and C. Arpigny, 1994. Hubble-Space Telescope Observations of Comet-P/Shoemaker-Levy 9 (1993e). *Science.* **263**, 787-791.

Yeomans, D. K. and P. Chodas, 1993, IAU Circ., 5909.

Zahnle, K., 1992. Airburst Origin of Dark Shadows on Venus. *J. Geophys. Res*, **97**, 10243-10255.

Zahnle, K. and M. M. Mac Low, 1994. The Collision of Jupiter and Comet Shoemaker-Levy 9. *Icarus*, in press.

Zel'dovich, I. B. and Y. P. Raizer, 1967. *Physics of Shock Waves and High-Temperature Hydrodynamic Phenomena*, Chap. 12. Academic Press, New York, pp.916.

PAPER III

Comet Shoemaker-Levy 9: Fragment and Progenitor Impact Energy

Comet Shoemaker-Levy 9: Fragment and Progenitor Impact Energy

Toshiko Takata, Thomas J. Ahrens

Lindhurst Laboratory of Experimental Geophysics
Division of Geological and Planetary Sciences
California Institute of Technology
Pasadena, CA 91125

Division of Geological and Planetary Sciences
California Institute of Technology
Pasadena, California 91125

Glenn S. Orton and Andrew J. Friedson

Jet Propulsion Laboratory
California Institute of Technology
Pasadena, California 91109

to be submitted to *Nature*

Abstract

Preliminary observational data from the impact of fragments of Comet Shoemaker-Levy 9 (SL9) are compared with smoothed particle hydrodynamic (SPH) and radiative calculations to determine the energies of individual SL9 fragments and the equivalent diameter of the SL9 progenitor. The Hubble Space Telescope (HST) images of the G impact-induced plume demonstrate that it achieved a height of ~3300 km [Hammel et al., 1994]. This is in close agreement with the SPH calculations for a 7×10^{28} erg or 2 km ± 0.3 km diameter solid ice impactor at 60 km/sec. Comparison of the R fragment impact-induced plume brightness in the 8 to 12 μm band, as recorded by the NASA Infrared Telescope Facility (Mauna Kea, HI) [Orton et al. 1994], with our radiative predictive calculations yields a kinetic energy of 4×10^{28} ergs or a diameter of 1.6 ± 0.3 for the R fragment. Using the G and R impacts to calibrate Weaver et al.'s [1994] detailed photometric determination of the relative diameters of pre-Jovian impact projectiles in the SL9 chain from HST images yields revised values for the 11 largest fragment diameters. Adding the inferred masses from the plume and radiative calibration of Weaver et al.'s catalog yields an SL9 progenitor equivalent (ice) diameter of 4.1 ± 0.6 and 3.5 ± 0.5 km, respectively. This compares to a 7.7 km diameter progenitor inferred by Weaver et al. and a 2 km diameter progenitor obtained using tidal break-up modeling by Scotti and Melosh [1993] and Asphaug and Benz [1994]. We also examined the inferred position of Jupiter derived H_2O impact ejecta from the hypothetical (3 to 5 bar) cloud deck and find that although Jupiter derived impact induced plumes having radius of $> 10^3$ km and achieved altitudes of 3×10^3 km, the contained Jovian water ejecta is restricted to the interior of the plume and would be masked from Earth observations by the surprisingly opaque plume. On the basis of Bjorker et al.'s [1994] observations of thirty minutes' water emissions from the plumes of the impact sites of fragments G and K Field and Ferraro's [1994] analysis

which indicates that even if SL9 fragments are 50% porous, upon being subjected to entry, the ram pressures, upon reaching the level of 1 bar, squeeze-out virtually all porosity and the present, self-consistent kinemetric and radiative coupling of the SL9 impactor, we conclude: 1) there is no evidence that SL9 was anything but a comet as first suggested by the coma, 2) penetration of 2 km diameter fragments occurs to depths of $\sim$ 300 km, even for a porous comet, as calculated by the present SPH method and by other groups using finite difference methods [Zahnle and MacLow, 1993, Boslough et al., 1994].

1. Introduction

The most spectacular event ever witnessed by humankind was the recent impact of fragments of Comet Shoemaker-Levy 9 (SL9) on Jupiter that occurred during the period of 16 to 21 July 1994. Undetected until 25 March 1993, this (initial 4 km diameter) comet was tidally disrupted into some 21 fragments upon peri-Jovian passage within the Roche-limit on or about 7 July 1992 [Scotti and Melosh, 1994]. An enormous amount of data is becoming available which requires analysis. Previously we predicted observable phenomena based on calculations using the Smoothed Particle Hydrodynamics (SPH) method. We studied the entry of the cometary fragments into the Jovian atmosphere and the subsequent plume evolution induced by the deposition of the impact energy. We predicted [Takata et al. 1994, Ahrens et al., 1994a,b] the radiance of the impact flash and the subsequent plume radiance over a range of infrared and visible wavelengths using fragment sizes previously estimated on the basis of Hubble Space Telescope (HST) photometric measurement [Weaver et al., 1994] and theoretically derived from the description of tidal disruption of the SL9 parent body [Scotti and Melosh, 1993; Asphaug and Benz, 1994].

Here we attempt to interpret the preliminary SL9 impact observations by comparing these with our predictions. The impact of SL9 with Jupiter presents unique opportunities to test our understanding of many aspects of impact physics, which has been an area of active research, since the importance of impact cratering as a geologic process in the solar system was first recognized.

The impact energy of the SL9 fragments is the most important parameter required for undertaking calculations of the impact phenomena and the subsequent effects on Jovian atmosphere. Although the velocity of the fragments (60 km/s) was well known from orbital determination [Yeomans and Chodas, 1993], the actual fragment sizes and densities were uncertain. The numerical models of Scotti and Melosh

[1993] and Asphaug and Benz [1994] used to reproduce the orbital position of the line of fragments after the break-up demonstrated that the diameter of the parent body was < 2 km and the total expected energy was $\sim 8 \times 10^{28}$ ergs. The photometric measurements obtained with the HST yield an estimated solid ice, 7.7 to 10 km diameter parent body [Weaver et al, 1994]. Upon impact with Jupiter, a total impact energy of 4.3 to 9.4 $\times 10^{30}$ ergs, if a fragment density of the fragments of 1 g/cm^3 is assumed. Thus, there was an uncertainty of more than two orders of magnitude in the total kinetic energy of all the fragments.

We employ two methods to estimate the impact energy and the mass of fragments. One is to calculate the radiative energy flux versus wavelength from an impact site, and compare this with observed radiative signal. Secondly, we compare the impact-induced plume with numerical and analytical calculations for different impact energies.

2. Plume Size and Impact Energy

In this section, the size of plume generated by the impact of SL9 fragments is investigated. Here, 'plume' represents the shock-heated gas rising up in the inhomogeneous Jovian atmosphere. Our SPH simulations [Takata et al., 1994, Ahrens et al., 1994a] demonstrated that the impact energy deposited in the Jovian atmosphere results in the rise of shocked atmospheric gas to more than several tens of scale heights. The plume size, especially the maximum height, is strongly dependent on the impact energy. We compared observed plume height and lateral dimensions with the SPH results.

The radial size of the plume generated by the impact of a 2-km fragment at altitudes of 0 km, 200 km, and 300 km is plotted in figure 1. Here, 0 km represents the 1-bar-pressure level. After 10^2 seconds of plume expansion, the plume radii in the troposphere and stratosphere (below 1μbar pressure level) agree with a self-similar cylindrical shock expansion rather than the self-similar spherical expansion [Zeldovich and Raizer, 1966]. This implies that once the energy is deposited at each altitude, it is approximately conserved. The lateral propagation of the strong shock wave induces strong heating of the atmosphere surrounding the impact trajectory. This shock wave attenuates to a sonic wave as it propagates. Since the increased temperature of the plume relative to the ambient atmosphere is a direct result of shock heating around the impact site, the observed lateral radius of the plume, particularly at infrared wave lengths, reflects the radius of the propagating shock wave. After impact of a 2 km diameter fragment, Figure 1 shows that the radius of the plume reaches 900 km at an altitude of 200 km and 1500 km radius at the altitude of 300 km in the Jovian stratosphere.

The atmospheric gas ejected above the stratosphere is gravitationally-bound and assumes a parabolic trajectory in 10^1 minutes. This atmospheric gas reimpacts a distance at $\sim$ 4h from the ejection point, where h is the maximum height of the plume. If the plume reaches $\sim$ 3300 km, as in the case of the G impact, the maximum radial distance of the atmospheric gas from the impact site reaches $\sim$ 12000 km. The primary observable change in this region will be at optical rather than thermal wavelengths. This result agrees with the position of the crescent shape dark region observed after impact, at the site of the fragment G impact [Hammel et al., 1994] which has a radius of 10000-14000 km centered on the impact point.

Next we compare plume height from SPH calculations and observed height. In figure 2, the plume heights obtained from the SPH simulations for 400 m- and 2 km diameter fragments are shown [Takata et al. 1994]. These impacts have energies of 6×10^{26} and 7×10^{28} erg, respectively. Here we assume, for the 2-km fragment, that all of the kinetic energy is converted to gravitational energy, as a lower limit to the final plume height (2600 km), and that all the kinetic and internal energy is converted to

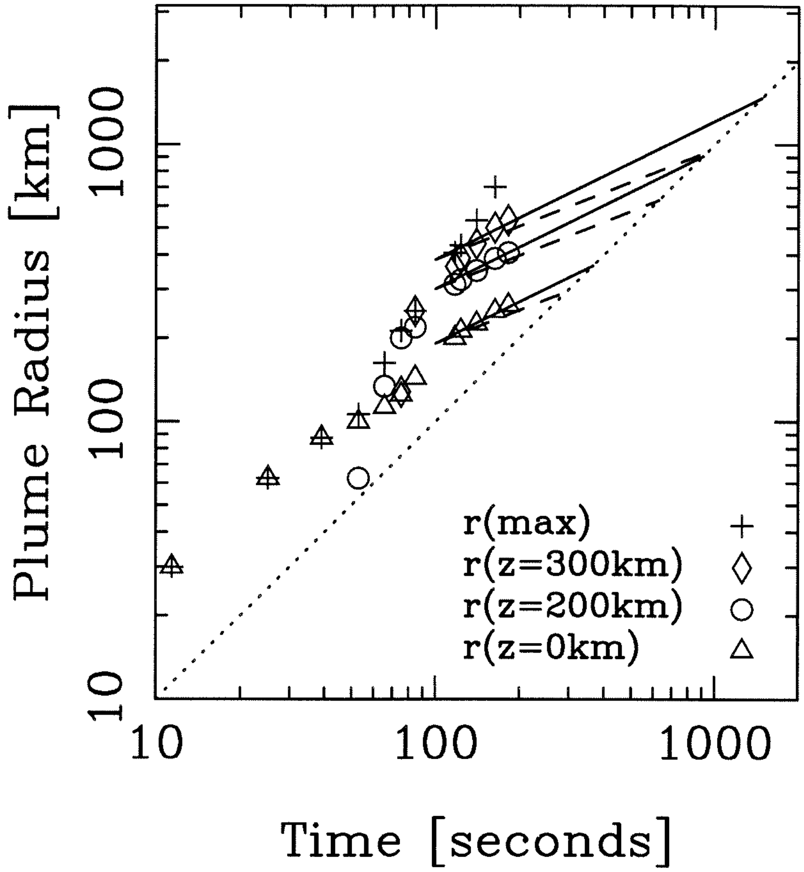

Figure 1. Radial size of the plume generated by the impact of 2 km size-comet. Symbols of △, ○, and ◊ represent the radial plume sizes at the altitude of 0 km (troposphere), 200 km, and 300 km (stratosphere), respectively. + represents the maximum radial extent of the plume. Solid lines and dashed lines represent the slopes of radial distance versus time which are in proportion to $t^{0.5}$ and $t^{0.4}$, corresponding to the self-similar cylindrical and spherical expansion of blast waves [Sedov, 1959]. Dotted line indicates the approximate similarity solution sonic wave limit.

gravitational energy as an upper limit of the ballistic trajectory height (4000 km). On average, the plume produced by the 2-km fragment rises ~ 3300 ± 700 km above the 1-bar pressure level.

The preliminary plume height of fragment G observed by HST is 3300 km [Hammel et al., 1994]. The curve of plume development is also shown in Fig. 2.

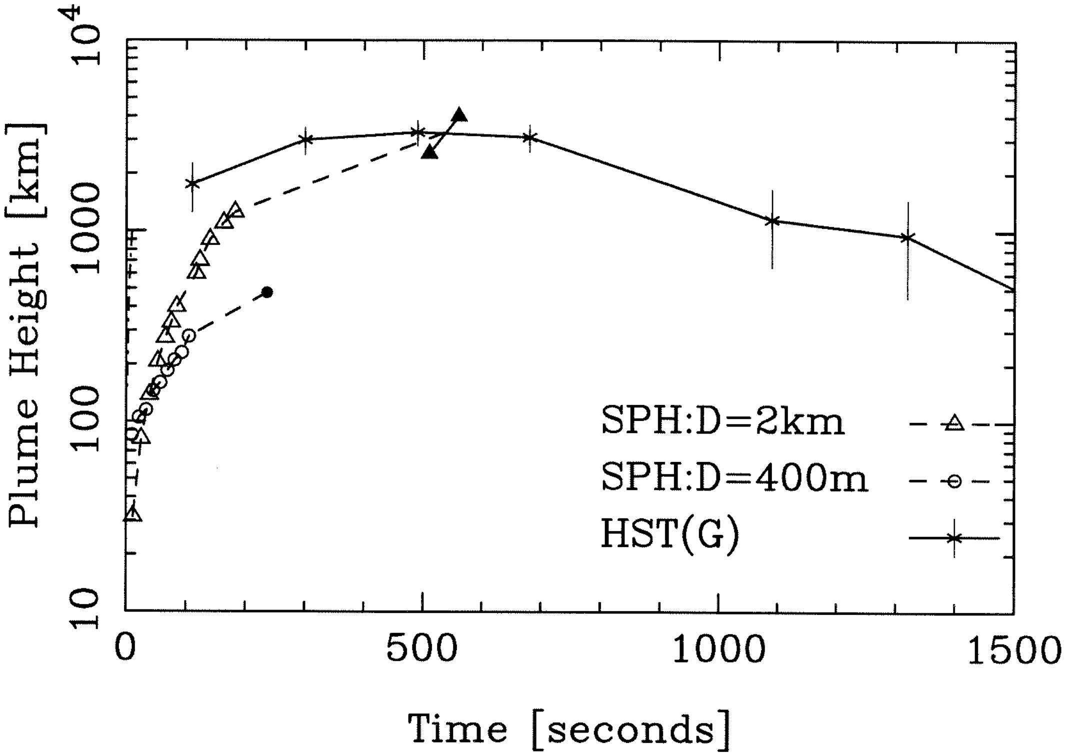

Figure 2. Comparison of plume height obtained from SPH calculations with Hubble Space Telescope (HST) observational results. The SPH calculation is for the comet fragment with the diameter of 2 km and 400 m. Here, 0 km height represents the 1 bar pressure level. Symbols, o, represents an SPH plume simulation for the impact of D = 400 m; • indicates maximum height for D = 400 m extrapolated from the SPH simulation; △ indicates SPH simulation for the impact of D = 2 km; and △ represents maximum height for D = 2 km impact extrapolated from the SPH simulation. The symbol $*$ indicates HST observation of fragment G as a function of time [Hammel et al., 1994].

Interpolation of maximum plume height using the SPH simulations summarized in Fig. 2 yield a cometary fragment diameter of $\sim 2 \pm 0.3$ km, or impact energy of 8×10^{28} erg on Jupiter, assuming density of $\rho = 1$ g/cm^3 for the G impactor. Direct HST photometric observations suggest that the fragment G is $\sim$ 3.5 km in diameter [Weaver et al. 1994]. In contrast, scaling the fragment size distribution from Weaver et al.'s observations to the results of Scotti and Melosh [1993], who inferred a parent body diameter of $\sim$ 2 km, a diameter of fragment G, of $\sim$ 700 m would be obtained. Therefore, the diameter of the G impactor we obtain, 2 ± 0.3 km, is intermediate between estimates of 3.5 km from Weaver et al. [1991] and 0.7 km from Scotti and Melosh [1993].

3. Radiative Signature and Impact Energy

In this section, we compare the radiative flux inferred from our SPH simulations [Ahrens et al., 1994b] with the preliminary absolute radiance of the plume from fragment R observed by the NASA InfraRed Telescope Facility (IRTF) [Orton et al., 1994]. In figure 3, calculated energy flux versus wavelength for 400 m and 2 km-size fragment at the earth and the results of IRTF are shown. The radiative curve of SPH simulation is obtained assuming each atmospheric particle is a blackbody radiator disc. Then the total normal radiative power is calculated and converted to the energy flux observed from the earth's orbit. The calculations represent the radiance some 10^2 seconds after the impact whereas the observations correspond to a peak in radiance observed 4 minutes after impact. The blackbody temperature that fits the IRTF data is approximately 1600 K, whereas plume temperatures calculated for 2 km- and 400 m-size fragments are $\sim$ 2000 K and $\sim$ 500 K, respectively.

Assuming blackbody radiation, and interpolating logarithmically the radiative signature suggests R fragment impact energies of $3.5 \pm 3.0 \times 10^{28}$erg. Assuming that the radiative flux is proportional to the impact energy at 7.8 and 10 microns, and the R fragment density is 1 g/cm^3, the estimated fragment size is $\sim 1.6 \pm 0.3$ km.

The preliminary HST observations of fragment G indicate that the plume temperature is $\sim$ 1500 K at t $\sim$ 2 minutes after the impact. From SPH results, the temperature of the plume-head is $\sim$ 2000 K for the D = 2 km fragment and $\sim$ 500 K for the D = 400 m fragment after 100 seconds. Therefore, the deposited energy is fairly well defined on the basis of these comparisons. The diameter of fragment R is inferred to be 3.4 km from Weaver et al. [1994] and the corresponding estimated size, applying the size distribution of Weaver et al. [1994] to the progenitor size obtained

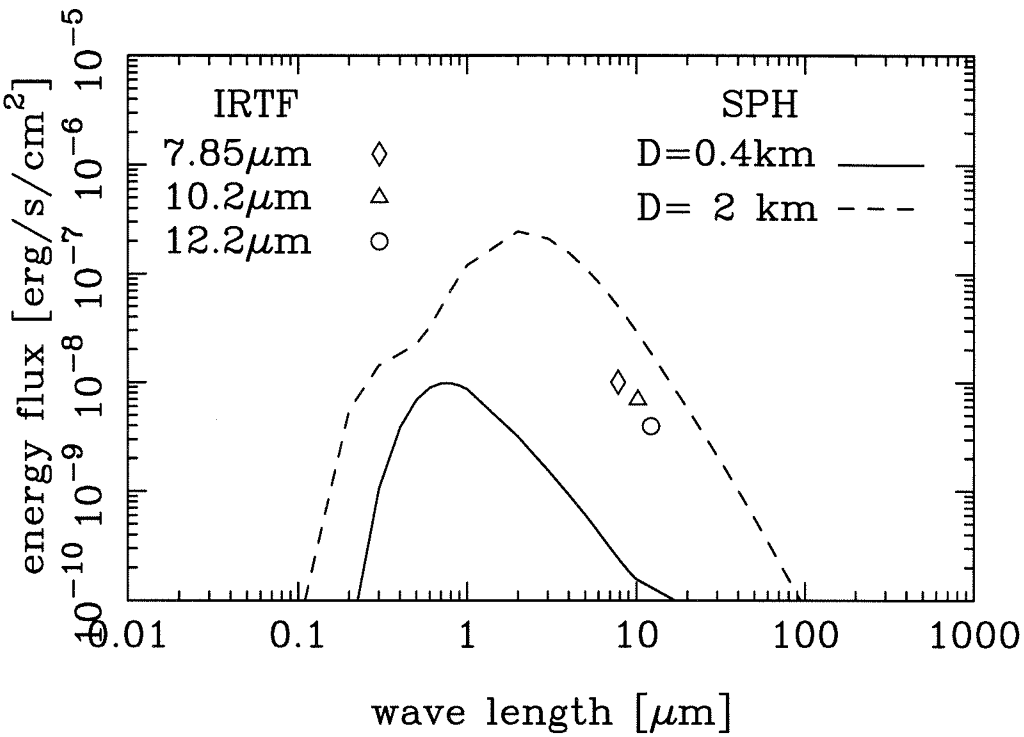

Figure 3. The comparison of the SPH radiative flux [Ahrens et al., 1994b] with the IRTF observation [Orton et al., 1994]. The calculated radiative flux at the earth orbit from SPH is shown by dashed line for the D = 400 m and by solid line for the D = 2 km. These represent the calculated radiative flux at t = 10^2 seconds after the impact. The IRTF results are for CH_4 bands of 7.85 μm, 10.2 μm, and 12.2 μm, respectively, then peak values occur $\sim$ 4 minutes after impact. Assuming the black body radiation, these data locate between the radiative profiles of D= 400 m and D = 2 km calculated from SPH numerical simulation.

by Scotti and Melosh [1993], is $\sim$ 600 m. Therefore, the present energy of R impactor lies between two previous estimates.

4. Total Impact Energy and the Progenitor Size

Using the values obtained in the previous two sections, the progenitor SL9 size is calibrated with relative sizes of fragments obtained by Weaver et al. [1994] photometrically. After impact, we now know that the photometric brightness of each fragment before the impact is not simply related to the magnitude of the impact

Fragment ID	Diameter [km] from Weaver et al.	Diameter[km] from plume height	Diameter [km] from radiance scaling
C	2.5	1.3	1.1
E	3.0	1.6	1.4
F	2.9	1.5	1.3
G	3.8	**2.0±0.3**	1.7
H	3.1	1.6	1.4
K	3.9	2.1	1.8
L	3.9	2.1	1.8
Q	4.3	2.3	2.0
R	3.4	1.8	**1.6 ± 0.3**
S	3.4	1.8	1.6
W	3.1	1.6	1.4
Total 11 fragments Progenitor size	7.7	4.1 ± 0.6	3.5 ± 0.5

Table 1. Estimated size of the 11 largest SL9 fragments. The diameters in the first column are the size distribution estimated from the pre-impact photometric observation by Weaver et al. [1994]. The size of fragment, G, evaluated by the comparison of plume heights between SPH simulations and the HST observations [Hammel et al., 1994], and all other fragment diameters calibrated from the size distribution of Weaver et al. [1994], are in the second column. The third column shows fragment sizes estimated from the radiance of fragment, R, from SPH simulations and IRTF observations [Orton et al. 1994].

energy. However, we apply Weaver et al.'s determination of diameter distributions, as a first approximation. In Table 1, the photometrically determined diameter from Weaver et al. [1994] and the diameters scaled from the comparison of plume height for fragment G and that of radiance for fragment R are listed.

The SL9 progenitor size, which Weaver et al. obtained for the 11 brightest fragment was 7.7 km. We obtain from comparison of theoretical and 4.1±0.6 km from observed plume height, and 3.5 ± 0.5 km from comparison of theoretical and observed radiance.

5. Discussions

The HST team detected radiation from the following species: Mg, Mg^{++}, Mg^{+}, CS, and Fe [Noll et al., 1994]. However, no water molecules, atoms, or ions are presently reported as being detected at any ground-based observational site. Bjoraker et al. [1994], using the Kuiper Echelle Grating Spectrometer on the Kuiper Airborne Observatory, detected emission from H_2O for G and K fragments for about a half-hour after these impacts. They inferred from their data that the temperature was > 500 K and concluded that P/Shoemaker-Levy 9 was of cometary, and *not* of asteroidal, origin.

A water cloud layer is also believed to exist at $P \sim 3$-5 bar in the Jovian atmosphere. If the size of fragments are ≥ 1 km, and these are approximately spherical bodies, all the numerical models for the entry [Takata et al., 1994, Mac Low and Zahnle, 1994, Boslough et al., 1994, and Wingate et al., 1994] suggest that such massive objects should reach the water cloud layer and eject some of the constituents of the deep atmosphere.

5.1 Plume structure

One possible explanation of the difficulty of water detection is that according to the results of Fig. 4, water, and other constituents of Jupiter's interior, appear to be present only in the center of the plume and not on its presumably opaque surface. The plume is defined in the infrared largely by radiation from methane bands and at visible wavelengths by radiation from sulfur compounds and possibly metallic ions from the comet. Thus we infer these mask radiation from OH^- and H_2O molecules.

Boslough [personal communication, 1994] has independently come to the same conclusion. Figure 4 shows the plume from a 2 km fragment some 2 minutes after impact. The spatial distribution of the atmospheric gas originated from different regions are indicated as follows: stratosphere ($\cdot$), NH_3 cloud layer ($\circ$), NH_4SH cloud layer ($\bigcirc$), and material below the pressure levels where the water cloud is expected to exist($\triangle$). The stratospheric plume of Fig. 4 rises up to 900 km, whereas the atmosphere originated from below expecting water cloud deck rises only 270 km above 1 bar-pressure level. Similarly, the lateral diameter of the plume is $\sim 10^3$ km, whereas the material from the expecting water cloud deck has laterally expanded only $\sim$ 300 km.

We conclude that deep atmospheric gas exists within the lower 1/3 of the overall dimensions of the plume and remains deep inside of the plume for a long time, whereas the water lines extinct at half an hour after the impact only in the cases of large fragments. This explains that CH_4 spectra was observed for most of the SL9 plumes. We note that CH_4 is the major infrared emitter in the stratosphere.

Infrared observations [Orton, et al. 1994] indicate that the temperature of the impact site below several bar pressure level did not change appreciably after the impact, and hence, it is claimed that the fragments did not penetrate into these pressure levels. However, the lateral size of the plume and the resultant heated gas varies as a function of altitude. In the stratosphere, plume radii exceeded 2×10^3 km for many of the impacts. Moreover, the lateral "plume stalk" within the troposphere expanded to less than 300 km even for the largest (2 km diameter) impactors. We infer that available telescopic resolution was not enough to detect the small scale (10^2 km) radiation from deeper constituents, or the radiation from lofted water was blocked by the opacity of the stratospheric plume. We conclude that penetration at least to the several bar-pressure levels did occur upon impact of SL9.

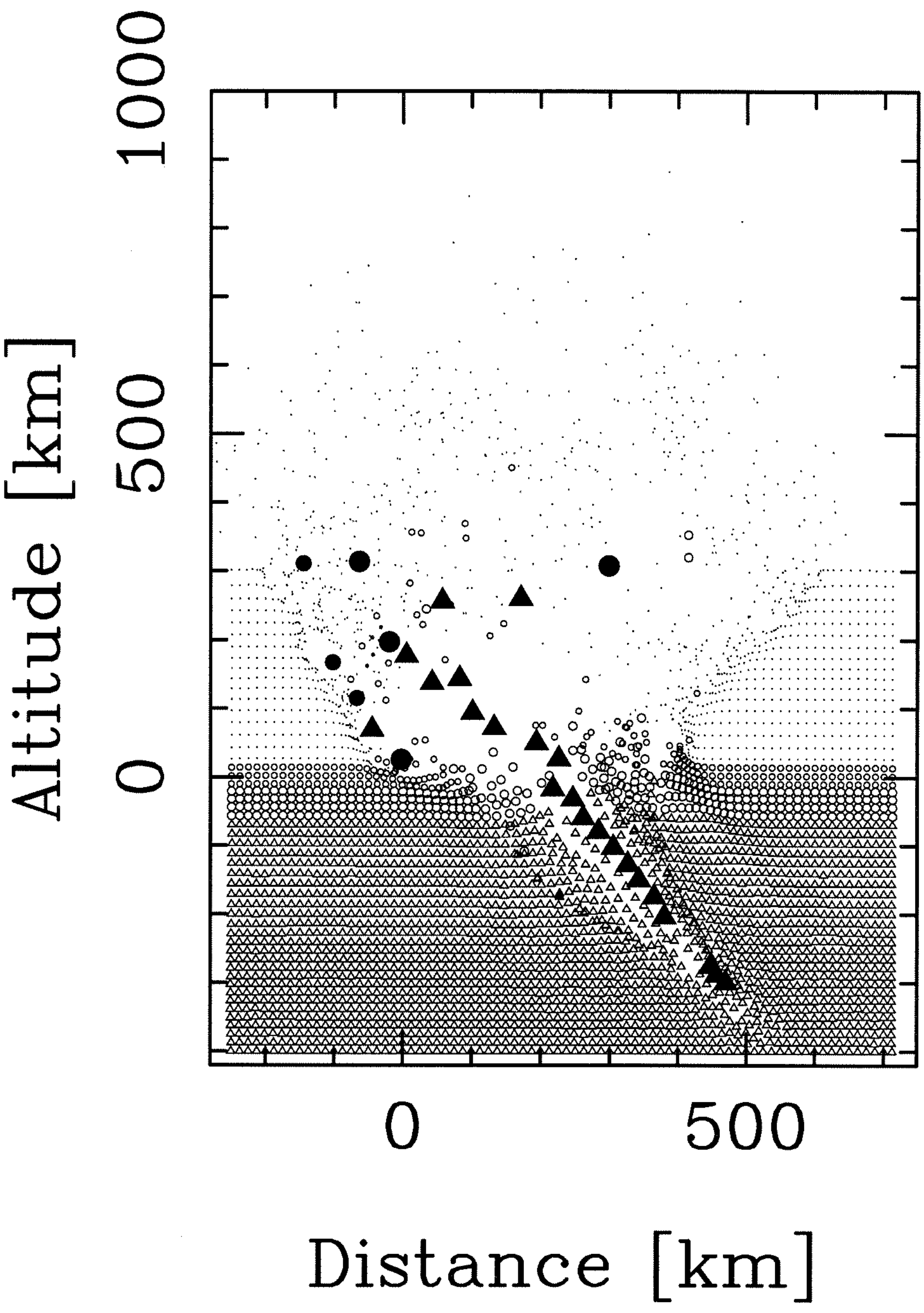

Figure 4. SPH results of plume expansion in the case of the impact of 2 km size-fragment after 123 seconds. △ shows the atmospheric particles originated from the Jovian atmosphere below 4 bar ($Z <$ -60 km). The atmosphere in this region is considered to be a reservoir of H_2O molecules. ∘ and ○ represent atmospheric particles originated from the Jovian atmosphere between 400 mbar and 1.3 bar (20 km $> Z >$ -10 km), and between 1.3 bar and 4 bar (-10 km $> Z >$ -60 km), respectively. NH_3 and NH_4SH cloud layers exist in these atmospheric regions, respectively. · represents the optically (transparent) atmosphere above cloud layers. CH_4 is the major minor constituents at this altitude. Filled symbols represent the atmospheric particles initially located at cometary trajectory. These include cometary materials too.

5.2 Some comments on Jovian atmospheric structure

In the Jovian atmosphere, the thick ammonia cloud fragments at an altitude of 5-10 km and pressures 0.5 to 0.7 bars, prevents terrestrial-based observation of the deeper atmosphere. The chemical structure of the atmosphere is not well known below that pressure level. The detection of the water in Jovian atmosphere has long been attempted; however, the results have been mixed. Drossart and Encrenaz [1982], using the Voyager I, Interferometer Spectrometer and Radiometer (IRIS) data detected H_2O (in the gas phase) at a level of $4 \pm 1 \times 10^{-6}$ (mole fraction), and found it to be depleted by a factor of 100 from the cosmic abundance. However, a later analysis by Carlson et al. [1992] of the same data found a water abundance at 1.5 - 2.0 times solar abundance. The water vapor in the Jovian troposphere above the 6 bar pressure level was measured by Bjoraker [1985] using the Kuiper Airborne Observatory. This measurement depended on conducting observations through holes in the ammonia clouds. Bjoraker's [1985] observations yielded a water depletion of a factor 40 to 100 relative to solar abundance between 2 and 6 bars in the Jovian atmosphere. This result agrees with Drossart and Encrenaz [1982].

The original idea underlying the proposition that a water cloud is expected to exist at the $\sim$ several bar pressure level in Jupiter's atmosphere is based on solar abundance model of Lewis [1969]. However, if the Jovian atmosphere is reduced chemically, the water abundance could be very low as observed by Bjoraker [1985], or from the first analysis of Voyager I data by Drossart and Encrenaz [1982]. Such an environment may make the detection of water molecules more difficult. Finally, we note that, in the future, the Galileo atmospheric probe may be able to offer more detailed analysis of the chemical composition of the Jovian atmosphere.

Another possibility is that H_2O molecules react with CH_4 molecules in the plume of high temperature and the reaction produces CO molecules, since CO were detected in some infrared and millimeter telescopes. The preliminary observation of KAO shows that the mixing ratio of H_2O relative to CH_4 in the plume is 1000. This represents the H_2O content in the deep troposphere similar to the solar abundance, if the water originated from the deep atmosphere.

5.3 Was SL9 a Comet or Asteroid?

The main reason SL9 is considered cometary is that its fragments display cometary comae.

We infer that metallic ions observed [Noll et al., 1994] upon impact of SL9 on Jupiter are of cometary origin rather than atmospheric origin, since to date metallic ions are not detected at great concentrations in any substantial atmosphere on any planet or satellite. Metallic ions such as observed from SL9 are rather commonly observed upon impact of metallic projectiles onto various target materials. Since the calculated cometary to atmospheric mass ratio in the plumes is 1:40 [Takata et al., 1994], most of the gas in the plume is Jovian atmosphere. Therefore, an asteroidal origin of SL9 cannot be absolutely excluded. Moreover, the detection of H_2O from the G and K impacts [Bjoraker et al., 1994] could be explained by impact of a carbonaceous chondritic asteroid (carbonaceous chondrites contain $\sim$ 10% water). Moreover, any asteroidal type object is possible, since this might correspond to any meteorite type, except iron-nickel meteorites (since these contain no Mg^{++}). The lack of observing spectra from molecules or ionized species containing Si is not understood and would be expected if SL9 was either cometary or asteroidal. In conclusion, the spectral data are inclusive, and the only definition that SL9 is a comet is that it displayed a coma.

5.4 Possible Problems with Impact Modeling

We need to look back to the assumptions made in conducting impact modeling, in the event that the marginal detection of water is actually the result of only very shallow penetration of the SL9 fragments (to pressures less than $\sim$ 3 bars and altitudes greater than -40 km) such that they did not reach the water cloud deck at 3 to 10 bars and altitude of -30 to -40 km on Jupiter. Since emission spectra from compounds of sulfur are detected, and the source of the sulfur compounds is probably the Jovian atmosphere, it could be argued that fragments penetrated to less than the 3 bar pressure level. However, this argument is not supported by the plume cross-section shown in Fig. 4 which demonstrated that water ejecta remains in the interior of the opaque plume and is thus likely to be invisible to telescopic observation.

From the analysis of the plume size and the radiative signature, we conclude that the mass of the largest fragments are $\sim 2 \times 10^{15}$ g and have energies of 7.5×10^{28} ergs (for a density of 1 g/cm^3) corresponding to a diameter of $\sim$ 2 km. For any shape icy bodies with masses of $\sim 2 \times 10^{15}$ g upon impact on the Jovian atmosphere, all numerical simulations, both finite difference and SPH techniques, conducted by us, Zahnle and Mac Low [1994], and Boslough et al. [1994] indicate that penetration to pressure $\geq$ 10 bar always occurs. This pressure is approximately that which is equivalent to 100 m of water on the Earth. Moreover, recently, Field and Ferrara [1994] demonstrated that even if the SL9 fragments have an initial density (porous) as low as 0.2 g/cm^3, these become completely compressed by the dynamic pressure exerted via passage through the atmosphere when they reached the several bar level.

If the SL9 fragments did not reach the water cloud layer, it is conceivable the scenario outlined below can be constructed about the nature of the fragments.

The fragments may not each have been a single body, but a swarm of small bodies. For example, the fragment, Q, was originally observed to be a single object. After the repair of the HST, when better resolution was gained, it turns to be four separate objects. Approximately 25 fragments were detected using HST before the impact. The tidal break-up of SL9 could have produced 2^n fragments, in principle, rather than random number of fragments [Benz and Asphaug, 1994] where n is the arbitrary integer. Therefore, it is plausible that a large number of small objects, separated by distances of $\sim 10^2$ m, were produced but still observed as a single body from the Earth. If such an aggregation of small bodies, separated by distances greater than the order of the diameter of each body existed, each body penetrates separately into the Jovian atmosphere. Therefore, each object may have been too small to penetrate to the ~ 10 bar pressure level. For example, some 10^3 fragments of 10^2 m in diameter, spread out such that there was $\sim 10^2$ m of the space between objects, would not penetrate the water clouds. Such an array of objects may contain the same impact energy as 1 km - single solid impactor, and display the same photometric radiance prior to impact.

6. Conclusions

Upon impact of SL9 on Jupiter, the observed plume height (for the G impact) and radiative signature (for the R impact) are self consistent with individual fragments having impact energies lying between Weaver et al.'s determination ($\sim 10^{31}$ ergs) based on photometry [Weaver et al., 1994] and models based upon tidal break up ($\sim 10^{29}$ ergs) [Scotti and Melosh, 1993; Asphaug and Benz, 1994]. Fragment G is estimated to have the impact energy of $\sim 7 \times 10^{28}$ ergs upon the comparison of SPH simulations of plume height with HST images [Hammel, 1994]. The radiative signature at 10^2 seconds after the impact from SPH simulations are compared with IRTF spectral data taken at peak radiance some 4 minutes after impact [Orton et al., 1994]. The inferred impact energy of a fragment R obtained is 3.5×10^{28} erg. Upon adding up SL9 fragment masses (scaled by the G and R impactors) in the Weaver et al. [1994] catalog, the progenitor diameter of SL9 comet is estimated to be in the range 3.5 to 4.1 km and the total impact energy becomes $\sim 5 \times 10^{29}$ ergs. The lack of detection of water in the observed plumes is attributed to the geometry of the distribution of deep atmospheric constituents within the model plume. Moreover, the "water cloud layer" expected to exist in the Jovian atmosphere may actually have very little water as suggested earlier by Bjoraker [1985]. We conclude that deep penetration to ~ 300 km occurs for 2×10^{15} g (equivalent to 2 km diameter solid ice) SL9 fragments even if these are initially porous. However, if each of the 21 to 25 fragments were actually a cloud of 10^3, 10^2 m objects, separated by a 10^2 m or so, we would expect shallow penetration. However, we expect from the simulations of Asphaug and Benz [1994] such effectively super-porous SL9 fragments are gravitationally unstable, and we infer that a deep penetration model most easily fits all observations.

7. Acknowledgements

We thank Dr. A.P. Ingersoll for fruitful discussion. We thank all of the IRTF team members, Dr. H. Hammel, and HST team members for providing data and G. B. Field, and A. Ferrara for sharing their preprint with us.

References

Ahrens, T. J., T. Takata, J. D. O'Keefe, and G. S. Orton, 1994 (a). Impact of Comet Shoemaker-Levy 9 on Jupiter. *Geophys. Res. Lett.*, **21**, 1087-1090.

Ahrens, T. J., T. Takata, J. D. O'Keefe, and G. S. Orton, 1994 (b). Radiative Signatures from Impact of Comet Shoemaker-Levy-9 on Jupiter. *Geophys. Res. Lett.*, **21**, 1551-1553.

Asphaug E. and W. Benz, 1994, Density of Comet Shoemaker-Levy 9 Deduced by Modeling Breakup of the Parent Rubble-Pile. *Nature*, **370**, 120-124.

Belton, M. J. S., J. Veverka, P. Thomas, P. Helfenstein, D. Simonelli, C. Chapman, M. E. Davies, R. Greeley, R. Greenberg, J. Head, S. Murchie, K. Klaasen, T. V. Johnson, A. McEwen, D. Morrison, G. Neukum, F. Fanale, C. Anger, M. Carr, and C. Pilcher, 1992. Galileo Encounter with 951 Gaspra - 1st Pictures of an Asteroid. *Science*, **257**, 1647-1652.

Benz, W. and E. Asphaug, 1994. Shoemaker-Levy 9 and the Tidal Disruption of Comets. *Lunar. Planet. Sci. Conf. XXV abstract*, 101-102.

Bjoraker, G. L., The Gas Composition and Vertical Cloud Structure of Jupiter's Troposphere Derived from Five Micron Spectroscopic Observations, Doctor's thesis of Univ. of Arizona, 1985.

Bjoraker, G. L., T. Herter, S. Stolovy, G. Gull, and B. Pirger, 1994. IAU Circ. 6053.

Boslough, M. B., D. A. Crawford, A. C. Robinson, and T. G. Trucano, 1994. Watching for Fireballs on Jupiter. *EOS*, **75**, 305-310.

Carlson, B. E., A. A. Lacis, and W. B. Rossow, 1992. The Abundance and Distribution of Water Vapor in the Jovian Troposphere as Inferred from Voyager IRIS Observations, *Astrophys. J.*, **388**, 648-668.

Drossart, P. and T. Encrenaz, The abundance of Water on Jupiter from the Voyager IRIS Data at 5 μm, *ICARUS*, **52**, 483-491, 1982.

Field, G. B. and A. Ferrara, 1994. The Behavior of Fragments of Comet S-L 9 in the Atmosphere of Jupiter. *submitted to Astron. J.*.

Hammel, H. B., R. F. Beebe, A. P. Ingersoll, G. S. Orton, J. R. Mills, A. A. Simon, P. Chodas, J. T. Clarke, E. De Jong, T. E. Dowling, J. Harrington, L. F. Huber, E. Karkuschka, C. M. Santori, A. Toigo, D. Yeomans, and R. A. West, 1994. Hubble Space Telescope Imaging of Jupiter: Atmospheric Phenomena Created by the Impact of Comet Shoemaker-Levy 9. *submitted to Science.*

Lewis, J. S., 1969. The Clouds of Jupiter and the NH_3-H_2O and NH_3-H_2S Systems, *Icarus*, **10**, 365-378.

Mac Low, M. M. and K. Zahnle, 1994. Explosion of Comet Shoemaker - Levy 9 on Entry into the Jovian Atmosphere. *Nature* submitted.

Noll, K. S. M. McGrath, H. A. Weaver, S. Atreya, J. J. Caldwell, L. Trafton, and R. Yelle, 1994. *bulletin American Astron. Soc.*, **26**, 1059.

Orton, G. S., M. A'Hearn, and IRTF team, 1994. The NASA infrared telescope facility investigation of Comet Shoemaker-Levy 9 and its Collision with Jupiter: Preliminary results. *submitted to Science.*

Scotti, J. V. and H. J. Melosh, 1993. Tidal Breakup and Dispersion of P/Shoemaker-Levy 9: Estimate of Progenitor Size. *Nature*, **365**, 733-735.

Sekanina, Z. 1993. Disintegration Phenomena Expected During Collision of Comet Shoemaker - Levy 9 with Jupiter. *Science*, **262**, 382-387.

Takata, T., J. D. O'Keefe, T. J. Ahrens, and G. S. Orton, 1994. Comet Shoemaker-Levy 9: Impact on Jupiter and Plume Evolution. *Icarus*, **109**, 3-19.

Weaver, H. A., Feldman, P. D., A'Hearn, M. F., Arpigny, C., 1994. Hubble-Space Telescope Observations of Comet-P/Shoemaker-Levy 9 (1993e). *Science*, **263**, 787-791.

Wingate, C. A., N. Hoffman, and B. Stellingwerf, 1994. SPH Calculations of Comet

P/Shoemaker-Levy 9 Impact on Jupiter. *AAS meeting, abstract.*

Yeomans, D. K. and P. Chodas, 1993, IAU Circ., 5909.

Zahnle, K. and M. M. Mac Low, 1994. The Collision of Jupiter and Comet Shoemaker-Levy 9. *Icarus*, **108**, 1-17.

PAPER IV

Atmospheric Effects on Cratering on Venus

Atmospheric Effects on Cratering on Venus

Toshiko Takata, Thomas J. Ahrens

Division of Geological and Planetary Sciences
California Institute of Technology
Pasadena, California 91125

and

Roger J. Phillips

Department of Earth and Planetary Sciences
Washington University
St. Louis, Missouri 63130

submitted to *J. Geophys. Res.*

Abstract

A paraboloidal bow shock model was developed in order to estimate the surface distribution of gas shock-induced modifications surrounding venusian impact craters. We applied two-dimensional oblique shock dynamics to describe a three-dimensional paraboloidal - shaped bow shock impinging upon an assumed incompressible venusian surface. The effects of the hypersonic atmospheric shock acting on the venusian surface are considered in terms of maximum gas pressure, the density, the particle velocity, and the temperature, for varying angles and velocities of impact. The maximum boulder size that can be saltated by the shockwave induced gas flow and the degree of mutual collision of the surface materials are also considered. The present calculations quantitatively predict the areal extent of the gas shock perturbed surface for normal and oblique impact as a function of impact angle and velocity, and radii of impactors. For a 1 km-radius stony meteorite impacting at 20 km/s, the radius of the disturbed area extends $\sim$ 10-17 times the 3-5 km crater radius. The perturbed surface affects the surface radar properties and the present results can provide an explanation of the wide "dark/bright halos" surrounding some of venusian impact craters observed via Magellan imagery. For example, a $\sim$ 50 km radius bright halo within a $\sim$ 20 km dark halo is observed around the 3.1 km-radius crater located at 16.5° north latitude and 334.4° longitude. The average value of the radar backscatter cross section of the $\sim$ 20 km radius dark halo indicates that $\sim$ 50 cm-thick layer of porous lithologic material is superimposed upon the undisturbed surface. The occurrence of the bright halo indicates that the surface roughness in this region is $\sim$ 30% greater than that of the surrounding original surface. The present model can relate the observed crater halo radii to the impact parameters, such as impact velocity and angle, and the impactor radius.

1. Introduction

Venus has a dense atmosphere, whose pressure and density on the surface are 9.2 MPa and 65.0 kg/m^3, respectively [*Seiff*, 1983]. Among the terrestrial planets, this dense atmosphere is unique to Venus. Meteoroids upon transversing this atmosphere are affected by the resulting deceleration, ablation, deformation, and fragmentation. The atmosphere also affects impact ejecta emplacement and reduces the final crater dimensions relative to atmosphere-free planets [*Melosh*, 1989]. If there is no significant deceleration, incident meteoroids would impact the venusian surface with hypersonic velocity. During atmospheric transit, an atmospheric shock front forms. The shock wave driven by the meteoroids impinges on the venusian surface. As a result, features normally associated with impact cratering on atmosphere-free planets are modified in the case of impact cratering on Venus. Upon interpreting the Venera radar imaging, Ivanov [1986] conducted the first estimates of the effect of the gas shock. They explained qualitatively and approximately estimated the magnitude of shock interactions with the surface using the results of analog high-explosive experiments.

Magellan radar backscatter data revealed that some craters are surrounded by "dark halos" which have low radar backscatter cross-sections, and that these features are unique to Venus [*Phillips et al.*, 1991] (Figure 1). The halo in Figure 1 (d) has no crater, but still has the same features as other craters. Some of the dark halos are themselves accompanied by surrounding bright halos, as in Figure 1 (a), (b), and (d). In the case of oblique impact, the dark halos seem to elongate up-range of the impact craters whereas the continuous ejecta pattern extends preferentially down-range.

The variation of the backscatter cross section at constant radar incident angle around craters is explained by either the difference of the surface roughness, variation in the porosity of the surface materials, or the variation in lithology. A region of lower backscatter cross section, compared to the surrounding region, will occur when

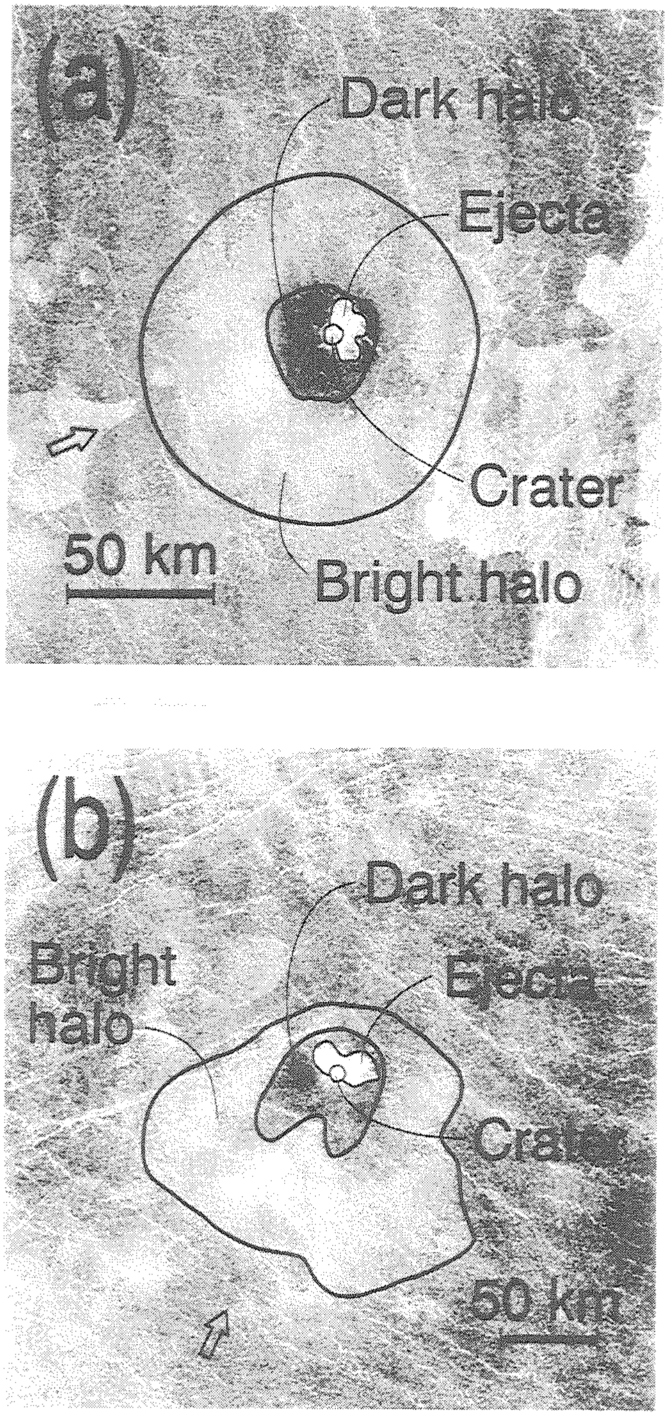

Figure 1. Magellan images of craters that have wide dark or bright halo features. (a) Unnamed crater, mean diameter 6.1 km, at 16.5°N and 334.4°E. (b) Unnamed crater, mean diameter 8.0 km, at 11.9°N and 352°E. (c) Unnamed crater, mean diameter 11 km, at 9.3°N and 358°E. (d) Bright and dark halo without crater, at 8.7°N and 333.5°E.

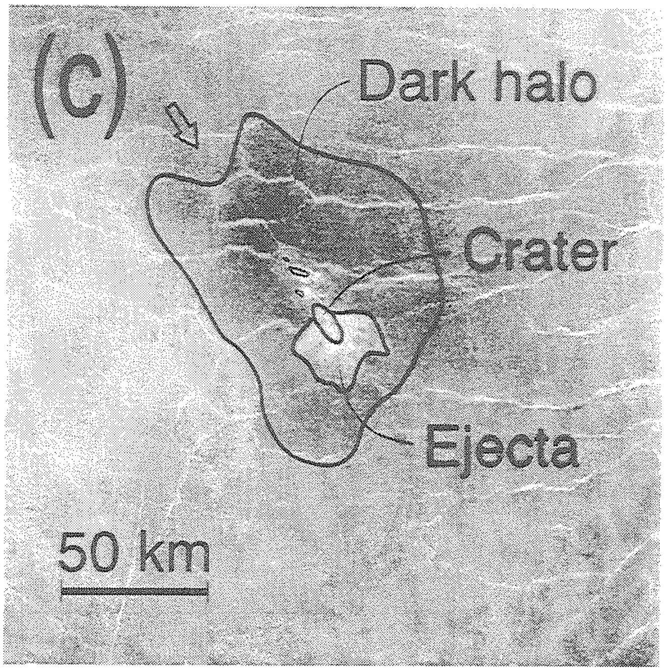
(c)
Dark halo
Crater
Ejecta
50 km

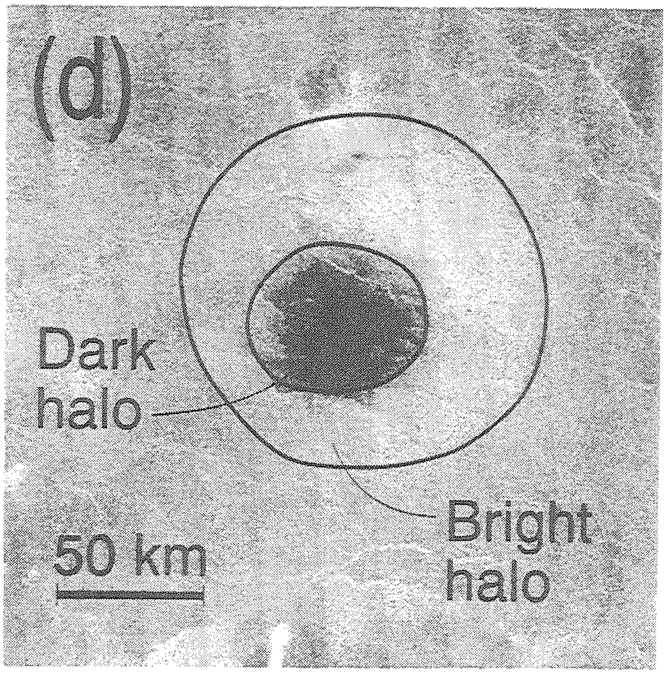
(d)
Dark halo
Bright halo
50 km

the surface is smoother than its surroundings. Another interpretation is that it is more porous than the original planetary surface. In contrast, an area with brighter backscatter cross-sections indicates that surface is rough at the scale of the Magellan radar wavelength (12.6 cm). The Pioneer Venus radar reflectivity data showed that a smooth appearing surface is dominated by bedrock or densely packed debris, and that the thickness of a fine grained regolith cover should be less than tens of centimeters thick [*Arvidson et al.*, 1991]. We also note that Venera 13 and 14 landing sites imaging data showed slab-like rocks and rock fragments with dimensions of several centimeters to several tens of centimeters [*Florenskiy et al.*, 1983]. Therefore, the modification of the radar properties as a result of impact cratering must overprint these features of the original surface. *Phillips et al.* [1991] suggested that "dark halos" originate from either the effect of impact of the atmospheric shock wave that trails the meteoroid, or represent a deposit of the fine material produced by the ablation of the meteoroid in the atmosphere. Zahnle [1992] assumed small bolides exploded in the atmosphere and approximated the expansion of the atmospheric shock wave with spherical blast wave model. Then peak gas shock pressures on the planetary surface are calculated. In his work, dark and bright halos are explained by the difference of sizes of the broken rocks.

Impact cratering on a planet with an atmosphere taken place in several stages: (a) the incoming meteoroids interact with the surrounding atmosphere producing a bow shock, (b) The shocked gas interacts with the planetary surface and surface materials are entrained in the atmosphere, (c) the meteoroids impact the solid planet and the surface experiences the compressive and rarefaction phases. Then vapor clouds expand as ejecta are launched. Planetary surfaces surrounding craters are modified by the passage of the initial bow shock wave, and the following explosive vapor cloud. The fireball expands symmetrically regardless of the obliqueness, whereas bow shock waves accompanying meteoroids largely depend on the obliqueness of impact. Since the dependence on obliqueness is the unique feature of halos, the interaction of bow shock waves with planetary surfaces can, in principal, explain the feature. Therefore, in this paper, the bow shock interaction of stage (b) is investigated.

A bow shock model is developed in this paper in order to quantify the effects of the hypersonic atmospheric shock accompanying with the oblique impact on the planetary surface. The related flow properties, such as maximum gas pressure and gas tangential shear flow velocity are calculated. The oblique shock dynamics is applied to the three-dimensional paraboloidal bow shock front interacting with an incompressible rigid half-space to understand the interaction of the gas shock with the planetary surface. Then the magnitude of the surface disturbance is estimated from the model. Finally, we evaluate how the bow shock model applies to the crater radar data, and how these data may be used to estimate impact parameters associated with a given crater.

2. Bow Shock Model and Shock Physics

2.1 Bow shock formation

When a hypervelocity meteoroid encounters an atmosphere, a shock front forms around the meteoroid and induces a compressed gas layer between the shock front and the meteoroid [*Bronshten*, 1983] (Figure 2 (a)). In addition, a bow shock wave and a wake develop behind the body and expand toward the incoming direction [*Martin*, 1966].

In the case of a meteoroid passing through an atmosphere with high Mach number, M, (ratio of shock velocity to local atmospheric sound speed) and with the corresponding low value of γ (the ratio of the specific heat at constant pressure relative to that at constant volume), the compressed gas layer becomes very narrow compared

(a)

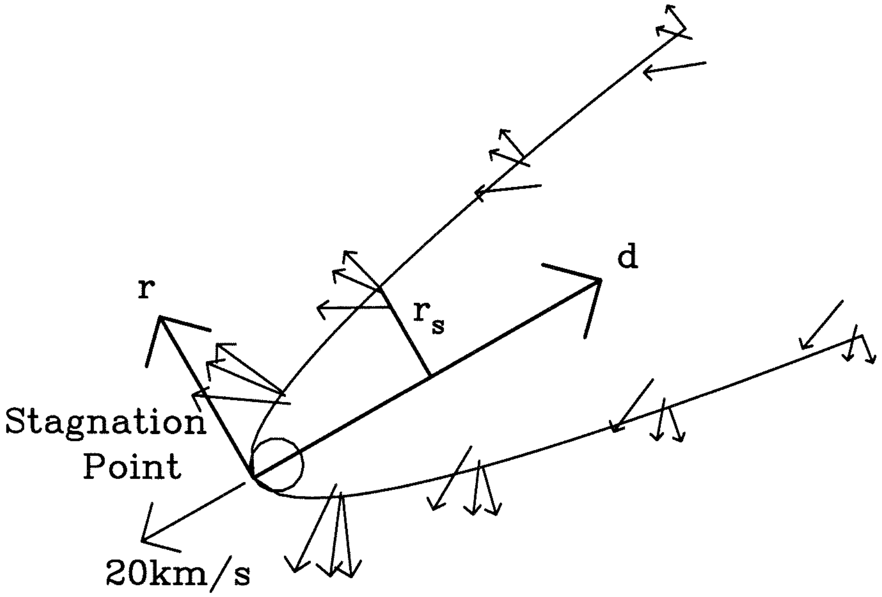

Figure 2. Gas flow and the corresponding shock parameters inside of a bow shock. (a) The bow shock shape calculated from the symmetric power law (Eq. 2) and corresponding gas flow velocity. **r** is the distance of the bow shock front from the trajectory of the meteoroid and **d** is the distance along the trajectory from the tip of the meteoroid. The meteoroid is traveling with the velocity of 20 km/s in this case. The arrows represent the velocity of the gas at each position of the space in the reference frame of the stationary planetary surface. (b) Shock parameters, such as atmospheric density, pressure, and gas velocity inside of the bow shock, normalized by these shock parameters at the shock front, r_s, are calculated from the symmetric power law (Eqs. (A1-1) - (A1-3)) in the case of the steady flow.

to the size of the body. Assuming that the body is a sphere, and that $M > 2$, the thickness, Δ_s, of the compressed layer, that is, the distance between the shock front and the body at the stagnation point, is expressed as

$$\Delta_s/R \sim 2/[3(\rho/\rho_0 - 1)] \sim (\gamma - 1)/3 \tag{1}$$

(b)

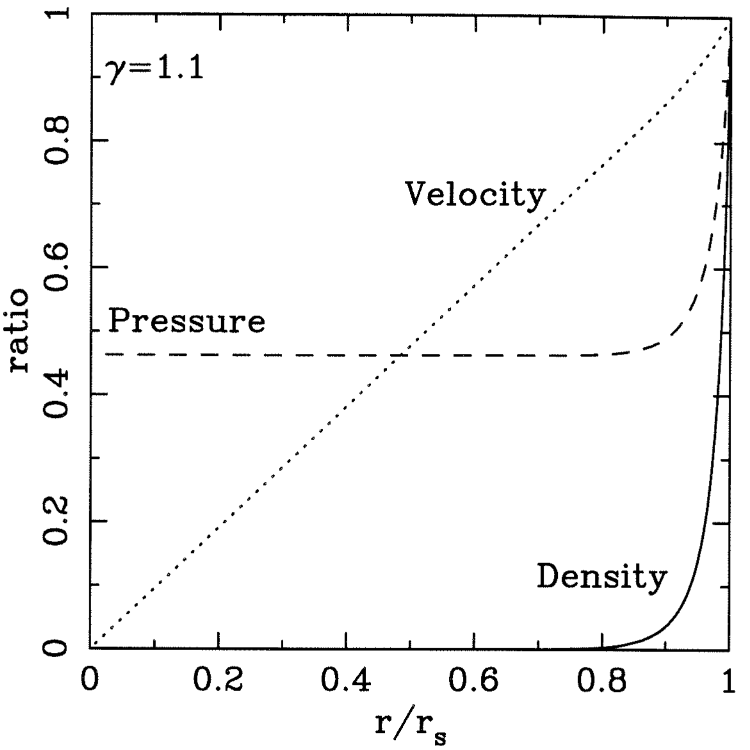

where R is the radius of the body, ρ is the atmospheric density of the shocked state and ρ_0 is the atmospheric density of the ambient state [eq. 5-2, *Martin*, 1966]. Δ_s/R becomes 0.07 for $\gamma = 1.2$, and 0.03 for $\gamma = 1.1$. Since the effective value of γ tends to unity at higher M, Δ_s/R approaches zero and the shock front gets close and tangent to the body at the stagnation point when $M \gg 1$ [*Hayes and Probstein*, 1966, p. 420].

Thus, the shock front has the same local curvature as the meteoroid on the stagnation point, and the shape of the bow shock wave approaches a paraboloidal surface. The normal distance of the bow shock wave from the trajectory of the meteoroid, r, is the function of the distance from the tip of the body along the trajectory, d, as shown in Figure 2 (a) [*Martin*, 1966];

$$r/R \sim (2d/R)^{\frac{1}{2}} \tag{2}$$

The motion in gas flow behind the bow shock can be calculated using a similarity solution for an inviscid axisymmetric expanding wake [Zel'dovich and Raizer, 1966]. This is shown in Figure 2(a) [Hornung, 1967]. In Figure 2(a), the meteoroid is moving at 20 km/s. The arrows represent the particle velocity in the gas flow in the reference frame of the stationary planetary surface. The ratio of the gas velocity, pressure, and density at the wake position (r) relative to those right behind the shock front (r_s) at the same travel distance from the stagnation point (d), v/v_s, p/p_s, and ρ/ρ_s, respectively, are calculated as a function of normalized wake distance r/r_s (Figure 2 (b)). Here, the subscript of s indicates the value behind the shock front. In this calculation, $\gamma = 1.1$ is assumed. The gas is compressed toward the region close to the shock front (figure 2(b)). If γ increases, the pressure and density curves, such as those in Figure 2 (b), fall off less rapidly.

2.2 Bow shock model

Assuming that the body retains a spherical curvature at the front during its traverse through the venusian atmosphere, the meteoroid is accompanied by the bow shock wave whose shape remains constant and is given by Eq. (2). The particle velocity of the gas at the shock front is normal to the shock front, as shown in Figure 2 (a). The gas enveloped by the shock subsequently expands forward and away from the trail of the meteoroid. The paraboloidal bow shock continues to propagate away from the trajectory, and it interacts with the planetary surface, as sketched in Figure 3 (a). In the reference frame of the surface at rest, the shock wave propagates away from the center of the crater. The propagation and reflection of the shock wave at around the contact point of shock wave on the planetary surface is analogous to the case of spherically expanding blast wave interacting with the surface [*Heilig*, 1985; *Brode*, 1968] (Figure 3 (c)). However, in the case of oblique impacts, the trajectory of the blast shock wave trailing to the meteoroid is also inclined toward the surface, and the blast wave interacts with the up-range surface at an earlier point in time than the impact of the meteoroid (Figure 3 (b)). Therefore, a different interaction from that of a spherical explosion is expected, and a paraboloidal bow shock represents shock interaction with planetary surface in the case of oblique impact.

To quantify the position of the paraboloidal bow shock front as a function of time, we employ a coordinate system to define the surface position, X and Y, and vertical elevation, Z. We assume that the meteoroid trajectory lies in the X-Z plane. Here Φ is the angle of the trajectory from the horizon [Figure 4(a)]. The unit of length is normalized to the radius of a meteoroid, R. We express the bow shock surface as $f = 0$, where f is

$$f = (\frac{Y}{R})^2 + (\cos\Phi \cdot \frac{Z}{R} - \sin\Phi \cdot \frac{X}{R})^2 - [2(\cos\Phi \cdot \frac{X}{R} + \sin\Phi \cdot \frac{Z}{R} - \frac{X_0}{R})]^{2n} \quad (3-1)$$

Here, $X_0 = X_r - V_i t$, X_r is an arbitrary reference distance at $t = 0$, V_i is the impact velocity of the meteoroid along its trajectory, $\vec{V_i} = (-V_i \cos\Phi, 0, -V_i \sin\Phi)$, and $n = \frac{1}{2}$ for a paraboloid.

For some values of Φ, Eq. (3-1) cannot be applied for $X \leq 0$, since the shock front expressed by Eq. (3-1) at these points is inclined toward the incoming direction on the planetary surface, and thus Eq. (3-1) is no longer appropriate for the propagating shock. However, when the meteoroid impacts the surface, the atmospheric gas is compressed between a meteoroid and the surface. The compressed atmospheric gas on the impact site can be explosively released cylindrically [O'Keefe and Ahrens, 1988]. Therefore, we assume that the shock front propagates cylindrically along the planetary surface in the down-range direction in the same way as the case of normal impact. Then, for the oblique impact, instead of Eq. (3-1), in the region of $X < 0$

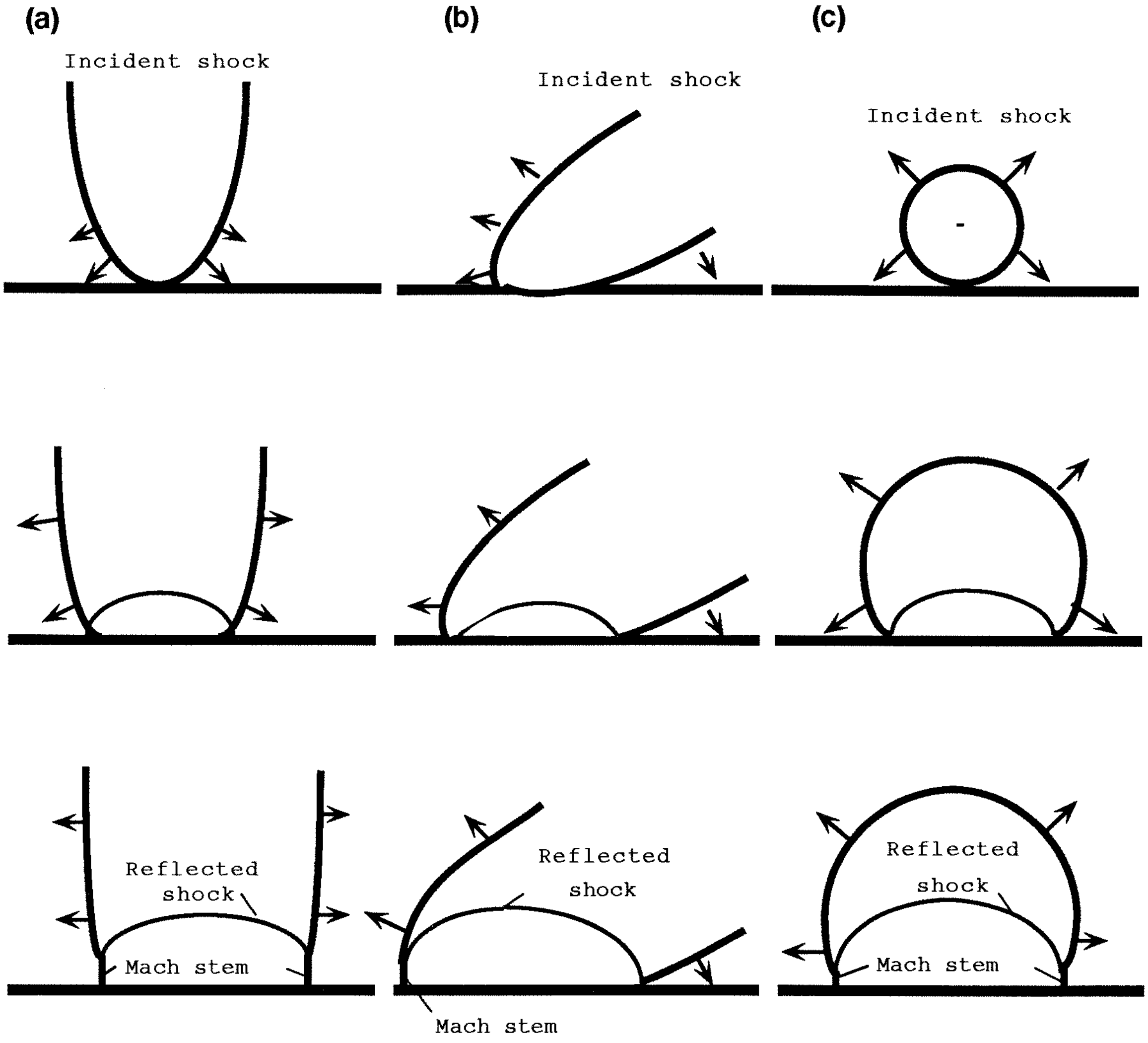

Figure 3. The sketch of the propagation and the interaction with the planetary surface of various shock expansion models. (a) a bow shock wave for the normal impact. (b) a bow shock wave for the oblique impact. (c) for comparison, a spherical blast wave from an atmospheric explosion.

and $-X/Z < \tan\Phi$, we use

$$f = (\frac{Y}{R})^2 + (\frac{X}{R})^2 - [2(\frac{Z}{R} - \frac{X_0}{R})]^{2n} \qquad (3-2)$$

Then the propagation of the shock wave on the surface is similar to that of normal impact (Z=0 in Eq. (3-2) corresponds to Z=0 and $\Phi = 90°$ in Eq. (3-1)), and Eq.

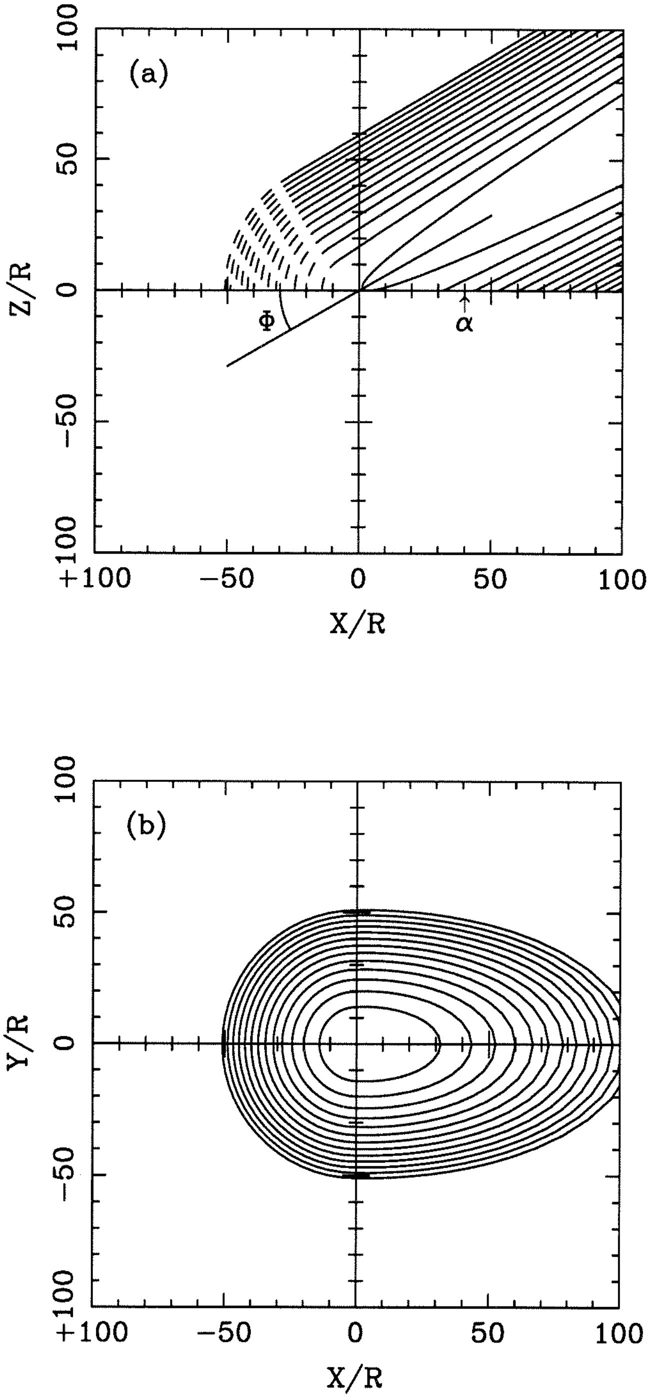

Figure 4. Time varying position of propagating bow shock front. (a) vertical cross section, (b) footprint on the ground, for $\Phi = 30°$ with a time interval of normalized time of $100R/V_i$. In Eqs. (3-1) and (3-2) the condition of $Y = 0$ corresponds to the propagating blast wave in Figure 2 (a) and the dotted line expresses the position applied by Eq. (3-2). The coordinate is normalized by the meteoroid radius R and the center of the meteoroid passes through the origin of the coordinate system.

(3-1) and Eq. (3-2) are continuous at $X/Z = \tan\Phi$. Figure 4 shows the time varying position of the propagating bow shock front in a vertical cross section (a) and ground foot print (b), in the case of $\Phi = 30°$, with time intervals equal to $100R/V_i$. The position of the bow shock front in a vertical cross section is expressed as $f(t, Y = 0) = 0$ (corresponding to (a)), and the position of the shock front on the surface (corresponding to (b)) can be expressed as $f(t, Z = 0) = 0$ in Eq. (3-1) and Eq. (3-2). The shock fronts defined by Eq. (3-2) are plotted with dashed lines in Figure 4 (a).

The horizontal propagation velocity of the shock front on the planetary surface, q_1, Mach number of M_1, and shock angle, that is, the inclination angle of the shock front from the ground surface, α, are calculated from Eqs. (3-1) and (3-2) at each point on the planetary surface as

$$q_1 = c_1 M_1 = \frac{1}{\sin\alpha}(\vec{V_i} \cdot \frac{\nabla f}{|\nabla f|}) \tag{4}$$

and

$$\sin\alpha = \sqrt{f_x^2 + f_y^2} \tag{5}$$

where c_1 is the sound velocity of the ambient state, and we define $\nabla f/|\nabla f| = (f_x, f_y, f_z)$.

To relate the paraboloidal bow shock to cylindrical and spherical atmospheric blast wave, we will compare the position of the propagating shock wave for these cases. In the case of the normal impact of the meteoroid ($\Phi = 90°$), from Eq. (3-1) and (3-2), the distance of the shock front on the planetary surface (Z=0) from the center of the impact as a function of time, $r_b(t)$, can be written as

$$\frac{r_b(t)}{R} = k_b(\frac{V_i t}{R})^{\frac{1}{2}} \tag{6}$$

where k_b is $\sqrt{2}$. In the case of the strong spherical blast wave, the distance of the shock front from the point of the explosion, $r_{sp}(t)$, becomes

$$\frac{r_{sp}(t)}{R} = k(\frac{E}{\rho})^{\frac{1}{5}} t^{\frac{2}{5}} \simeq k(\frac{2\varepsilon\rho_m}{\rho})^{\frac{1}{5}}(\frac{V_i t}{R})^{\frac{2}{5}} \sim k_s(\frac{V_i t}{R})^{\frac{2}{5}} \tag{7}$$

where k is a coefficient, equal to approximately unity (0.8 for γ=1.1 and 0.9 for γ =1.2) and E is the total energy of the explosion [*Zel'dovich and Raizer*, p. 99, 1965]. Here, we use the kinetic energy of the meteoroid for the explosive energy, E, with the coefficient of the efficiency of the conversion from the kinetic energy of the meteoroid to the explosive energy of the gas, $\varepsilon(\leq 1)$, where $E = \frac{\varepsilon}{2}\frac{4\pi}{3}R^3\rho_m V_i^2$, ρ_m is the density of the meteoroid, and k_s is the coefficient of $\simeq k(\frac{2\varepsilon\rho_m}{\rho})^{\frac{1}{5}}$. In the case of a cylindrical blast wave produced by one point source, the distance of the shock front from the explosive point, $r_c(t)$, becomes

$$\frac{r_c(t)}{R} = \sqrt{2}k'(\frac{E}{\rho})^{\frac{1}{4}}t^{\frac{1}{2}} \simeq k'(\frac{8\varepsilon\rho_m}{\rho}R)^{\frac{1}{4}}(\frac{V_i t}{R})^{\frac{1}{2}} \sim k_c(\frac{V_i t}{R})^{\frac{1}{2}} \tag{8}$$

k' is another coefficient whose magnitude is approximate unity [*Sakurai*, p. 348, 1968]. k_c becomes $\sim R^{\frac{1}{4}}$ at $\varepsilon = 0.01$, and $\sim 4R^{\frac{1}{4}}$ at $\varepsilon = 1$, assuming that $\rho_m = 2700\text{kg/m}^3$.

The ratio between the radii of propagating paraboloidal bow shock and that of the spherical explosion is

$$r_b(t)/r_{sp}(t) \sim (k_b/k_s)(V_i t/R)^{-0.1} \tag{9}$$

Since k_b/k_s is approximate unity, the difference of two models depends in detail on impact parameters. Similarly, the ratio between the radii of propagating bow shock and that of the cylindrical explosion is described by:

$$r_b(t)/r_c(t) \sim k_b/k_c \sim R^{-\frac{1}{4}} \tag{10}$$

Both (9) and (10) show that these ratios are on the order of unity, that is the paraboloidal bow shock is analogous to an atmospheric blast wave. Since Eq. (3-1) and (3-2), or corresponding Eq. (6) described essentially a cylindrical blast wave, the paraboloidal bow shock model can be treated as the cylindrical blast wave, by taking into account oblique impact.

2.3 Reflection shock wave

Next, we will examine the atmospheric shock state via the interaction with the surface. In the case of a strong surface explosion (e.g., nuclear), a thermal precursor in the atmosphere occurs because underground shock initially outruns the atmospheric shock and subsequently pre-heats the atmosphere immediately above the ground. The main atmospheric shock is also reflected from the surface, and the reflected shock is also transmitted backward from the incident shock front on the ground surface [*Brode*, Fig. 15, 1968]. The nature of the gas shock reflection also changes as the atmospheric shock front propagates away from the center of the explosion. The effect of the shock reflection following the incident shock is comparable to the incident shock. For example, the ratio of the pressure behind the reflected shock to the pressure in front of the reflected shock (or behind the incident shock), p_3/p_2, is $\sim (3\gamma-1)/(\gamma-1)$ in the case of a tangential shock when the ratio of the pressure behind incident shock to that of the ambient pressure is $p_2/p_1 \gg 1$. Then p_3/p_2 becomes 13, for $\gamma = 1.2$, and 26, for $\gamma = 1.1$ [*Courant and Friedrichs*, p. 153, 1948]. Here, the subscript 1 indicates the ambient state, and the subscript 2 indicates the pressure behind the incident shock, whereas the subscript 3 indicates the pressure behind the reflected shock [figure 5]. Thus, more than one order magnitude difference can be observed in the pressure behind the reflection shock and it is essential to take into account the effects of shock reflection, in order to estimate the actual shock properties at the contact points of shock wave on the planetary surface and the magnitude of the disturbance on the surface. The effect of enhanced pressure by shock reflection wave was discussed in Brackett and McKinnon [1992]. However, geometrical application of oblique impacts has not been previously taken into account.

For constant γ, the configuration of the reflected shock and the state behind the shock (pressure, density, temperature, and particle velocity) can be estimated from the horizontal component of the shock front propagation velocity, q_1, in Eq. (4), and from the angle of the shock front, α, using the conservation equations for oblique shocks (Appendix 2 [*Hornung*, 1986]).

We summarize the configurations of shock reflection in Figure 5 [from *Hornung*, 1986]. When the value of the properties within two of the shocked regions (as depicted in Figure 5) are the same, we use the lowest value of appropriate subscript. Here, the velocity of the gas flow is expressed in the frame of reference of the stationary shock front. When M_1 is less than $(\sin\alpha)^{-1}$, a shock does not form and the flow becomes subsonic, and when the gas velocity behind the incident shock $M_2(= q_2/c_2)$ is < 1, the reflected shock is diffusive, and the inclination of the incident shock front becomes gradually perpendicular to the surface (we denote this case as "no reflection").

Two other types of shock reflection exist. Regular reflection is shown in Figure 5 (a). Mach reflection is shown in Figure 5 (b). In the latter case, the intersection of the incident and reflected shock does not contact the planetary surface, and a Mach stem is developed [*Hornung*, 1986].

The calculated shock reflection types, as a function of α and M_1 in the case of $\gamma = 1.1$, are shown in Figure 6 (a). The regions are divided by the types of no reflection (diffusive reflection), Mach reflection, regular reflection, and subsonic region (unhatched region in the figure). In order to see the effect of varying the value of γ, we plotted the post shock pressure for $\gamma = 1.1$(solid line) and $\gamma = 1.2$ (dotted line) in Figure 6 (b). The discontinuity of the isobar around $\alpha \sim 45°$ in this figure is caused by the change of the reflection type (the boundary between regular reflection and Mach reflection). If γ becomes smaller, the regular reflection occurs at greater α. If the type of reflection is regular, the difference of the pressure between $\gamma = 1.1$ and $\gamma = 1.2$ becomes about a factor of two at high Mach numbers. We will discuss the selection of the effective γ for shocked CO_2 gas in the next section.

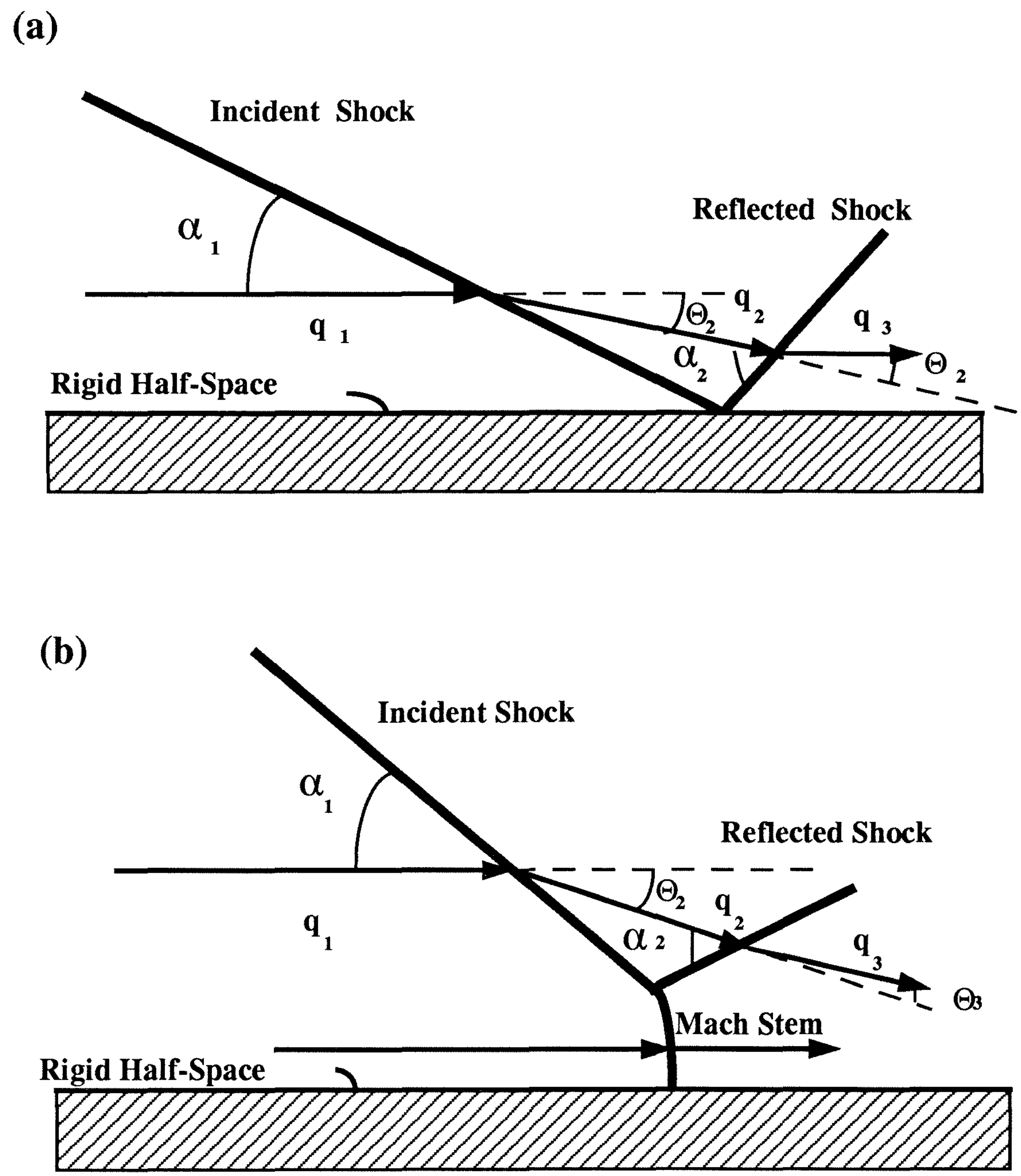

Figure 5. Sketch of (a) regular reflection and (b) Mach reflection. (a) The initial gas flow and final flow are the same direction in the case of regular reflection. The intersection of the initial and reflected shock front is on an assumed rigid planetary surface. (b) Impact angle α is large enough for the intersection of incident shock front and reflected front to detach as Mach stem from the ground (from *Hornung*, 1986).

(a)

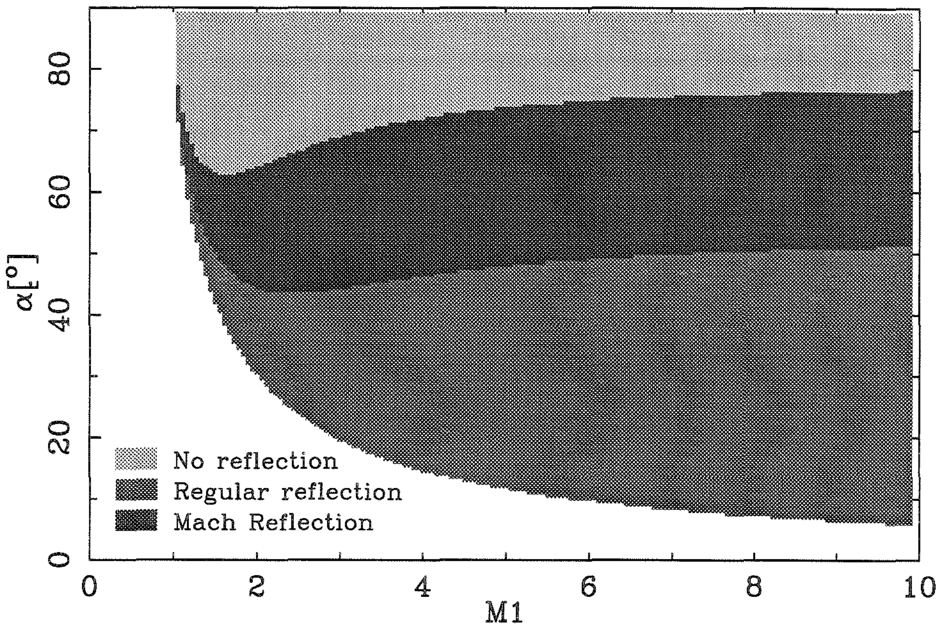

Figure 6. Reflection type and shock pressure as functions of impact angle and impact velocity. (a) Simulated shock configurations for given impact angle α and the propagation speed in the Mach number, M_1, in the case of $\gamma = 1.1$. The various regions represent shock reflection types. (b) Comparison of pressure profiles for the case $\gamma = 1.1$ and 1.2.

In these calculations, we assume that the flow of the gas in front of and behind the shock front is pseudo-steady inviscid flow of a perfect gas in the thermal equilibrium. The pseudo-steady flow means that the shock wave is assumed to propagate into a stationary gas in an inertial frame with the speed of $q_s (= q_1 \sin \alpha)$, and this can be treated as the steady flow of the horizontal velocity of q_1 with the stationary shock front on the surface. The difference between pseudo-steady flow and a steady flow is that the transition from the regular reflection to the Mach reflection occurs at higher α in the case of the pseudo-steady flow [*Hornung*, 1986].

Because we approximate the gas flow to be inviscid and the planetary surface

(b)

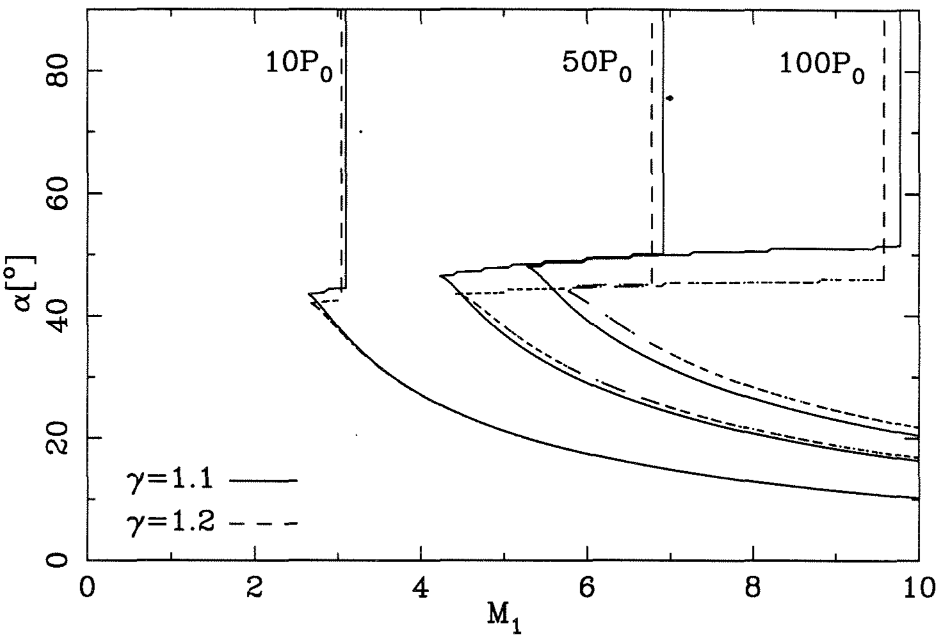

to be incompressible, we neglect the shear stress on the surface and the heat flux from (or to) the surface. These effects thicken the viscous boundary layer, and cause the transition from the regular reflection to Mach reflection to occur at higher shock angles of interactions [*Hornung*, 1986]. This suggests that the boundary effect causes much higher shock pressures and densities in the extended range of the regular reflection. Conversely, the porosity and roughness of the surface attenuate the reflected shock wave. Thus, the calculation of the shocked state can be more complicated on a real planetary surface.

3. Results

3.1 Results of the paraboloidal bow shock model

In this section, we will examine shock induced gas properties on the surface caused by oblique impact of a meteoroid, such as maximum pressure, $P(X,Y)$, maximum density, $\rho_s(X,Y)$, maximum horizontal gas velocity, $U(X,Y)$, and maximum temperature, $T(X,Y)$, using paraboloidal bow shock model taking into account reflection shock waves.

Before discussing the effects of the gas shock, we calculate the expected crater radius, R_c, for impacts on Venus. The scaling law of Schmidt [1980] is employed, for craters in dry sand which neglects the effect of atmospheric pressure, and the transient radius of the crater, R_{ct}, is,

$$\frac{R_{ct}}{R} = 0.7(\frac{gR}{V_i^2 \sin^2 \Phi})^{-0.16}(\frac{4\pi}{3}\frac{\rho_m}{\rho_t})^{1/3} \tag{11}$$

where g is Venus gravity ($\simeq$ 8.8 m/s^2), and we assume a density of the target and the ejecta, ρ_t, of 2800 kg/m^3, and that of the meteoroid, ρ_m, respectively. The radius of the final crater, R_c, becomes $\sim 1.19 R_{ct}$ [*Melosh*, p.129, 1989]. Here, obliquity reduces the size of the crater from that of normal impact [*personal communication with Schmidt*].

The resulting shock-induced gas states at the venusian surface are shown in the case of impact of a stony object at velocity, V_i, of 20 km/s, with radius, R, of 1 km, and impact angle of $\Phi = 60°$ in Figure 7-1, $\Phi = 45°$ in Figure 7-2, $\Phi = 30°$ in Figure 7-3, and $\Phi = 15°$ in Figure 7-4. The crater size, R_c, calculated from eq.(11) with $\rho_m = 10^3$ kg/m^3 varies from $5.4R$ to $3.6R$, as Φ becomes from 90° to 15°. In these figures, the crater size, $R_c \sim 5R$, is shown as a dotted circle.

Figure 7-1 (a) - 7-4 (a) demonstrate the characteristics of the shock reflection corresponding to the bow shock model. The flow is subsonic in the unhatched region. Since the shock reflection process is non-linear, the spatial distribution of different reflection modes as a function of impact angle can be observed. The lower the value of Φ becomes, the smaller the area of regular reflection, and the greater the surface area which is exposed to a Mach reflection in the up-range area. In the down-range region, or in the case of normal impact, no reflection occurs except at the center of

Figure 7-1.

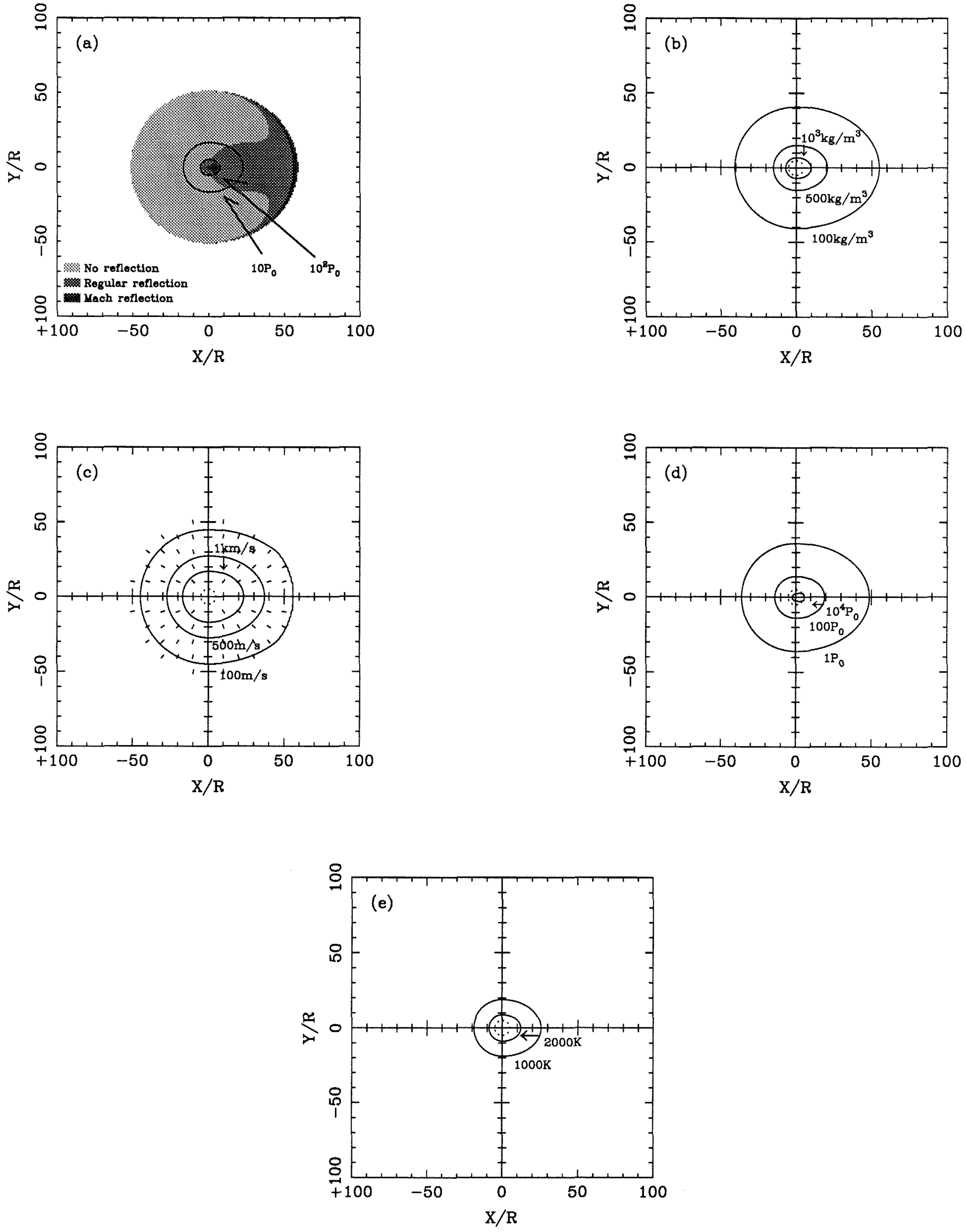
(a)
Y/R
X/R
100
50
0
−50
100
+100
−50
0
50
100
▒ No reflection
▓ Regular reflection
█ Mach reflection
$10P_0$
10^2P_0
(b)
10^3kg/m^3
500kg/m^3
100kg/m^3
(c)
1km/s
500m/s
100m/s
(d)
10^4P_0
$100P_0$
$1P_0$
(e)
2000K
1000K

Figure 7-2.

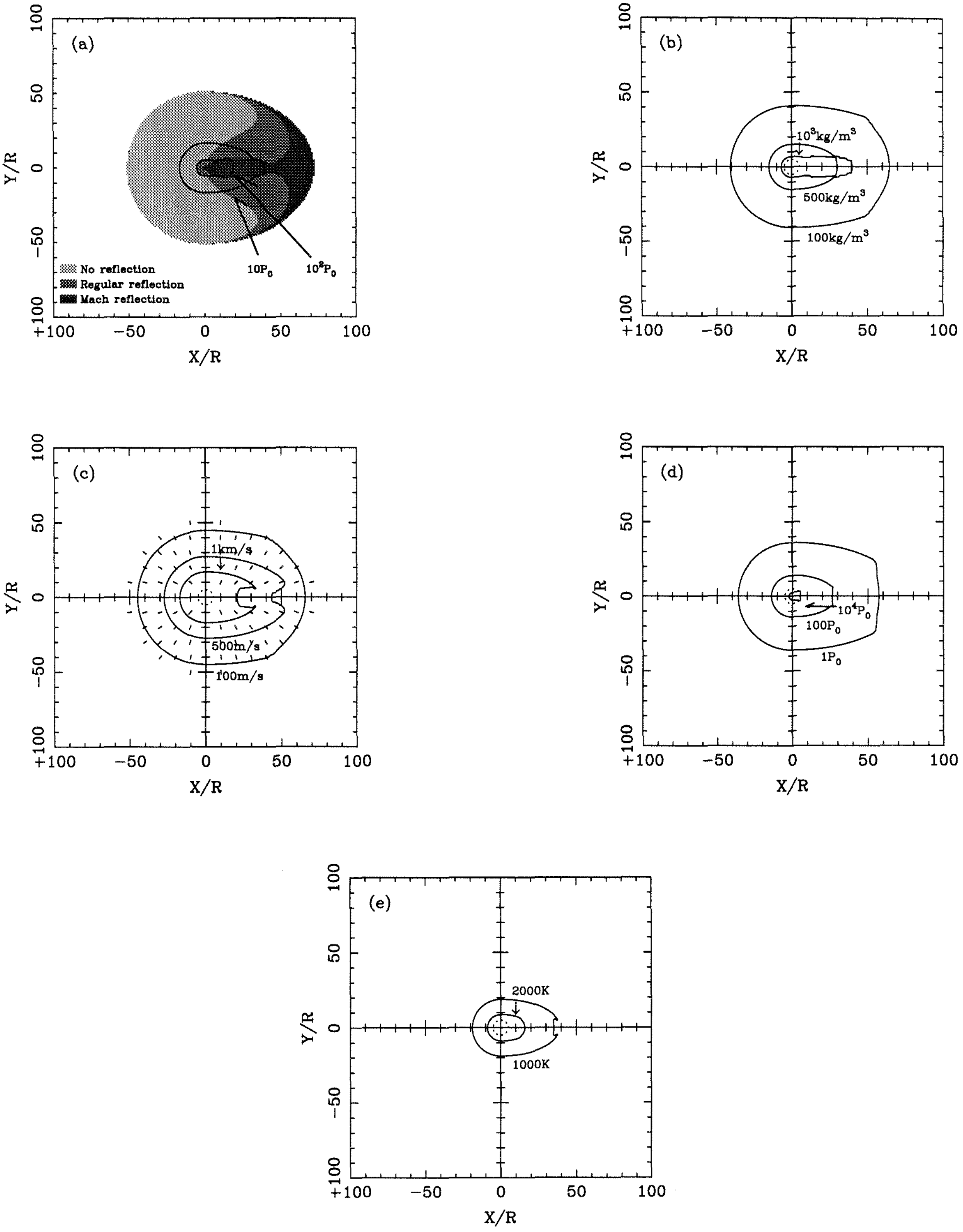
(a)
No reflection
Regular reflection
Mach reflection
10P₀
10²P₀
(b)
10³kg/m³
500kg/m³
100kg/m³
(c)
1km/s
500m/s
100m/s
(d)
10⁴P₀
100P₀
1P₀
(e)
2000K
1000K
Y/R
X/R
100
50
0
−50
−100
+100

Figure 7-3.

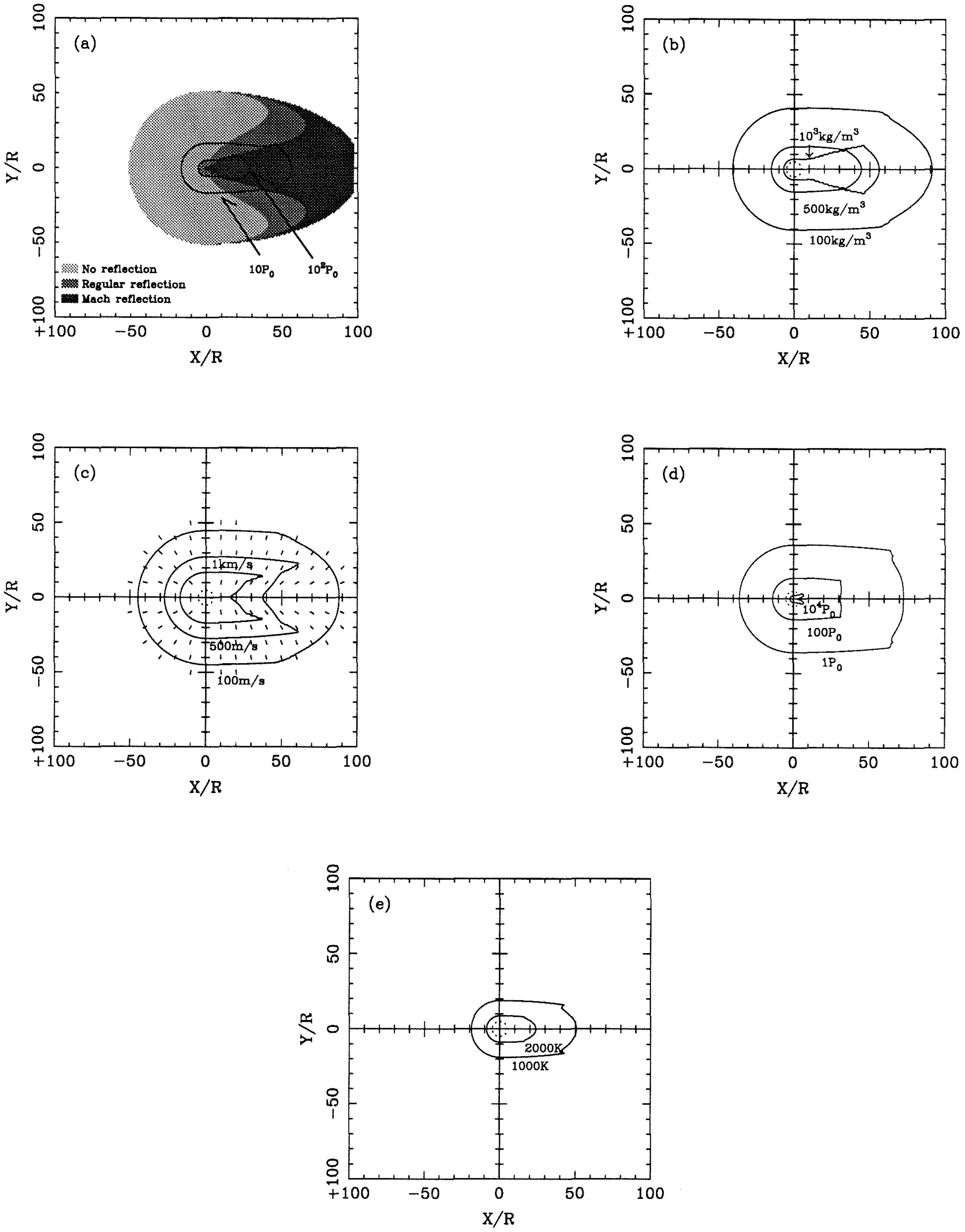
(a)
▨ No reflection
▨ Regular reflection
■ Mach reflection
$10P_0$
10^2P_0
(b)
10^3kg/m^3
500kg/m^3
100kg/m^3
(c)
1km/s
500m/s
100m/s
(d)
10^4P_0
$100P_0$
$1P_0$
(e)
2000K
1000K
Y/R
X/R
100
50
0
−50
−100
+100
−50
0
50
100

Figure 7-4.

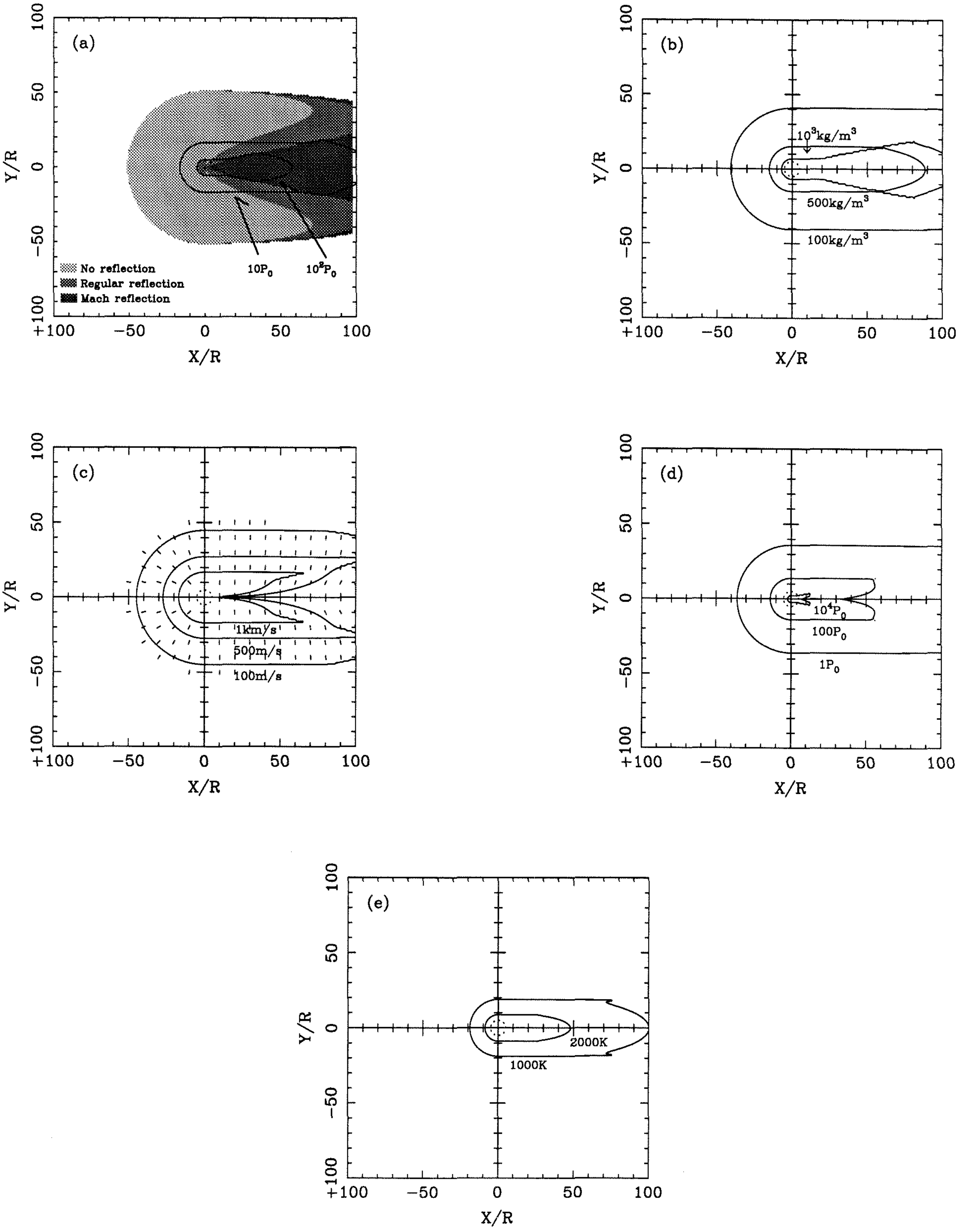
(a)
No reflection
Regular reflection
Mach reflection
$10P_0$
10^2P_0
(b)
10^3kg/m^3
500kg/m^3
100kg/m^3
(c)
1km/s
500m/s
100m/s
(d)
10^4P_0
$100P_0$
$1P_0$
(e)
2000K
1000K
Y/R
X/R
100
50
0
-50
-100

Figure 7. Maps of shock properties for oblique impact on Venus in the case of the impact velocity of meteoroid $V_i = 20$ km/s. The impact angle is $\Phi = 60°$ in 7-1, $\Phi = 45°$ in 7-2, $\Phi = 30°$ in 7-3, and $\Phi = 15°$ in 7-4. Coordinate system is the same as that of Figure 4. The dotted circles in all figures represent the crater size in the case of impact by a 1 km radius meteoroid. (a) Shock reflection types and maximum shock pressure. The representation of reflection types is the same as Figure 4. Isobars are normalized by venusian surface pressure, P_0 of 9.2 MPa. (b) Maximum shock density. (c) Maximum horizontal gas velocity induced by shock wave. Small ticks in the figure show the unit vectors of gas flow directions. (d) Maximum induced dynamic pressure with the unit of P_0. (e) Maximum shock induced gas temperature. T_0 is venusian surface temperature, 735 K.

the impact crater, because over most of the planetary surface, the shock front intersects the surface with $\alpha \sim 90°$. The maximum pressure induced by the shock waves are also shown in Figure 7-1(a) - Figure 7-4(a). Here, P_0 is the ambient pressure of the venusian atmosphere on the surface. There are discontinuities of the isobars in the transition zones between different shock reflection modes in the cases of smaller Φ. This corresponds to the discontinuity that can be seen in the transition of Mach reflection from the regular reflection in Figure 6 (b). The pressure produced by atmospheric shock is $\sim 10^2$ GPa in the center of a crater and $\sim 10^1$ GPa at the rim of a crater for the impact of a 1 km-radius meteoroid at 20 km/s impact velocity.

The maximum density compressed by the shock, $\rho_s(X, Y)$, is shown in Figure 7-1(b) - Figure 7-4(b). There are discontinuities of the profiles in the transition zones between different shock reflection modes in the cases of smaller Φ as can also be seen in the pressure profiles of Figure 7-1(a) - Figure 7-4(a). The lower the impact angle Φ becomes, the wider the region of high density in the up-range direction.

The maximum horizontal gas particle velocity generated by the shock wave $U(X, Y)$ is also plotted in Figure 7-1(c) - Figure 7-4(c) for different Φ. A considerable area (e.g., within $\sim 20R_c$ for $\Phi = 30°$) is affected by the strong (> 100 m/s) gas velocity in this case. The direction of the gas flow is also shown in Figure 7-1(c) - Figure 7-4(c) with small ticks. Strong gas flow occurs initially radially from the center of the impact, but in the case of oblique impacts, this flow changes to become perpendicular to the incoming trajectory of the body in the up-range region.

Figure 7-1(d) - Figure 7-4(d) show the maximum dynamic pressure, $\rho_s U^2$, calculated from the results of Figure 7-1(b) - Figure 7-4(b) and Figure 7-1(c) - 7-4(c). The maximum dynamic pressure is $\sim 10^2$ GPa at the center of the impact. Since the ranges of the dynamic pressure are affected by the gas density and the gas particle velocity, as Φ becomes smaller, or the radial distance from the center becomes smaller, the contours change from circular to shapes which are constricted around the center of the impact along the up-range footprint of the projectile trajectory. This bilateral symmetry was previously qualitatively estimated in Ivanov *et al.* [1986].

Horizontal gas flow induces viscous stresses, which in turn produce surface disturbance. From Figure 7 (c) and (d), in the case of larger Φ, the materials can be transported radially on the planetary surface around the crater. In the case of smaller Φ, in the up-range region, the gas flow moves materials toward the perpendicular to the trajectory footprint rather than dispersing them radially from the center of the impact. This can cause the material to be transported toward the incoming direction and in the direction which is perpendicular to the trajectory footprint. Thus particle motion can cause elongation and bilateral distributions of surface material.

Although there may be significant atmospheric effects of blast waves on the surface of Venus, the thermal energy content of these gas shocks is insufficient for production of significant thermal metamorphism outside the range of the crater ejecta in this case of V_i=20 km/s and R=1 km. The gas temperatures are less than $\sim$ 2000 K over areas not covered by the crater ejecta (Figure 7-1 (e) - Figure 7-4 (e)).

From Figure 7, it is clear that the region affected by the shock wave becomes wider and more elongated in the up-range region with decreasing Φ, that is with greater obliquity of impact.

The effects of the impact velocity on the shock properties along the footprint of the impactor's trajectory in the up-range direction ($X > 0$ and Y=0 in Eq. (3-1) and (3-2)) are shown for the case of $\Phi = 45°$ in Figure 8.

Figure 8 (a) shows the profiles of the maximum pressure. There is a kink in the pressure profile of V_i = 50 km/s in Figure 8 (a) because of the transition from the regular reflection to Mach reflection. The maximum shock density is shown in Figure 8 (b) in units of ρ_0=65kg/m^3. Figure 8 (c) shows the maximum horizontal gas velocity for various velocities. The gas velocity decreases more rapidly at the region close to the subsonic region. The horizontal gas velocity becomes zero, and the corresponding kink exists on the tangential contact point of the bow shock to the surface (e.g., at $X/R \sim 1.4$, in the case of $\Phi = 45°$), which is nearly inside the crater. The dynamic pressure is in units of P_0 in the cases of Figure 8 (d). In Figure 8 (e), maximum shock induced gas temperature is shown in units of venusian surface temperature, $T_0 = 735$ K.

The ratio of the radius of the crater to that of the impactor is proportional to $\sim V_i^{0.32}$ from Eq. (11). In the case of normal impact or the case without modification by the mode of reflection, the distance of the subsonic region (e.g. r/R for M_1 $\sim$1) varies as $\sim V_i$. Therefore, the region affected by the gas shock compared to the radius of the crater becomes wider, as the impact velocity increases.

3.2 Gas properties of the atmosphere

We have used the effective ratio of the specific heat γ instead of the exact ratio of the specific heat for a perfect gas, and used the value of $\gamma = 1.1$ for CO_2 in our calculations. In the case of triatomic CO_2 gas, γ is 1.20 at 730 K, and 1.15 at 2900 K at 1 atm [*Hilsenrath et al.*, 1955], and the variation of γ depends primarily on the temperature. However, the density behind the bow shock can reach higher values in the case of an ideal dissociating gas than in the case of a perfect gas if

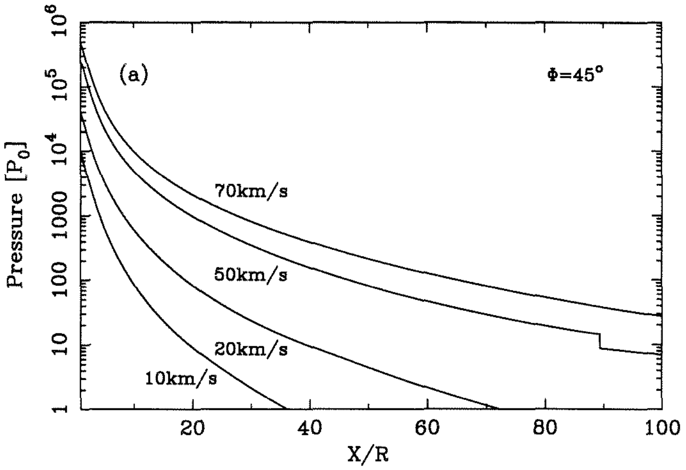
(a)
Φ=45°
Pressure [P$_0$]
10^6
10^5
10^4
1000
100
10
1
70km/s
50km/s
20km/s
10km/s
20
40
60
80
100
X/R

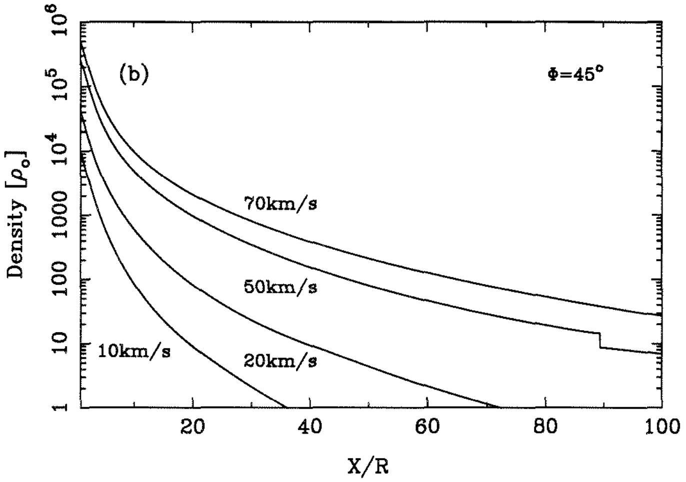
(b)
Φ=45°
Density [ρ_o]
10^6
10^5
10^4
1000
100
10
1
70km/s
50km/s
20km/s
10km/s
20
40
60
80
100
X/R

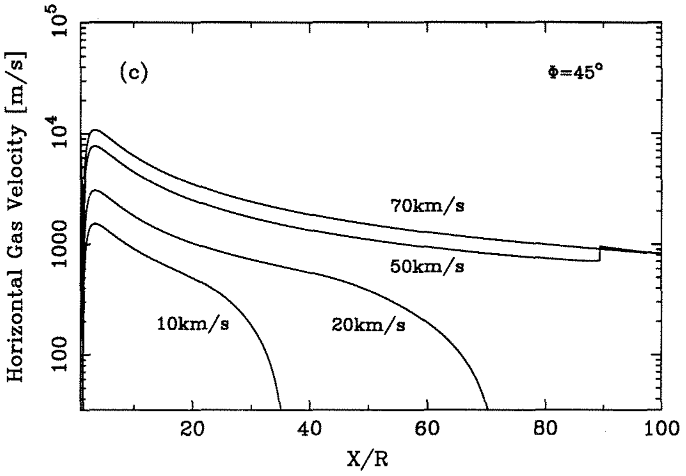
(c)
Φ=45°
Horizontal Gas Velocity [m/s]
10^5
10^4
1000
100
70km/s
50km/s
10km/s
20km/s
20
40
60
80
100
X/R

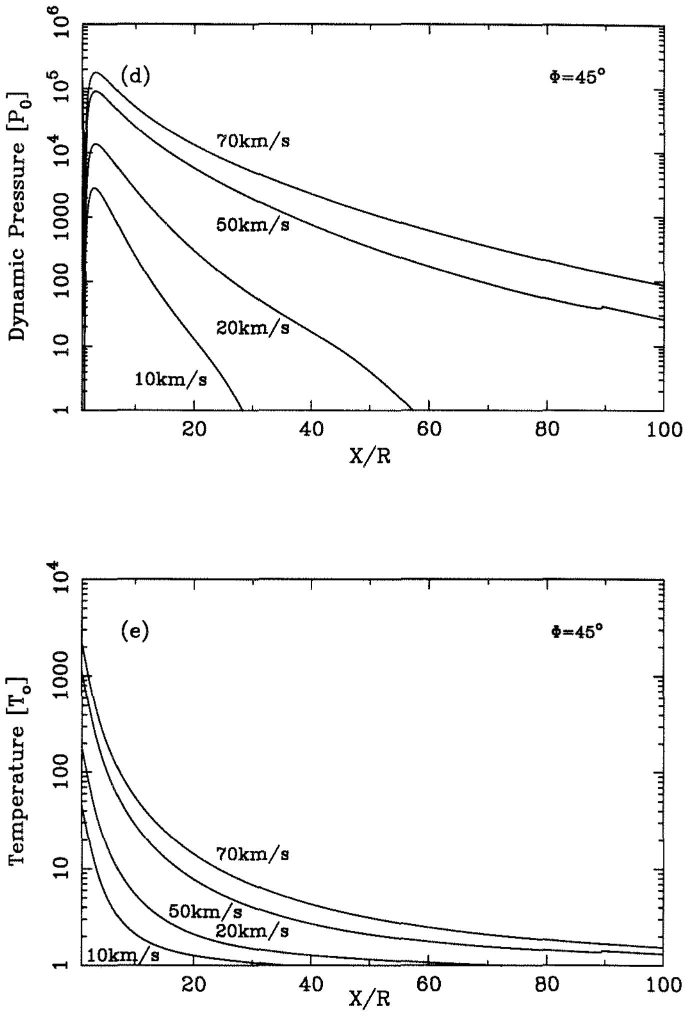

Figure 8. Shock properties for various impact velocities in the case of impact angle $\Phi = 45°$ as a function of distance from the center of the crater toward the incoming direction, along the trajectory footprint. Impact velocities V_i of 10 km/s, 20 km/s, 50 km/s, and 70 km/s are selected. (a) Maximum relative shock pressure [P/P$_0$]. (b) Maximum relative shock density [ρ/ρ_0]. (c) Maximum horizontal gas velocity. (d) Maximum relative dynamic pressure [P/P$_0$]. (e) Maximum relative gas temperature [T/T$_0$].

significant amounts of dissociation occur behind the shock and γ decreases close to unity [*Vincenti and Kruger*, p. 182, 1965]. In the case of CO_2, the calculation of the ideal dissociating gas for $M \sim 12$ shows that the ratio of the density before and behind the shock becomes ~ 23 in the state of the dissociative relaxation, and the corresponding γ becomes 1.09 [*H. Hornung*, unpublished data, 1992]. Therefore, in order to take into account real gas effects, we used a smaller effective ratio, γ, rather than the value expected for the perfect gas. From Figure 6 (b), in the case of smaller M (< 5), the effect of the different γ to the shock properties is not significant, but for large M, the effect of dissociation is important. The uncertainties in shock properties in the case of a different value of γ to those of $\gamma_0 = 1.1$ is roughly $P(\gamma)/P(\gamma_0) = 1.9\gamma/(\gamma+1)$ for shock pressure and $\rho(\gamma)/\rho(\gamma_0) = 21(\gamma-1)/(\gamma+1)$ for shock density for normal impact. Therefore, pressure doesn't change so much; however, the dynamic pressure changes about a factor 2 to 4. If the gain of the enthalpy increases further to dissociate the gas completely, the gas becomes monatomic; moreover, electronic excitation becomes significant at $T > 10^4$ K. Then, γ increases up to 5/3. In the region outside of a crater and the ejecta, the gas temperature is not high enough to dissociate the gas (e.g., fig. 7(e) and fig. 8(e)), and the constant $\gamma \sim 1.1$ is a reasonable value to utilize for describing the shock-induced gas over a wide area.

3.3 Time dependence of shock properties

We have estimated the maximum shock properties at each point of the planetary surface; however, in the case of a blast wave expansion, the shock properties at a given position are functions of time. The pressure increases suddenly to the peak value estimated upon the shock arrival. Attenuation then occurs and the shock pressure decreases below the ambient value upon the arrival of the rarefaction wave. The pressure, then, relaxes to the ambient state. Attenuation is estimated using the axisymmetric power laws shown in Figure 2 (b), due to the similarity of the bow shock model to the axisymmetric blast wave. In the following discussion, we estimate the time variable gas shock properties by applying the method of Zel'dovich and Raizer [1965] to the case of a cylindrical blast wave.

The distance of the shock wave from the center of the impact normalized by R, at time t, after the impact, $r_s(t)$, and its propagation velocity, $dr_s/dt(t)$, is, from Eq. (6), proportional to $t^{1/2}$ and $t^{-1/2}$, respectively. Assuming that the shock wave arrives at $t_0(< t)$ and t at a distance of $r_s(t_0)$ and $r_s(t)$, the ratio of the maximum pressure, density, and gas velocity at time, t, to those at t_0, are: $P_{max}(t)/P_{max}(t_0) \sim t_0/t$, $\rho_{max}(t)/\rho_{max}(t_0) \sim 1$, and $U_{max}(t)/U_{max}(t_0) \sim (t_0/t)^{1/2}$. Here, the subscript '$max$' indicates the maximum value at each position. The ratios of the attenuated shock properties at $r_s(t_0)$, at time, t, relative to the maximum shock properties at $r_s(t)$, expressed by the axisymmetric power law are $P(t)/P_{max}(t) \sim \eta(y_0)$, $\rho(t)/\rho_{max}(t) \sim \zeta(y_0)$, and $U(t)/U_{max}(t) \sim \xi(y_0)$, as seen in figure 2(b). Here, η, ζ, and ξ, are the similarity function calculated in Figure 2 (b), for the pressure, density, and velocity and $y_0 = r/r_s$.

Therefore, at the position of $r_s(t_0)$, the parameters of the shock properties as a function of time are given approximately as

$$P(t) \sim P_{max}(t_0)(t_0/t)\eta((t_0/t)^{1/2}) \qquad (12-1)$$

$$\rho(t) \sim \rho_{max}(t_0)\zeta((t_0/t)^{1/2}) \qquad (12-2)$$

and

$$U(t) \sim U_{max}(t_0)(t_0/t)^{1/2}\xi((t_0/t)^{1/2}), \qquad (12-3)$$

when $t \geq t_0$. At $t < t_0$, P and ρ are equal to the initial ambient values, and $U = 0$. Figure 2 (b) shows that the function of η becomes a constant of 0.47, as $y_0 < 0.8$, and $\xi(y_0) \sim y_0$, so we can approximate the pressure and the velocity as $P(t) \sim 0.5P_{max}(t_0)t_0/t$ and $U(t) \sim U_{max}(t_0)t_0/t$ at the same position. Therefore, even though the attenuation of shock wave is transient, the attenuation of shock properties is more gradual at greater distances from the center of the crater. At larger distances from the center of the crater, once shock properties achieve sufficient magnitude to cause the disturbance of the surface properties, then the time duration to keep the same magnitude of shock properties at the same position is longer. Therefore, maximum shock properties was examined in present work as the first approximation.

3.4 Entrainment of surface materials

In this section, the magnitude of the surface disturbance is estimated using the shock properties obtained in the section of 3-1. The change of the surface features around the site of large near-surface explosions is mainly caused by deposition of thrown-out ejecta and by deposition of the debris (dusts, pebbles, rocks, and boulders) lofted outside the crater by the high speed wind associated with the blast wave. The viscous stresses associated with this gas flow above the surface entrain and loft the surface materials and form the turbulent mixing of dusts and pebbles with the atmosphere. Then surface materials are scoured and finally re-deposited, and this changes the original surface features. We assume that the effects on a planetary surface induced by impact cratering are analogous to the effects of large near-surface explosions. The present bow shock model demonstrates that a wide region compared to the crater radius can be affected by the shock wave and the following horizontal high-velocity gas wind. Although this high-speed gas flow is transient, it is expected to loft surface materials and change the surface properties.

In order to examine how wide a surface area can be affected by the impact, we will employ the shock properties of the gas calculated from the bow shock model to the saltation or suspension regime.

The horizontal wind velocity U is related to the wind friction velocity u_* with a friction coefficient C'_f, and is given for the case of the Reynolds number, Re, of order more than 10 for steady flow as

$$u_*^2 = \frac{1}{2} C'_f U^2 \tag{13}$$

[*Iversen et al.*, 1976].

We note that C'_f changes from $\sim 10^{-4}$ to $\sim 10^{-2}$ depending on the roughness of the surface and the type of flow (steady versus transient) [*Rosenblatt*, 1985]. We use $C'_f \sim 0.0015$ for turbulent flows with Re of $\sim 10^9$ [*Tani*, 1967] for the case in which the value of CO_2 viscosity is $\sim 10^{-5}$ Pa·s [*White*, 1974], $D_p \simeq 10^{-1}$m, $U \sim 10^3$m/s, and $\rho \sim 10^2$kg/m^3. C'_f becomes 0.003 for Re of 10^7; therefore, the value we use is a lower limit.

The threshold friction velocity, u_{*t}, that is the friction velocity required to initiate lofting and saltation of a particle of diameter, D_p, can be written as

$$u_{*t} = A\left[\frac{(\rho_p - \rho)}{\rho} g D_p\right]^{1/2} \tag{14}$$

where ρ_p is the particle density ($\simeq 2800$ kg/m^3), ρ is gas density, and the coefficient A is estimated as 0.11 for μm to 1cm size particles [*Iversen et al.*, 1976]. We assume that the value of the coefficient is effective for $10^0 - 10^1$ cm sized-rocks, since no experimental work for > cm rocks has been conducted. We apply this equation to the gas flow induced by the paraboloidal bow shock wave. By setting $u_* = u_{*t}$ in Eqs. (13) and (14), then we can estimate the maximum saltation rock size with given gas velocity. This can be applied to the region where the propagation of the shock wave becomes supersonic, since the wind velocity is comparable and the attenuation of the velocity is slower.

In Figure 9, maximum saltation rock size is calculated for $V_i = 20$ km/s and $\Phi = 30°$ using the maximum gas velocity, density profiles, and dynamic pressure of Figure 7-3. In this case, the dynamic pressure of 1 MPa can induce saltation of boulders up to the order of 1 m in size. Moreover, rocks of less than 10 cm in size

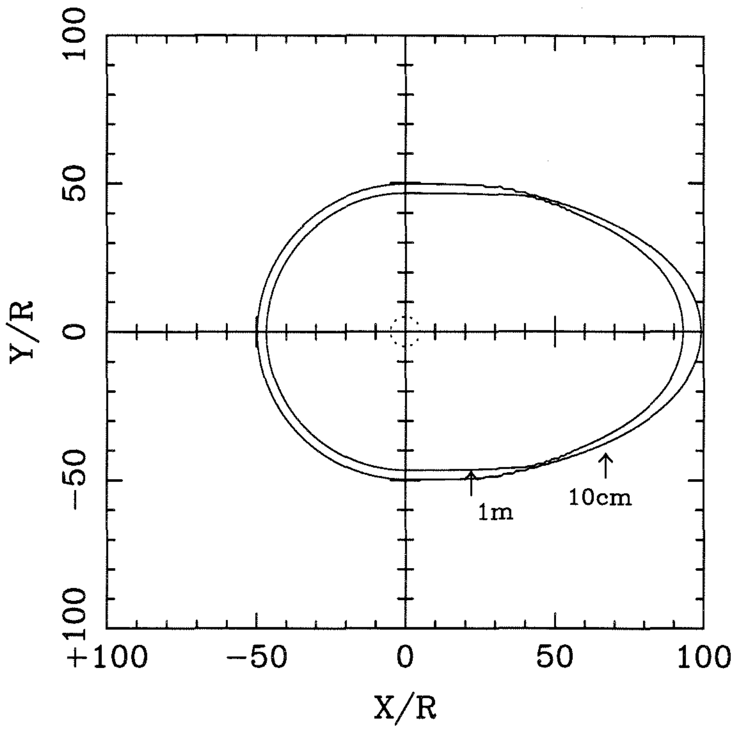

Figure 9. Maximum saltation boulder size calculated in the case of impact velocity $V_i =$ 20 km/s and impact angle $\Phi = 30°$ using profiles in Figure 7-3. The crater size estimated from Eq. (11), $R_c = 4.3R$, is shown as a dotted line.

can be saltated within most of the area of the supersonic region. Since particles of several millimeters in the maximum size can be moved easily by venusian surface winds [*Greeley et al.*, 1984], the lofting of particles of more than one centimeter in size is unique to the impact processes.

In the case of steady flow, the travel distance of the particles is $\sim 10u_*^2/g \sim C_f'U^2/2$, if the final velocity, that is the downward velocity of rock particles, w_F, is less than u_* [*Bagnold*, 1941]. The final velocity is smaller when the size of the particle becomes smaller. The transport distance is expected to be less than this estimate, because of the transient flow of the shock.

3.5 Degree of mutual comminution

Particles of surface materials, once in motion, can be comminuted via mutual collision and collisions with the planetary surface resulting in a fine grained porous deposit. Therefore, in this section, we will estimate the degree of mutual comminution of the entrained materials in the gas flow analogous to impact fragmentation.

The largest size of the fragment of the target, D_{pL}, produced by the projectile of size D_{pp} onto the target of size D_{pt} for the same materials is expressed as

$$(\frac{D_{pL}}{D_{pt}})^3 = 0.024(\frac{P_i D_{pp}^3}{Y D_{pt}^3})^{-0.93} \tag{15}$$

[*Mizutani et al.*, 1990]. This is applicable if $D_{pp} \leq D_{pt}$, where Y is the fracture strength of the rocks and P_i is the impact pressure calculated from the Hugoniot equation of $P_i \sim \rho_p u_p c_p$ in the case of $u_p/c_p \ll 1$. Here c_p is the bulk sound velocity of the particle materials and u_p is the relative velocity of the particles. This shock pressure is also applicable to the case of low impact velocity of ≤ 10 m/s within a factor of two. We use the values of basalt in *Mizutani et al.* [1990]. Then $Y \sim 480$ MPa and $c_p \sim 5040$ m/s.

The rock particles might continuously collide several times or never collide. They also might impact obliquely. However, for simplicity in our model, every particle collides normally, at least once, with a particle of the same or larger size with their characteristic velocity. We considered two characteristic relative velocities. One occurs when the entrained materials fall to the Venus surface and impacts rocks on the surface. Another occurs when the surface materials are entrained and impact other rocks in the flow.

In the first case, the impact velocity is almost the same order of the final velocity, w_F, which is calculated as

$$3C_D \rho w_F^2 = 4D_p(\rho_p - \rho)g \tag{16}$$

C_D is 0.5 in the case of $w_F < 10^1$ m/s and $Re \sim 10^4$ [*White*, 1974]. Then, the ratio of the largest size of the post-collisional fragment to the initial size, D_{pL}/D_p, becomes ~ 0.4 when $D_p \sim 10$ cm, and D_{pL}/D_p becomes ~ 0.6 when $D_p \sim 1$ cm.

In the latter case, the impact velocity is almost equal to the initial upward saltation velocity, w. Since w is the same order of u_* [*Bagnold*, 1988], we assume impact velocity $u_p \sim u_*$. In the case of impact velocity of 20 km/s and impact angle of 30° as in Figure 9, the calculated ratio of the largest fragment size to the initial size, D_{pL}/D_p, is shown in Figure 10. The degree of mutual collision is effective in the region close to the crater (the particle size is reduced by 50% at $\sim$ 40R and reduced to 25% at $\sim$ 15R), and in the region of the hypersonic flow propagation. However, it is relatively less effective in the region of the supersonic flow and not in the subsonic region at all.

Both cases may occur wherever the size of surface materials allow lofting and saltation or suspension. As a result, the surface materials must be affected by lofting, turn-over, and the mutual collision of rocks in the wide area as compared to the crater radius. The surface features are thus changed by the shock induced gas flow. This calculation shows that high impact velocity produces a wider area affected by saltation, crushing and redistribution of surface materials, and that oblique impact induces a more elongated affected area, which is oriented toward the up-range direction. This is consistent with the observation of halos that elongate toward the opposite direction of the ejecta distribution, as shown in Figure 1.

4. Discussion

4.1 Wide crater halos

In this section, we are going to apply the results of the bow shock model to the crater located at 16.5° north latitude and 334.4° longitude shown in Figure 1 (a) in

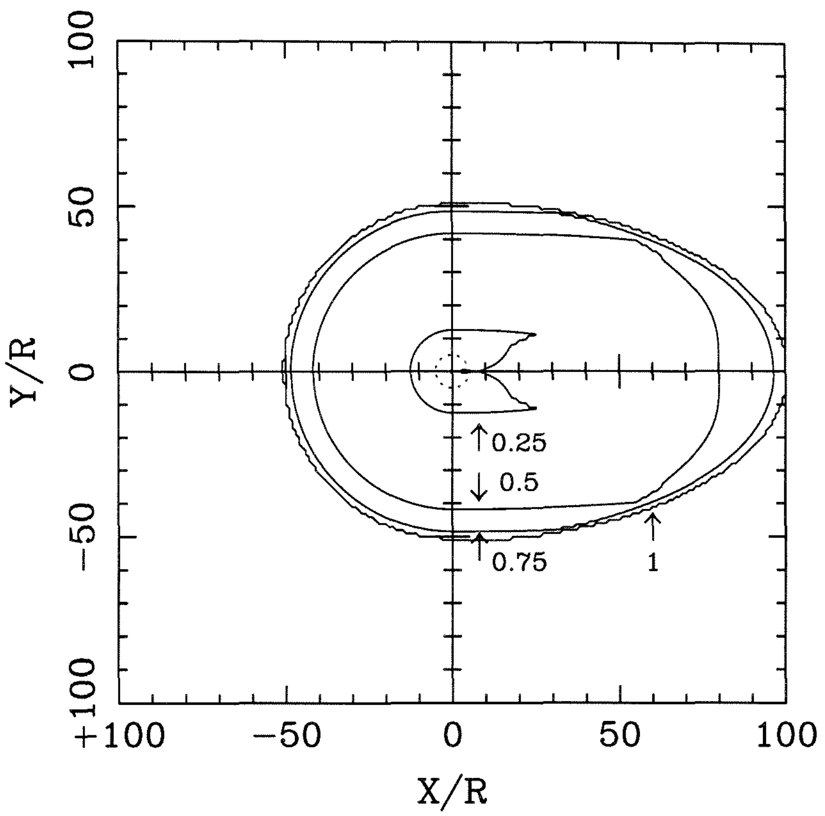

Figure 10. The ratio of the maximum fragment size relative to the original size. Contours of the ratio of the largest size of the post-collisional surface particles relative to the original target size, D_{pL}/D_{pt}, in the case of collision with particles of the same size. Impact parameters are the same as figure 9.

order to test the causes of radar dark/bright halos.

In the case of this crater, the median value of the backscatter cross section, σ_{med} of Figure 1 (a), is -14.2 dB, that of the region of the dark halo σ_D is -17.6 dB, and that of the region of bright halo σ_B is -11.6 dB as measured along the longest radius of the halo of this crater. The backscatter cross section is obtained by the conversion from the pixel value in SAR image data, which is normalized by the scattering coefficient of Muhleman's law for the radar incidence angle of the particular pixel ($\sim$ 44° at

16.5°N) [*Hyon*, 1991; *Plaut*, personal communication, 1991].

First, we assume that the dielectric constant of the surface materials and the radar incidence angle are the same everywhere in this region, that the surface is flat, and that the change in backscatter cross section is caused mainly by the change of surface roughness, h. h should be approximately on the order of the largest particle size, so that $O(h) \simeq O(D_{pL})$. The difference (Δ) in h is related to the difference in backscatter cross section (in dB) by

$$\Delta[\log(h)] = 0.05\Delta\sigma \tag{17}$$

for Bragg scattering [*Ulaby*, 1982]. For Eq. (17) to be valid, h must be less than the scale of radar wavelength (λ). From this relationship, the average values of relative ratio of roughness of the disturbed regions of dark halo, h_D, to the original surface, h, h_D/h, and that of the bright halo, h_B, to the original surface, h_B/h, of the crater in figure 1(a) are approximately 0.7 and 1.3, respectively.

Alternatively, we could assume that the change of backscatter cross sections is caused by the radar penetration into a surface layer of varying degree of porosity. The thickness of the porous layer should be approximately proportional to the maximum saltation boulder size, D_p, in each region, if the transportation of the materials is ignored. The relationship of the difference of the layer thickness Δd and the difference of the backscatter cross section $\Delta\sigma$ [dB] can be expressed approximately,

$$\Delta d = -0.12 L_p \Delta\sigma \tag{18}$$

where L_p is the penetration depth which is 9.2λ for dry soil [*Elachi*, 1987]. From this equation, the region of dark halo has an $\sim$ 50 cm thicker porous surface layer superimposed on the original average surface materials. If the high backscatter cross section is caused by the lack of a porous layer, then the thickness of the porous layer of the region of the bright halo is approximately 35cm thinner than that of the original surface.

Taking into account the cause of the dark halo surrounded by the bright halo, the dark halo would represent the re-deposit of finer regolith that are comminuted by the mutual collision and deposit of the finer particles ejected directly from the surface. This increases local surface porosity and the smooth porous surface results in a radar backscatter cross section lower than the original surface in the vicinity of the crater. The bright halo is caused by a change of roughness rather than the reduction of the thickness of the porous layer. In this region, the saltation is not effective enough to induce boulders to be broken-up. Instead they may be turned over and redeposited, whereas the finer particles are suspended and are diffused over a wider area. Thus, a roughened surface can be induced by the blast wave which will result in a higher radar backscatter cross section than that of the original surface (Figure 11).

4.2 Application of the model to the venusian craters

The ratio of the distance from the crater's center to the boundary of the supersonic flow region, r_t, to the meteoroid's radius, R, becomes a linear function of the impact velocity in the case of the vertical impact from Eqs. (3-1) and (4), as

$$\frac{r_t}{R} \simeq 2.5V_i \tag{19}$$

Here, V_i is in the unit of km/s. Using the scaling law of Eq. (11), the size of the crater, R_c, becomes $\sim$ 3-5R for R=1 km, $\rho_m = 10^3 \mathrm{kg/m}^3$, and V_i=20 km/s; the ratio of the radius of the supersonic shock region to the radius of the crater, r_t/R_c, then becomes $\sim$ 10-17 with $15° < \Phi < 60°$. The ratio of the shortest distance from the center of the crater to the boundary, r_{ts}, to the longest one, r_{tl}, r_{ts}/r_{tl}, becomes approximately $\sin\Phi$ from Eq. (4), if $M_1 \gg 1$.

We assume that the initial Venusian surface contains a range of grain sizes less than order 10 centimeters. In the region where particles of a large size (a few cm to $\sim$ 10 cm) cannot be entrained and suspended, finer particles deposited upon and

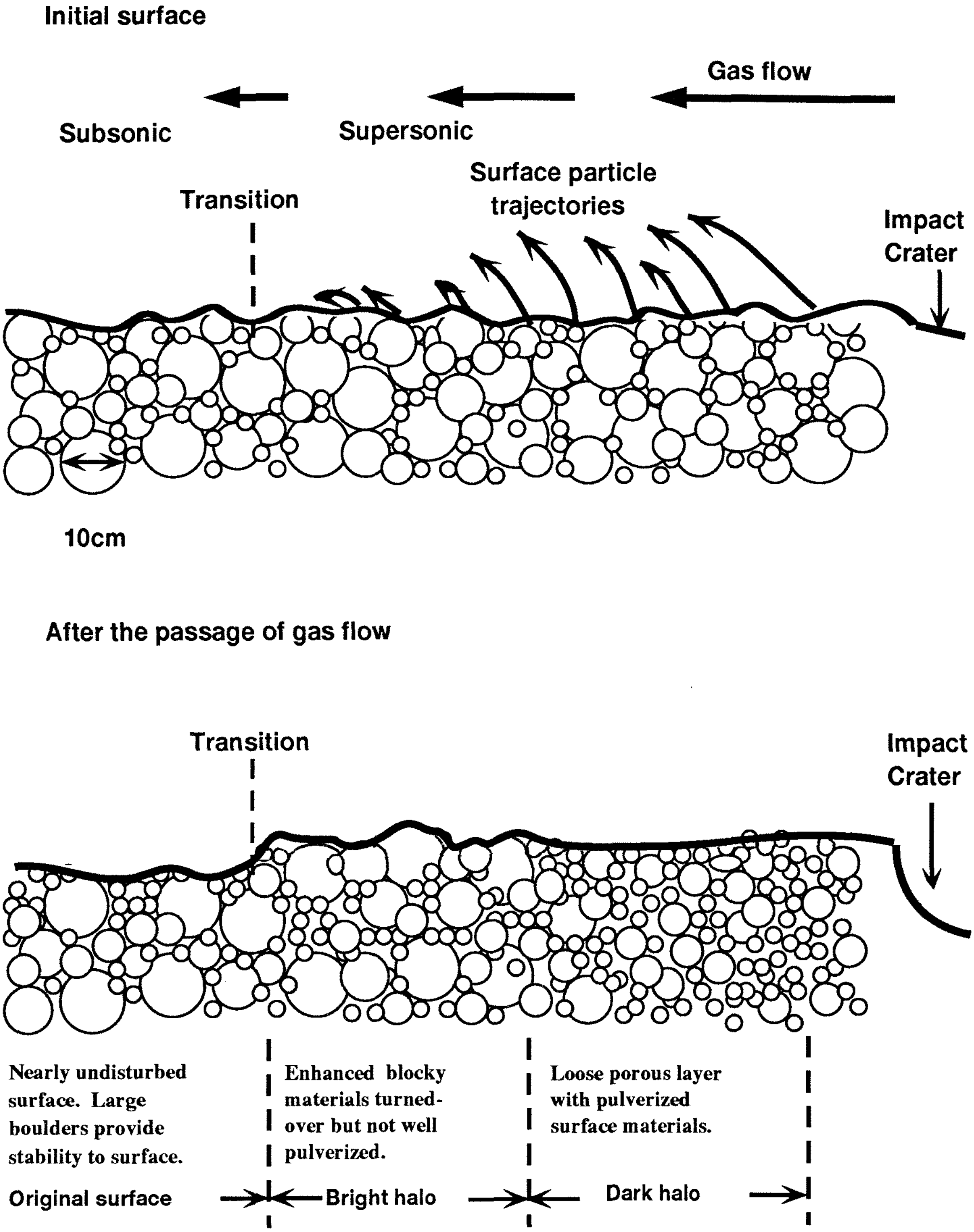

Figure 11. Sketch of the change of the surface disturbance by the gas flow as a function of the distance from the crater center. The surface stated of the prior- and the post-shock wave's passage. The surface is assumed to consist of particles of less than 10 cm in size.

between the large cobbles can be lofted, whereas material beneath the cobbles cannot, so the effect of the disturbance of the surface is expected to be small, maintaining approximately the original radar properties (Figure 11). Therefore, we assume that the transition from the undisturbed area to the disturbed area in radar properties occurs approximately in the locations where the maximum saltation boulder size is about 10 centimeters, and this is approximately the boundary between the supersonic flow region and subsonic flow region (Figure 7-3 (a) and Figure 9).

Then the Eq. (19) becomes

$$R_c/R = 2.5V_i(R_c/r_{hs}) \tag{20}$$

where r_{hs} is the shortest radial size of the halo, and r_{hs} is defined in Figure 12 as well as the longest radial distance, r_{hl}. We can observe the radius of the halos, r_h (r_{hs}, r_{hl}) and R_c. Therefore, eq. (20) can provide the relationship between the impact velocity and the radius of the meteoroid, and the observed radius of the halo around the crater.

In the case of the crater in figure 1(a), the longest radial distance of the bright halo, r_{hl}, and the shortest radial distance, r_{hs}, are approximately 74 km and 50 km, respectively. The ratio of the longest to the shortest halo of the crater is approximately $r_{hs}/r_{hl} \sim \sin\Phi$, and this corresponds to an impact angle, Φ, of $\sim 43°$(Figure 12). The radius of the crater, R_c, is $\sim$ 3100m. Then assuming that it is caused by an icy comet of a density of 1000 kg/m ^{3}, the features correspond to an impact velocity on the surface V_i of 45 km/s and R of $\sim$ 450 m. The corresponding incident velocity becomes $\sim$ 55 km/s and this is in the range of possible impact quantities.

In the case of the crater in figure 1(b), r_{hl} and r_{hs} are approximately 98 km and 43 km, respectively. From these ratio, an impact angle is assumed to be $\sim 26°$. Assuming the impact of an icy body, the calculated impact velocity on the surface V_i of $\sim$ 17 km/s and R of $\sim$ 1000 m are obtained. The corresponding incident velocity

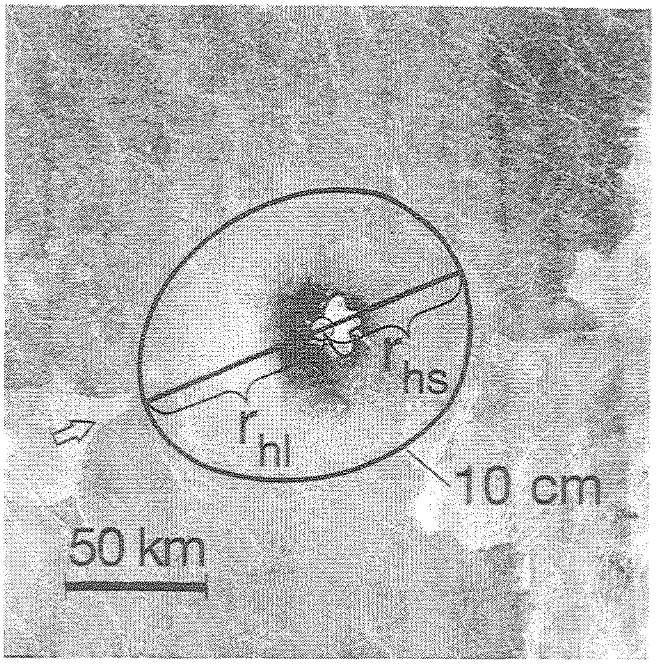

Figure 12. Crater image of Figure 1(a) with the contour that represents the calculated maximum saltation boulder size of 10 cm resulting from the impact of the meteoroid of a 450 m radius with an impact velocity of 45 km/sec and an impact angle of 43°.

is ~ 20 km/s and it is also plausible on Venus. The estimated impact angle is smaller than the one of the impact crater in figure 1(a). This agrees with the difference of the ejecta shapes in two craters that shows the impact crater in figure 1(b) formed with lower impact angle. The shape of the halos in figure 1(b) shows the butterfly shape in the up-range. This also agrees with the lower impact angle.

From the application to above two impact craters, the bow shock model can, in principle, explain the formation of halos and its geometry.

4.3 Constraints of the bow shock model

We assumed that the shape and mass of a meteoroid are constant while it travels in the venusian atmosphere. We also assumed that the incoming angle is constant and the meteoroid does not decelerate in the venusian atmosphere. However, the initial shape of the meteoroid may not be a spherical. There may also be deformation, fragmentation, or ablation taking place in the atmosphere. The trajectory of the meteoroid may also change due to the atmospheric drag or to a change of mass. We discuss these effects on the bow shock model and constraints here.

The deformation or the irregular shape of the body does not affect the power law of Eq. (2) in the far wake, if we use the characteristic radius, R_n (the radius of the curvature on the stagnation point), instead of the radius of the sphere, R [*Martin*, 1966]. For example, if the body is cylindrical with the radius of the cylinder R_{cl} and the plane surface faces the flow field, Eq. (1) becomes $\Delta_s/R_{cl} \sim [(\gamma-1)/2]^{0.5}$ [*Martin*, 1966], and R_n approaches

$$R_n \sim (\Delta_s^2 + R_{cl}^2)/(2\Delta_s) \tag{21}$$

as $M \to \infty$, as the first approximation.

Fragmentation of meteoroids is expected to be a common phenomena, since the strength of the stony meteorites are ~ 6-500 MPa [*Melosh*, 1981], and the dynamic pressure at the stagnation point, ρv^2, of 10^2 MPa, is easily achieved at an altitude below 60 km for meteoroid velocities of 10 km/s. Meteoroid fragmentation was expected to decelerate a body. Also, dispersal of the meteoroid widens the area of the cross section per unit mass, and as a result, the drag force acting on unit mass becomes larger. Passey and Melosh (1980) analytically concluded that several bow shocks would form and surround each fragment. The experimental results [*Schultz and Gault*, 1992] and numerical simulations [*Takata et al.*, 1994], however, show that the bow shock tends to contain a collection of fragments within a bow shock rather than dispersing the fragments, and the swarm of fragments itself changes its shape to minimize the atmospheric drag and deceleration in the high atmospheric pressure in the case of hypersonic impact. Therefore, the deceleration due to the break-up would be smaller than the degree which has been widely considered in the past.

The change in the size of a meteoroid due to ablation is approximately expressed as $R_i/R_\infty \sim \exp(\frac{\sigma}{6}(V_i^2 - V_\infty^2))$ [*Nagasawa*, 1981], where R_i is the radius of the meteoroid when it impacts the surface, R_∞ is the initial radius of the meteoroid before it encounters the atmosphere, and σ is the ablation coefficient in the order of $\sim 10^{-3}$ [s^2/km^2] [*Takata et al.*, 1994]. If $R_\infty < 100$ m, R_i/R_∞ decreases dramatically and it will not keep the shape of the exact paraboloid [Roddy *et al.*, 1992].

We assumed a uniform atmosphere in these calculations. If the size of the body becomes comparable to or larger than the scale height of the atmosphere (~15 km for Venus), the area impacted by the bow shock wave becomes smaller compared to the radius of the meteoroid, and the ratio of the impact energy coupled with the atmosphere to the initial impact energy becomes small. This phenomena agrees with the Magellan observational fact that halos can be observed around the craters of relatively small sizes [Schaber et al. 1992].

The original atmospheric shock feature would be modified by the strong zonal westward winds that can transport the ejecta in crater diameters larger than 15 km and distribute the deposit as a parabolic feature [*Arvidson et al.*, 1991; *Vervack and Melosh*, 1992].

Therefore, to summarize, the size of craters which is subjected to the above analysis is restricted to those with radii that are less than order 10^1 km. The bow shock model is directly applicable to meteoroids in the range of the radius between ~ 100 m and ~ 10 km for the expecting impact velocity on the orbit of Venus. In the case of the existence of significant deceleration or mass loss, the modification of the above theoretical analysis has to be conducted.

5. Conclusions

We have investigated the origin of the dark and bright halos around the craters that are observed by Magellan imagery. We have developed a bow shock model to understand the horizontal profile of gas shock properties on the venusian surface originating from a meteoroidal impact as the most likely origin of the dark and bright halos. From the propagation of a paraboloidal bow shock front interacting with a planetary surface, we considered the shock propagation of an oblique impact. We also took into account the effects of shock reflection from the venusian surface. For various impact angles and impact velocities, we calculated the maximum gas pressure, horizontal gas velocity, and temperature. The strong wind induced by the shock wave can, in principle, loft the surface materials, which can then be fragmented by mutual collisions. We estimated the saltation boulder size induced by the gas flow, and the magnitude of the effect of crushing of surface materials. The results show that a wide area can be affected by the surface disturbance by the strong gas flow (wind) induced by shock wave. The radial size of the disturbed area becomes 10 - 17 R_c, in the case of V_i=20 km/s and R=1 km. As a result, gas shock inducing the disturbance of the surface materials is likely to be the origin of the changes of the radar backscatter which give rise to both dark and bright halos. As an example, we investigated the crater in Figure 1(a). We infer that the dark halo originated from the fine porous materials produced by the mutual collision of saltated and crushing rocks. The bright halo is probably a rougher surface that is produced by the deposition of the rocks with dimensions of the order of the radar wavelength, 12.6 cm. In the region of the bright halo, the surface is excavated and turned over but not sufficiently pulverized to lower the backscatter. This process results in the deposit of blocky materials. We can relate the impact velocity, radius of the meteoroid, and the radius of the propagation of the supersonic shock wave ($\sim$ radius of the halos) using the bow shock model.

Finally, we obtained a relationship between the impact velocity, crater and projectile radius and the size of halos (Eq.20).

6. Acknowledgements

We would like to thank personnel associated with the Magellan mission for their efforts. We thank Dr. H. Hornung (Caltech) for valuable suggestions and comments which lead to the development of the present shock model. We thank Dr. J. D. O'Keefe (Caltech), Dr. B. A. Ivanov (Russian Academy of Science), and Dr. B. Sturtevant (Caltech), for their valuable suggestions and comments on the shock interactions with Venus. We also thank Dr. C. Elachi (JPL) for discussions on interpretation of the relationship of SAR data and surface properties, Dr. J. J. Plaut (JPL) for help on the SAR data analysis, Dr. C. Leff (JPL) for providing Magellan data, and Dr. R. Herrick (LPI), Mr. J. W. Holt (Caltech), and Ms. K. A. Tryka (Caltech) for their help on data analysis, and Dr. G. E. Danielson for producing crater-pictures. We thank Dr. R. M. Schmidt and anonymous reviewer for their constructive advice and criticism. Research supported under NAG1953. Contribution #5086, Division of Geological and Planetary Sciences, California Institute of Technology.

Appendix 1. The axisymmetric similarity solution

The gas is assumed to be a perfect gas with a constant ratio of specific heats and the flow is assumed to expand cylindrically; then the equations to characterize the motion of the gas are the momentum equation:

$$\frac{\partial v}{\partial t}+v\frac{\partial v}{\partial r}+\frac{1}{\rho}\frac{\partial p}{\partial r}=0 \qquad (A1-1)$$

the continuity equation:

$$\frac{\partial \rho}{\partial t}+\frac{\partial (v\rho)}{\partial r}+\frac{\rho v}{r}=0 \qquad (A1-2)$$

and the energy equation assuming that the flow is adiabatic:

$$\frac{\partial (p\rho^{-\gamma})}{\partial t}+v\frac{\partial (p\rho^{-\gamma})}{\partial r}=0 \qquad (A1-3)$$

[*Hornung*, 1967; *Hayes and Probstein*, 1966]. These are solved as a similarity solution; that is, the solution at time, t, is similar to the solution at any other time. The shock properties, such as p, ρ, and v, are just the functions of the lateral similarity variable, r/r_s, and the values at r_s (Figure 2(b)).

Appendix 2. The conservation equations for oblique shock

The conservation equations, through an oblique shock wave relating the upstream (subscript 1) and downstream (subscript 2), of density ρ, pressure P, Mach number M, deflection angle θ, and temperature T, are given by

$$\frac{\rho_2}{\rho_1} = \frac{(\gamma+1)M_1^2 \sin^2\alpha}{2+(\gamma-1)M_1^2 \sin^2\alpha} \qquad (A2-1)$$

$$\frac{p_2}{p_1} = \frac{2\gamma M_1^2 \sin^2\alpha - (\gamma-1)}{(\gamma+1)} \qquad (A2-2)$$

$$M_2^2 \sin^2(\alpha-\theta) = \frac{\gamma+1+(\gamma-1)(M_1^2 \sin^2\alpha - 1)}{\gamma+1+2\gamma(M_1^2 \sin^2\alpha - 1)} \qquad (A2-3)$$

$$\tan\theta = \tan\alpha \frac{M_1^2 \cos^2\alpha - cot^2\alpha}{0.5M_1^2(\gamma+\cos 2\alpha)+1} \qquad (A2-4)$$

$$\frac{T_2}{T_1} = \frac{p_2}{p_1}\frac{\rho_1}{\rho_2} \qquad (A2-5)$$

[*Hornung*, 1986]. Here θ is the deflected angle of a shock processed (downstream) gas flow to the pre-shocked (upstream) gas flow.

Eqs. (A2-1) to (A2-5) must be applied iteratively to both initial and reflected shocks to identify the corresponding shock reflection type.

References

Arvidson, R. E., V. R. Baker, C. Elachi, R. S. Saunders, and J. A. Wood, Magellan: Initial analysis of Venus surface modification, *Science*, *252*, 270-275, 1991.

Bagnold, R. A., *The Physics of Blown Sand and Desert Dunes*, pp 265, Methuen, London, 1941.

Bagnold R. A., *The Physics of Sediment Transport by Wind and Water*, pp 359, American Society of Civil Engineers, New York, 1988.

Brackett R. A. and W. B. Mckinnon, Cratering Mechanics on Venus: Pressure Enhancement by the Atmospheric Ocean, *Geophys. Res. Lett.*, **19**, 2115-2118, 1992.

Brode, H. L., Review of nuclear weapons effects, *Ann. Rev. Nuclear Sci.*, *18*, 153-202, 1968.

Bronshten, V. A., *Physics of Meteoric Phenomena*, pp 356, D. Reidel, Boston, 1983.

Courant, R. and K. O. Friedrichs, *Supersonic Flow and Shock Waves*, pp 464, Interscience Publishers, New York, 1948.

Elachi, C., *Introduction to the Physics and Techniques of Remote Sensing*, pp 413, John Wiley, New York, 1987.

Florenskiy, K. P., A. T. Bazilevskiy, G. A. Burba, O. V. Nikolayeva, A. A. Pronin, A. S. Selivanov, M. K. Narayeva, A. S. Panfilov, and V. P. Chemodanov, Panorama of Venera 9 and 10 landing sites, in *Venus* edited by D. M. Hunten, L. Colin, T. M. Donahue, and V. I. Moroz, p 149-153, University of Arizona Press, Tucson, 1983.

Gault, D. E. and J. A. Wedekind, Experimental studies of oblique impact, *Proc. Lunar Planet. Sci. Conf. IX*, 3,843-3,875, Pergamon press, New York, 1978.

Greeley, R., J. D. Iversen, R. N. Leach, J. R. Marshall, B. R. White, and S. H. Williams, Windblown sand on Venus: Preliminary results of laboratory simulations, *Icarus*, *57*, 112-124, 1984.

Hayes, W. D., and Probstein, R. F., *Hypersonic Flow Theory I*, pp 602, Academic Press, New York, 1966.

Heilig, W., Some aspects of curved shock waves, *Proceedings 5th Mach Reflection Symposium*, edited by G. W. Ullrich, San Francisco, 1985.

Hilsenrath, J., C. W. Beckett, W. S. Benedict, L. Fano, H. J. Masi, R. L. Nuttall, Y. S. Touloukian, and H. W. Woolley, Tables of thermal properties of gases, pp 488, *National Bureau of Standards Circular*, *564*, 1955.

Hornung, H. G., Inviscid hypersonic flow over axisymmetric power-law bodies, *Aero. Note*, *288*, 10 pp., Australian Defence Sci. Serv., Aero. Res. Lab., Melbourne, Australia, 1967.

Hornung, H. G., Regular and Mach reflection of shock waves, *Ann. Rev. Fluid. Mech.*, *18*, 35-58, 1986.

Hyon, J., Comments on Magellan MIDR CD-ROMS, *USA-NASA-JPL-MG-0001 V2 (CD-ROM)*, NASA-JPL, distributed by PDS, 1991.

Ivanov, B. A., A. T. Basilevsky, V. P. Kryuchkov, and I. M. Chernaya, Impact craters of Venus: Analysis of Venera 15 and 16 data, *J. Geophys. Res.*, *91*, B4, D413-D430, 1986.

Ivanov, B. A., I. V. Nemchinov, V. A. Svetsov, A. A. Provalov, V. M. Khazins, and R. J . Phillips, Impact craters on Venus: Physical and mechanical models, *J. Geophys. Res.*, *97*, 16,167-16,181, 1992.

Iversen, J. D., R. Greeley, and J. B. Pollack, Windblown dust on Earth, Mars, and Venus, *J. Atmos. Sci*, **33**, 2,425-2,429, 1976.

Martin, J. J., *Atmospheric Reentry*, pp 264, Prentice-Hall, Englewood Cliffs NJ, 1966.

Melosh, H. J., *Impact Cratering - A Geologic Process*, pp 245, Oxford University Press, New York, 1989.

Melosh, H. J., Atmospheric breakup of terrestrial impactors, *Proc. Lunar Planet. Sci.*, *12A*, 29-35, Pergamon Press, New York, 1981.

Mizutani, H., Y. Takagi, and S. Kawakami, New scaling laws on impact fragmentation, *Icarus*, *87*, 307-326, 1990.

Nagasawa, K., Ablation of meteorites from the viewpoint of the meteor observation (in Japanese), *Earth*, *3(9)*, 588-595, 1981.

O'Keefe, J. D. and T. J. Ahrens, Large scale impact on the earth with an atmosphere, *Lunar Planet. Sci. Conf. XIX*, 887-888, LPI, Houston, 1988.

Passey Q. R. and H. J. Melosh, Effects of atmospheric breakup on crater field formation, *Icarus*, *42*, 211-233, 1980.

Phillips, R. J., R. E. Arvidson, J. M. Boyce, D. B. Campbell, J. E. Guest, G. G. Schaber, and L. A. Soderblom, Impact craters on Venus: Initial analysis from Magellan, *Science*, *252*, 288-297, 1991.

Roddy, D., D. Hatfield, P. Hassig, M. Rosenblatt, L. Soderblom, and E. De Jong, Computer simulations of comet- and asteroid-like bodies passing through the venusian atmosphere - Preliminary results on atmospheric and ground shock effects, Abstract, *Int. Colloquium on Venus*, Pasadena, CA, 94-96, 1992.

Rosenblatt, M., Numerical simulations of thermally precursed airblast characteristics for HOB explosions, *Proceedings 5th Mach Reflection Symposium*, edited by G. W. Ullrich, San Francisco, 1985.

Sakurai, A., Blast wave theory, in *Basic Developments in Fluid Dynamics*, edited by M. Holt, pp. 309-375, Academic Press, New York, 1968.

Schaber, G. G., R. G. Strom, H. J. Moore, L. A. Soderblom, R. L. Kirk, D. J. Chadwick, D. D. Dawson, L. R. Gaddis, J. M. Boyce, and J. Russell, Geology and Distribution of Impact Craters on Venus - What are they telling us?, *J. Geophys. Res.*, *97*, 13,257-13,301, 1992.

Schmidt, R. M., Meteor Crater: Energy of formation - implications of centrifuge scaling, *Proc. Lunar Planet. Sci. Conf. XI*, 2,099-2,128, Pergamon Press, New York, 1980.

Schmidt, R. M., Experiments to investigate atmospheric effects on crater size, *Proc. Lunar Planet. Sci. Conf. XXIII*, 1,221-1,222, LPI, Houston, 1992.

Schultz, P. H. and D. E. Gault, On surviving atmospheric entry, *Proc. Lunar Planet. Sci. Conf. XXIII*, 1,235-1,236, LPI, Houston, 1992.

Seiff, A., Thermal structure of the atmosphere of Venus, in *Venus*, edited by D. M. Hunten, L. Colin, T. M. Donahue, and V. I. Moroz, pp. 215-279, University of Arizona Press, Tucson, 1983.

Takata, T., J. D. O'Keefe, T. J. Ahrens, G. S. Orton, Comet Shoemaker-Levy 9: Impact on Jupiter and plume evolution, *Icarus*, **109**, 3-19, 1994.

Tani, I., *Fluid Dynamics* (Japanese), pp 268, Iwanami, Tokyo, 1967.

Ulaby, F. T., Radar signatures of terrain : Useful monitors of renewable resources, *Proc. IEEE*, *70(12)*, 1410-1428, 1982.

Vervack, R. J. and H. J. Melosh, Wind interaction with falling ejecta: origin of the parabolic features on Venus, *Geophys. Res. Lett.*, *19*, 525-528, 1992.

Vincenti, W. G. and C. H. Kruger, *Introduction to Physical Gas Dynamics*, P. 182, John Wiley, New York, 1965.

White, F. M., *Viscous Fluid Flow*, pp 725, McGraw-Hill, New York, 1974.

Zahnle, K. J., Airburst origin of dark shadows on Venus, *J. Geophys. Res.*, *97*, 10,243-10,255, 1992.

Zel'dovich, Y. B. and Y. P. Raizer, *Physics of Shock Waves and High-Temperature Hydrodynamic Phenomena*, pp 93-101, Academic Press, New York, 1965.